Departamento de Física Teórica
Universidad Autónoma de Madrid

Flexibility of neuronal codes: Adaptation to stimulus statistics in a mechanosensorial neuron firing in bursts

Presentada por: Sara Arganda Carreras
Dirigida por: Dr. D. Gonzalo García de Polavieja Embid
Tutorizada por: Dr. D. Carlos Avendaño Trueba

Para la obtención del grado de
Doctor
por la Universidad Autónoma de Madrid
dentro del Programa de Doctorado en Neurociencias
del Dpto. de Anatomía, Histología y Neurociencia
Facultad de Medicina
Cantoblanco, Madrid, España
Abril 2009

To Carmen and Justo, my parents

To Ignacio and Ernesto, my brothers

Agradecimientos

Me imaginé muchas veces escribiendo los agradecimientos de mi tesis. Pensaba que sería mi gran momento para dar las gracias a todos los que me habéis ayudado, animado y también soportado durante estos años. Sin embargo, ahora me encuentro delante del ordenador con la certeza de que mis palabras van a ser insuficientes y torpes, que me voy a olvidar de gente que ha sido muy importante en este proceso y que cuando los vuelva a leer, me van a seguir quedando ganas de corregirlos. Pero no puedo dejar pasar esta oportunidad de daros públicamente las gracias, porque esta tesis ha sido para mí un trabajo colectivo en el que todos vosotros habéis participado de alguna manera.

El primero al que quiero dar las gracias es sin duda a mi director de tesis, Gonzalo García de Polavieja: Gracias por confiar en mí desde mi último año de carrera, gracias por estar siempre ahí para discutir de ciencia, para para resolver cualquier duda, gracias por el estupendo trabajo que hemos realizado juntos y muchísimas gracias por enseñarme otra manera de mirar a la biología. Quiero tambien agradecer muy especialmente a Raúl Guantes, no sólo su trabajo, sin el que esta tesis no habría sido posible, sino también todo su apoyo y la sonrisa con la que siempre me ha recibido cuando llegaba a su despacho con mi montaña de dudas sobre el programa o los metodos de análisis.

Quiero dar las gracias por su atención y disponibilidad a Carlos Avendaño Trueba, mi tutor en el Dpto. de Anatomía, Histología y Neurociencia de la UAM. Y del mismo departamento, no puedo olvidarme de Basilio Cáceres, Miguel Garzón y Esther del Cid, sin cuya ayuda, los trámites administrativos me habrían devorado. Gracias también a Alec Urazaev y Chris Sahley, en cuyo laboratorio (Purdue University, Indiana) pasé tres estupendos meses de estancia. Gracias también a Mikko Juusola por el mes y medio que pasé en su laboratorio, por el programa de análisis y por el estimulador mecánico. A Pablo Varona y al Grupo de Neurocomputación Biológica, con quien colaboramos en los primeros años.

Muchísimas gracias a mi familia por su apoyo y confianza incondicionales, especialmente a mis padres, Carmen y Justo (responsables de todo lo bueno que hay en mí) y a mis hermanos, Ernesto e Ignacio (no sé qué haría sin vosotros). También muchas gracias a Tito y Ana (siempre dispuestos a escucharme), a mi pequeño Jorge (que me supera en

estatura y en muchas otras cosas), a mis abuelos, Paquito y Lala (¿que habría sido de mi tesis sin mi taxista particular?), a Esther (para mí, mi hermana mayor), a Andrea (gracias por todos tus ánimos de estos meses)...

Gracias a todos los que habéis sido y a los que sois mis compañeros de laboratorio, especialmente a Marta (me alegro de compartir tanto contigo), Amanda (compañera de las horas tardías), Bea (cómo te echo de menos) y Alfonso (cualquier cosa que diga va a quedar corta, asi que ¡ñuiski!) que sois tan buenos compañeros como amigos. A todos con los que he compartido todos estos años en el Instituto Nicolás Cabrera: Pablo (echaré de menos que vengas a "molestar"), Paloma (gracias por la luna y por tantas cosas), Silvia, Ricardo, Marisela (gracias por compartir experiencias y dudas), Javi, Julián, Ileana, Judith, Santi, Lucía, Srikanth, Gabriel, Benjamin, Thomas... y muy especialmente a Marta Irimia (quedó bastante vacío cuando te fuiste).

Gracias a los amigos que siempre estáis cerca: Teresa (te extraño por Madrid), Alba, Rubén (mi insustituible anti-psicólogo), Sergi (mi tercer hermano), David, Sergio Montero (gracias por tus empujones), David Carratala, Juanjo, Ana Isabel (¡ánimo con la tuya!), Inés, Julia, Mario, Amaya, Ángel, Gilda, Ana Sáhara, mis niñas de la Fragua... A los que se convirtieron en mis amigos en la Facultad de ciencias: Alberto (también se te echa bastante de menos), Jose Delgado, Nico, Jose Oñorbe, Tomás, LuisFer, Ana Fernández, Belén, Arturo, Juanchi (de visita)... A los compañeros de la carrera que siguen ahí: Juanma (siempre dándome ánimos), Graciela, Jana y Blas, Alex (¡cuántas visitas os debo!)... A los compis de Precarios. A mis compis de piso, que han sufrido las consecuencias de mi escritura: Marta (¡de nuevo!) y Miki. A todos los que también habéis estado atentos a mis progresos y a mis desesperaciones de los últimos meses: Joel (nos debemos unas cañas), Amor, Miguel Rey, IsaIpa, David Temes, Fátima, Coco, Cristian (¡gracias por los artículos!)...

Finalmente, gracias a la Universidad Autónoma de Madrid por la Ayuda para estudiantes de Tercer Ciclo de mi primer año de doctorado y a la Comunidad de Madrid por la financiación de los 4 años de beca y contrato de formación de personal investigador y de mi estancia en EE.UU.

Contents

Nomenclature

ΔV	Hyperpolarization.
μ	Mean of a probability distribution.
σ	Standard deviation of a probability distribution
σ_{posit}	Standard deviation of a position probability distribution.
σ_{vel}	Standard deviation of a velocity probability distribution.
g_{Ca}	High-threshold non-inactivating Calcium conductance.
$g_{\text{K,Ca}}$	Calcium-activated Potassium conductance.
g_{K}	Delayed rectifier Potassium conductance.
g_{L}	Leakage conductance.
g_{Na}	Fast Sodium conductance.
I_{pump}	Sodium-activated pump current.
I_{Ca}	High-threshold Calcium current.
$I_{\text{K,Ca}}$	Calcium-activated potssium current.
I_{k}	Outward-persistent potassium current.
I_{L}	Leak current.
I_{Na}	Fast sodium current.
r_{av}	Average firing rate.
BTA	Burst-Triggered Average

BTP Burst Triggered Probability of stimulus.

IBI Inter-Burst Interval

ISI Inter Spike Interval

PCA Principal Component Analysis.

ROC Receiver Operating Characteristic.

SilTP Silence Triggered Probability of stimulus.

STA Spike-Triggered Average

STP Spike Triggered Probability of stimulus.

Abstract

In the present thesis we have described a sensory code in a spike-bursting mechanoreceptor in the leech *Hirudo medicinalis*. We have stimulated the neuron using naturalistic tactile stimuli with different statistical distributions while intracellularly recorded the cell bursting activity. Analyzing the input/output relationship, we found that this sensory code is based on the number of spikes per burst (burst size): Larger number of spikes per burst codes for larger velocity values of an object indenting the skin of the animal. We also found that the burst rate codes for velocity values of the stimulus.

Analyzing the flexibility of this sensory code, we further found that the burst sizes and rate code not for stimulus values *per se*, but for their ratio with the standard deviation of the stimulus distribution. There was a reduction in excitability correlating to an increase in hyperpolarization in response to higher stimulus variances. We examined whether the slow reduction in excitability induced by sodium-pump activity that has been seen in many neuronal types is also involved in this sensory coding. We have shown, by pharmacologically eliminating the action of sodium pumps, that the regulation of excitability by sodium pumps is necessary for the neuron to make different responses depending on the statistical context of the stimuli. In particular, sodium-pump activity allowed this sensory code to adapt to the stimulus velocity variance. Modeling further showed that sodium pumps can be a general mechanism of adaptation to statistics on the time scale of 1 min.

Resumen

En este trabajo de tesis hemos descrito el código sensorial de una neurona mecanoreceptora de la sanguijuela (*Hirudo medicinalis*) que dispara en ráfagas de potenciales de acción. Hemos registrado la actividad en ráfagas de la neurona a la vez que provocábamos su respuesta con estimulos táctiles con distinta distribución estadística. A través del análisis de la relación estímulo/respuesta, hemos encontrado que esta neurona tiene un código sensorial basado en el número de potenciales de acción por ráfaga: Ráfagas con mayor número de potenciales de acción codifican mayores valores de velocidad. Tambien hemos encontrado que la frecuencia entre ráfagas codifica la velocidad del estimulo táctil.

Analizando si se trataba de un código flexible, encontramos que el tamaño de ráfaga y la frecuencia entre ráfagas no estaban codificando el valor de la velocidad *per se*, sino el ratio del valor de la velocidad entre la varianza del estimulo. La neurona presenta además una reducción de la excitabilidad que corrrelaciona con un incremento en la hiperpolarización de la membrana en respuesta a varianzas del estimulo más grandes. Examinamos si la lenta reducción de la excitabilidad que se ha observado en otros tipos neuronales y que está inducida por la actividad de las bombas de sodio, está también implicada en este código sensorial. Hemos demostrado, a través del bloqueo farmacológico de las bombas de sodio, que la regulación de la excitabilidad por bombas de sodio es necesaria para que la neurona varíe su respuesta dependiendo del contexto estadístico del estimulo. En particular, la actividad de las bombas de sodio permite al código sensorial adaptarse a la varianza en las distribuciones de velocidades del estímulo. Simulaciones en un modelo de esta neurona muestran además que las bombas de sodio pueden ser un mecanismo general para la adaptación a la estadística en la escala de 1 minuto.

1 Introduction

1.1 The neuronal code problem

One of the most relevant characteristics of animals is that they have nervous systems. These structures are complex systems that evaluate external and internal conditions and generate different behaviors. The level of complexity varies along the evolutionary scale, but all nervous systems are processors of sensory and motor information. This processing entails filtering and interpreting sensory information and allows animals to react to changes in the environment, to make decisions and to respond with appropriate behaviors.

Nervous systems are built on several types of cells, categorized in two main groups: neurons and glial cells. Neurons are believed to be the most important active elements in the information network that drives different behaviors. They are known to receive, code and transmit the incoming information. Glial cells are usually described as supporting cells, however, recent studies show that astrocytes (macroglial cells of the central nervous system) are also implicated in information processing (Parpura et al., 1994; Volterra and Steinhäuser, 2004).

The study of how nervous systems work requires understanding how they process information, and for that we must first understand how neurons represent this information. This neuronal representation does not seem to be based on a fixed set of rules for the

whole nervous system. In contrast, this representation could depend on the neuron that is interpreting and processing the information, as well as on the information itself. A neuronal code is the way in which a neuron represents the incoming information.

In this thesis we decided to study sensory neurons, in order to have direct control over the stimulus eliciting the neuronal response. The role of sensory neurons is to translate the perceptible external world to the *neuronal language*. Sensory neurons are sensitive to physical variables such as temperature, pressure, concentration of a certain substance, intensity of light, wavelength, etc. The translation of these variables to the *neuronal language* constitutes a sensory code.

1.1.1 How to study a neuronal code

Wondering about neuronal codes leads to many different questions and approaches. Approaches to this problem go from a molecular to a systems point of view. We can, for example, be interested in describing the molecular mechanisms that underlie the neuronal representation of the information. Or we can wonder about how a population of neurons processes the information, and consequently forget about the role of single neurons.

This thesis, is focused on the representation of information by a single neuron. In this scenario, it is useful to consider neurons as black boxes, so that only input (stimulus) and output (neuronal response) are the essential signals that need to be analyzed to understand the neuronal code (Figure 1.1, *top*).

Borst and Theunissen (1999) pointed out three important questions when studying any neuronal code: *"What is being encoded?"* refers to the stimulus ensemble and stimulus features that the neuron processes, *"How is it being encoded?"* is centered in the type of code that the neuron uses, and *"With what precision?"* is related to the variance in the stimulus-response relationship, and therefore to the ability to discriminate between different stimulus values by the neuronal response (Figure 1.1, *bottom*). To answer these three interconnected questions, it is necessary to study the stimulus-response relationship. This relationship can be obtained through experiments in which we control and monitor the stimuli and record the neuronal responses at the right temporal scale.

To know *what is being encoded* by the neuron, we have to find a correlation between some parameters of the stimulus and the neuronal response. Choosing the correct stimulus ensemble and the relevant stimulus parameters is not trivial. Indeed, it is important to take into account that the way in which these parameters vary can lead to different interpretation of the results. In some cases, simple stimuli can suggest the relevant parameters, but some authors, like Sejnowski (1999), consider that realistic stimuli are

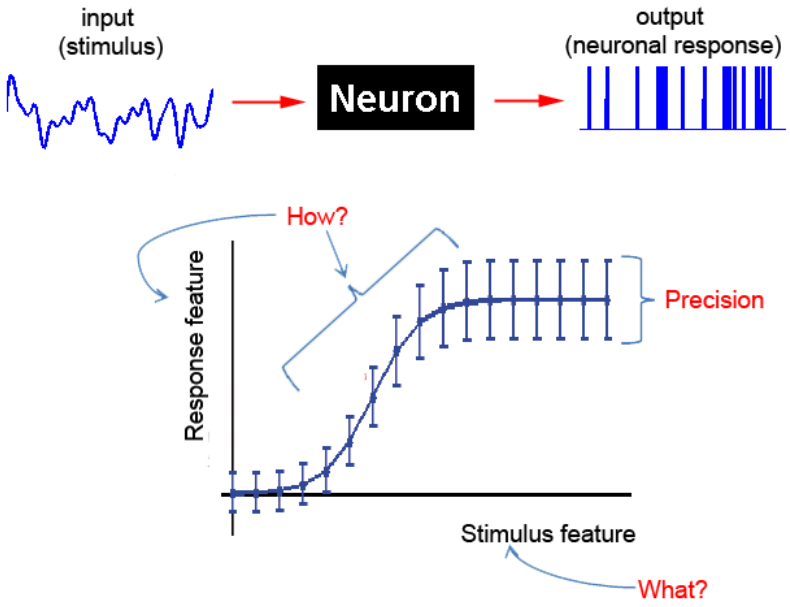

Figure 1.1: **Studing neuronal codes**. Schematic representation of the process to understand a neuronal code. *Top*: Neurons receive input (stimulus) and produce outputs (neuronal response). *Bottom*: The relation between some features of the stimulus and the response gives a clue to understanding the neuronal code. *What?* refers to the stimulus features that are being encoded in a certain way by some response features (*How?*), and the variance of the response give an approximation of the *precision* of the code.

needed to describe the efficiency of a neuronal code.

The description of the type of code, or *how is the information being encoded*, encloses two questions: *"Which parameters of the response are carrying the information?"* and *"what is the relationship between the input and the output?"*. To answer the first question, we need to find the relevant parameters in the neuronal response that carry the information about the stimulus. For the second question, we have to extract, from the stimulus-response relationship, the way in which different values of the response parameters are coding for different values of the stimulus.

The *precision* of the neuronal code refers to the ability of the response to accurately discriminate between different values of the stimulus. This precision can be quantified using methods of signal discrimination analysis that have been largely applied in this field (Rieke et al., 1997).

Another important aspect of the study of a neuronal code is its reliability. The reliability of a neuronal code refers to its reproducibility when the neuron is exposed to

repeated presentation of the same stimulus and is closely related to *what*, *how* and *with what precision* a neuron encodes information. Information theory (Shannon, 1948) is a rigorous mathematical framework that can be used to quantify this reliability. Information theory methods can determine how much information about the stimulus parameters is contained in neuronal responses and also evaluate the nature and precision of the neuronal codes (Rieke et al., 1997).

1.1.2 Types of neuronal codes

Neurons are cells with an excitable membrane, and that means that their membrane potential changes in response to appropriate stimuli. There are two types of changes in membrane potential: action potentials or spikes and graded potential changes. Spikes are fast changes of the membrane potential and are typically considered all-or-non stereotyped waveforms. Graded potential changes are non-stereotyped events and their shape strongly depends on the stimulus.

Spikes or graded potential changes travel along the neuronal membrane and arrive to the presynaptic end, where they produce the release of neurotransmitters to the synaptic gap. Neurotransmitters are responsible for changes in membrane potential of the post-synaptic neuron and consequently for the transmission of the information from neuron to neuron. Thus, it seems clear that neuronal codes are built on spikes or on graded potential changes. Which features of these membrane potential changes can be relevant for coding the input that excite the neuron? In the case of gradual changes, the value and dynamics usually correlate to the stimulus. In the case of spikes, there are more options and controversy. Several types of coding have been proposed, such as the number of spikes per time unit (*rate coding*, Adrian and Zotterman, 1926; Adrian, 1928), the precise timing when they occur (*temporal coding*, Bialek et al., 1991) or the temporal clustering of spikes (*burst coding*, Lisman, 1997). However, it has been shown that spikes in some neurons are not as stereotyped as believed, and that their shapes carry some information that could be used by post-synaptic neurons (*shape coding*, Polavieja et al., 2005).

These different types of codes will be described separately, but most probably neurons do not have one pure type of code but a weighted combination of a few. Indeed, the debate between rate and temporal coding could be viewed as the discussion about two extremes of the same idea. Depending on the neuron, the precise spike times could have more or less importance in the code.

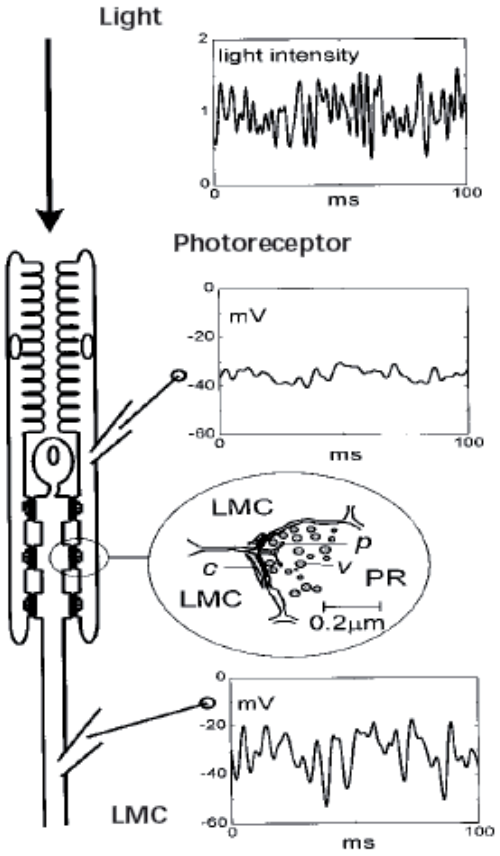

Figure 1.2: **Graded potential changes coding light intensity**. Photoreceptors and an LMC of the blowfly retina and lamina code light intensity in a single pixel of the compound eye. The stimulus is a randomly modulated light source. The signals are intracellular recordings of the graded changes of membrane potential induced by the stimulus. Six photoreceptors carrying the same signal converge on a single LMC and drive it via multiple parallel synapses. For clarity, only two of the six photoreceptors are depicted. The oval inset shows a photoreceptor-to-LMC synapse. The presynaptic site on the photoreceptor axon terminal (PR), contains synaptic vesicles (v), grouped around a prominent presynaptic ribbon (p). This release site faces four postsynaptic elements, containing cisternae (c). (Figure from Laughlin et al., 1998)

1.1.2.1 Coding based on graded potential changes

A non-spiking neuron transmits the incoming information by graded changes in its membrane potential. In Figure 1.2 (from Laughlin et al., 1998) we can see two examples of non-spiking neurons involved in phototransduction: Photoreceptors and Long Monopolar Cells (LMC) in blowfly. Photoreceptors transmit information about light intensity,

while LMC (postsynaptic to photoreceptors) make a more complex processing of the light signal. Both cells use graded potential changes to encode information.

Graded potential changes can carry more information than spikes. This is due to the fact that graded potential changes are continuous signals, while spikes are not. However, while neurons have mechanisms to accurately regenerate spikes through the axon, they do not have these kinds of mechanisms for graded potential changes. Therefore, part of the information carried by graded potential changes can be lost if it has to travel long distances.

1.1.2.2 Shape coding

Spike shapes vary from neuron to neuron, but they are typically considered stereotyped events of each cell. However, spikes in the same neuron can present different shapes. These differences are usually neglected because they are believed to have poor or no effect in the whole network. Nevertheless, there is experimental evidence of the implication of spike shapes on the neuronal code (Polavieja et al., 2005; Alle and Geiger, 2006; Shu et al., 2006).

Polavieja et al. (2005) recorded the activity of pyramidal neurons of rat cortex stimulated by dynamic clamp (a technique of conductance injection that mimics natural synaptic input) to examine the effect of stimulus history on spike shape. They found that different shapes of spikes (taller or wider, Figures 1.3A-B) had different conductance histories, as we can see in Figure 1.3C. They proposed a spike-shape code for pyramidal cells, in which broader somatic spikes are reliably produced in response to higher conductance input, allowing for four times more information transfer than spike times alone. This study shows experimentally that the shapes of spikes carry information about the stimulus.

Alle and Geiger (2006) showed that axons can transmit *analog signals* in addition to spikes at the mossy fiber–CA3 synapse. By *analog signals* they understand excitatory presynaptic potentials, which result from subthreshold dendritic synaptic inputs. These excitatory presynaptic signals were found to propagate to the presynaptic buttons, where they modulate the neurotransmitter release produced by spikes. In this context, spikes (*digital signals*) and subthreshold potentials (*analog signals*) are believed to be independent, however, for a external observer, the subthreshold potentials are indeed changing the shape of spikes.

From this point of view, Shu et al. (2006) found that modest changes in the somatic membrane potential of a presynaptic neuron modulate the amplitude and duration of axonal spikes and also the average amplitude of the EPSPs (excitatory potsynaptic po-

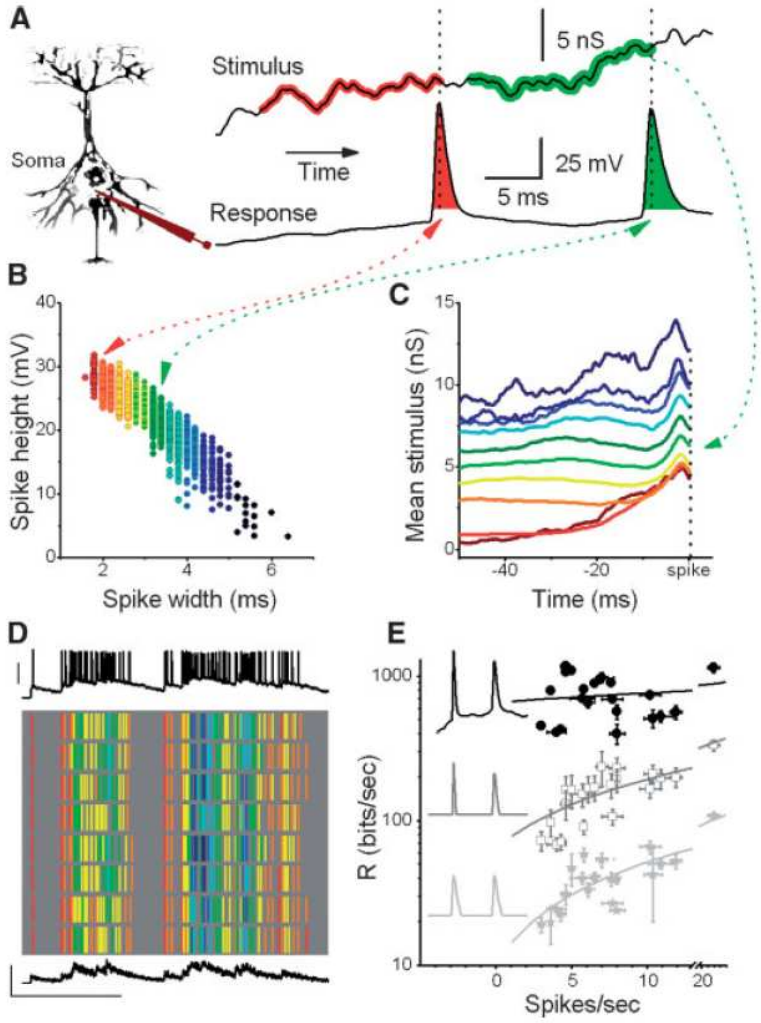

Figure 1.3: **Spike shapes carry information about the stimulus in cortical neurons**. **A**. Rapid changes in synaptic conductances at low input levels evoke tall and slim spikes (red); high input level evoke short and fat spikes (green). **B**. Sorting the spikes by their waveforms reveals a characteristic width–height distribution. **C**. The stimulus histories leading to similar action potentials are closely related, suggesting that each action potential waveform encodes in a compressed format tens of milliseconds of stimulus history prior to firing. **D**. Different trials with the same naturalistic conductance pattern show that the same spike-shapes are reliably produced by the same stimulus history, demonstrating that there is very little noise in the encoding. **E**. Comparison of the rate of information transfer, R, for the total somatic voltage responses (black symbols), the spike-shapes alone (gray open symbols) and the data where all the action potentials are replaced by a mean spike-shape. Spike-shape alone carry four times more information than pulsatile spikes (Figure from Juusola et al. (2007))

tentials) produced by these spikes in the postsynaptic neuron. These results further prove that the shapes of spikes can in fact have an effect on the postsynaptic neuron, and consequently on the information transmission.

Taking into account that spike shapes can both carry information about the stimulus and have an effect on the postsynaptic neuron, it seems reasonable to conclude that neurons may also use a code based on spike shapes.

1.1.2.3 Rate coding

The firing rate of a neuron is the number of spikes per second that the neuron is firing. When the specific spike sequence does not contain more information about the stimulus than the firing rate, we say that the neuron is using a rate code. Rate coding was first described by Adrian and Zotterman (1926). They showed that the firing rate of stretch receptor neurons in the frog muscles is related to the force applied to the muscle. In Figure 1.4 we can see a clear example of rate coding in a chemoreceptor of the honey bee. The chemoreceptor was stimulated by increasing concentrations of CO_2 and its response was an increasing firing rate (Lacher, 1964).

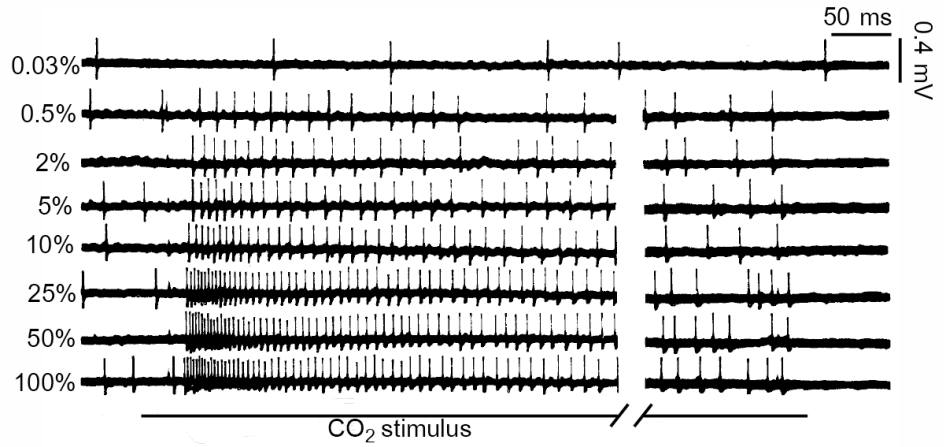

Figure 1.4: **Increasing firing rate in the response of a chemoreceptor in honey bee to increasing [CO_2]**. The chemoreceptor of the honey bee was stimulated by different [CO_2] (0.03, 0.5, 2, 5 , 10, 25, 50, 100% of CO_2 in air). The firing rate of the neuron increased with [CO_2]. (Figure from Lacher, 1964)

The term *firing rate* refers to spikes per time unit, but there are different averaging procedures to calculate it. According to these procedures we can get different quantities: spike-count rate, time-dependent firing rate and average firing rate. The spike-count rate is calculated by dividing the number of spikes in a trial by the duration of the trial.

The disadvantage of this rate is that it loses all temporal resolution about variation in the neuronal response during the trial. The time-dependent firing rate is defined by the number of spikes in short time intervals, which improves the temporal resolution. However, for very short time interval (and high temporal resolution), it needs to be averaged from several trials to avoid only two possible firing-rates values (0 and 1). The average firing rate is the average of the spike-count rate over several trials and also the time average of the time-dependent rate.

Variability in spike times can be considered noise in the neuronal response. The advantage of coding information by firing rates is that the neuronal response is averaged in time. This average in time makes the rate code robust with respect to the noise. However, rate coding has two disadvantages. First, averaging needs time, and consequently, the information encoding is slow. And second, by considering the variability in the spike sequence as noise, all the information that could be contained in the precise timing of the spikes is neglected (Stein et al., 2005). Thus, the assumption of rate coding might be ignoring parts of the code.

1.1.2.4 Temporal coding

A temporal code implies that precise spike timing or high-frequency firing-rate fluctuations carry information. It is important to note that there is no absolute time reference in the nervous system, so that the information is carried either in terms of the relative timing of spikes in a population of neurons or with respect to an ongoing brain oscillation (Stein et al., 2005). This type of code was defended by Bialek et al. (1991) to understand neuronal coding from the point of view of the organism. They argued that calculating firing rates needs an average over trials that it is not realistic in nature. They defended that to claim that a neuron uses firing rates to code information, one also needs to explain how the organism could estimate these firing rates from real-time observation of the spike trains. Precision and reproducibility of spike timing are the basis to differentiate between rate and temporal codes (Figure 1.5).

To test the type of code, the stimulus has to be repeated in order to evaluate the importance of spike times in the code. The relevant parameter for a rate code is the firing rate, but it can be achieved by different spike sequences. However, a temporal code is based on precise spike times. Figure 1.6 shows a real example of temporal coding in the central auditory area of songbirds. The spike timing turns out to be highly reproducible and to carry a 20% more information than modulations of spike rate (Wright et al., 2002). However, spike timing has a dual nature, as it can reflect the neuronal code but is also affected by the temporal properties of the stimulus. In any neuronal code, stimuli

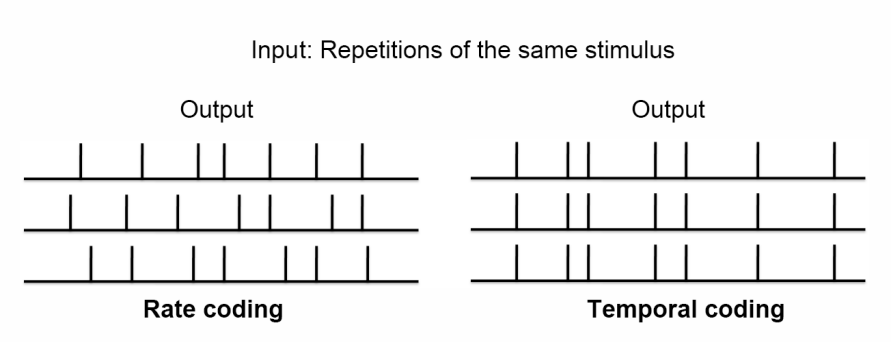

Figure 1.5: **Rate coding versus temporal coding**. Repetition of the same stimulus produces neuronal responses in which precision and reproducibility of the spike trains vary depending on the type of code. Rate coding (*left*) requires a neuronal response in which repetition of the same stimulus are represented by the same firing rate, but it allows variability in the spike times. Temporal coding (*right*) involves a neuronal response in which repetitions of the same stimulus produce the same specific spike train.

that change rapidly tend to generate precisely timed spikes and fast changes in firing rates. To resolve this, Theunissen and Miller (1995) proposed that, for a temporal code, information carried by spike times should be related to properties of the stimulus, but in a shorter time scale than the fastest time scale that characterize variations in stimulus.

1.1.2.5 Burst coding

Bursts are discrete groups of spikes that are followed by a period of quiescence before the next group of spikes occurs. In Figure 1.7 we can see an example of burst firing from a neuron of mouse first somatosensory cortex. Neurons firing in bursts are found in many different animals and in many different parts of the nervous system (Connors and Gutnick, 1990). In mammals, we can find bursty neurons in many parts of their nervous system, for instance in the neocortex (Connors and Gutnick, 1990; Gray and McCormick, 1996; Markram et al., 2004), hippocampus (Kandel and Spencer, 1961; Su et al., 2001), thalamus (Jahnsen and Llinás, 1984; Schingnitz and Werner, 1980) or cerebellum (Womack and Khodakhah, 2002). There are well known neurons firing in bursts in other animals like lobster (Combes et al., 1997), *Aplysia* (Barker and Gainer, 1975; Carnevale and Wachtel, 1980), *Clione* (Arshavsky et al., 1989) or the weakly electric fish (Metzner et al., 1998). Indeed, almost every neuron can be forced to fire in bursts under pharmacological manipulation or when the relevant stimulus oscillates around the firing threshold.

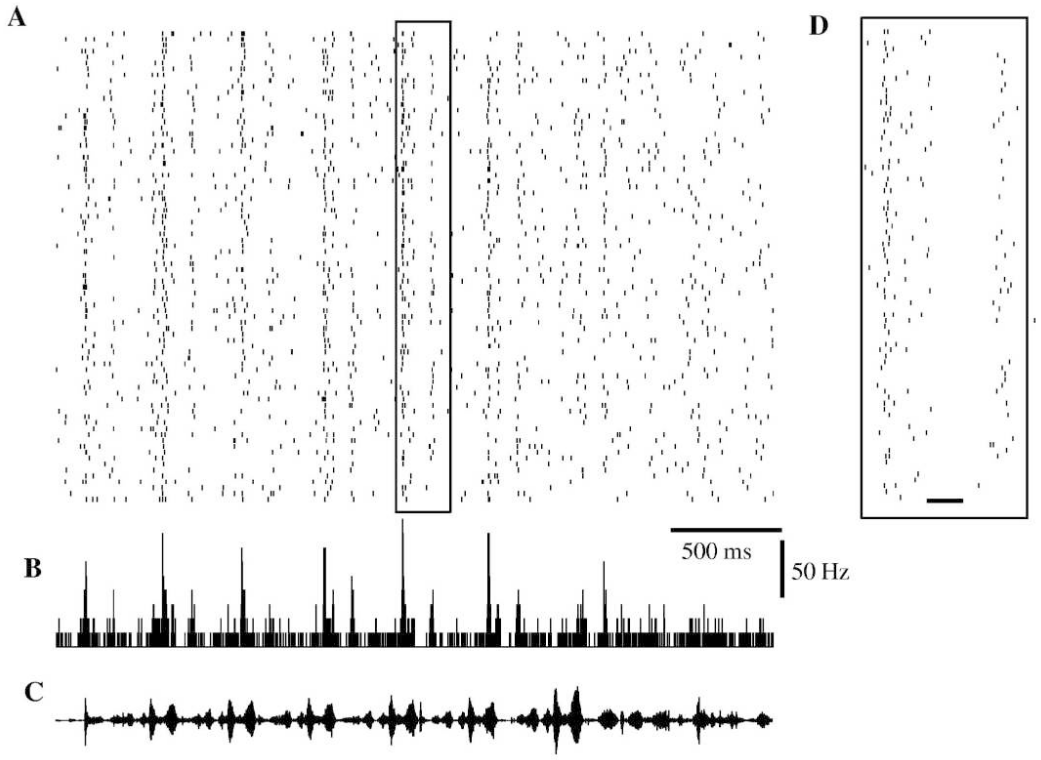

Figure 1.6: **Temporal coding in a central auditory area of songbirds**. **A**. Spike raster plot of the response of a single neuron of the central auditory area of songbirds to a natural sound (80 repetitions). **B**. Peri-stimulus time histogram (histogram of the times at which neurons fire) with 1 ms bins **C**. Sound pressure waveform for the natural sound ensemble.**D**. Blowup of segment shown in the box in A. The scale bar is 50 ms. (Figure from Wright et al. (2002))

Figure 1.7: **Intrinsic bursting activity in mouse cortex**. Repetitive intrinsic bursting in response to prolonged stimulus in a neuron near to the border of layers V and Vl in mouse first somatosensory cortex. Figure from Connors and Gutnick (1990).

The generation of bursts *in vivo* can be controlled by inputs onto the dendrites and by network characteristics or by intrinsic cellular mechanisms (Krahe and Gabbiani, 2004). When the origin is intrinsic, burst firing occurs as a result of the interaction of two types of biophysical processes: fast currents generating spikes and slower mechanisms controlling when bursts occur. According to the localization of these two processes, experimental (*in vitro*) and modeling studies point at two burst generating mechanisms: adendritic and dendritic.

Adendritic mechanisms imply only somatic currents. These mechanisms take place in neurons that are electrotonically very compact, in which there is not any relevant interaction between dendrites and soma. In Figure 1.8a we can see a model of a cerebellar granule cell based on seven somatic conductances (Krahe and Gabbiani, 2004). The slow process controlling burst activity is thought to be an alternating activation of a persistent Na^+current and a slow repolarizing K^+current. The fast process generating spikes within bursts relies on fast Na^+/K^+ channels and a fast spike afterhyperpolarization (AHP) produced by a Ca^{2+}-dependent K^+ current, which accelerates the removal of inactivation of fast Na^+channels. In addition, a resurgent Na^+current, I_{NaR}, is responsible for a delayed depolarizing afterpotential (DAP), which helps to trigger the next spike of the burst.

Dendritic mechanisms take into account the interaction between somatic and dendritic currents and are usually described as "*ping-pong*" mechanisms. Some models show that changes in size and electrotonic structure of dendritic trees can change the firing mode from tonic to bursty (Mainen and Sejnowski, 1996), indicating the possible importance of dendritic trees in the generation of bursts. Spike backpropagation from the soma to the

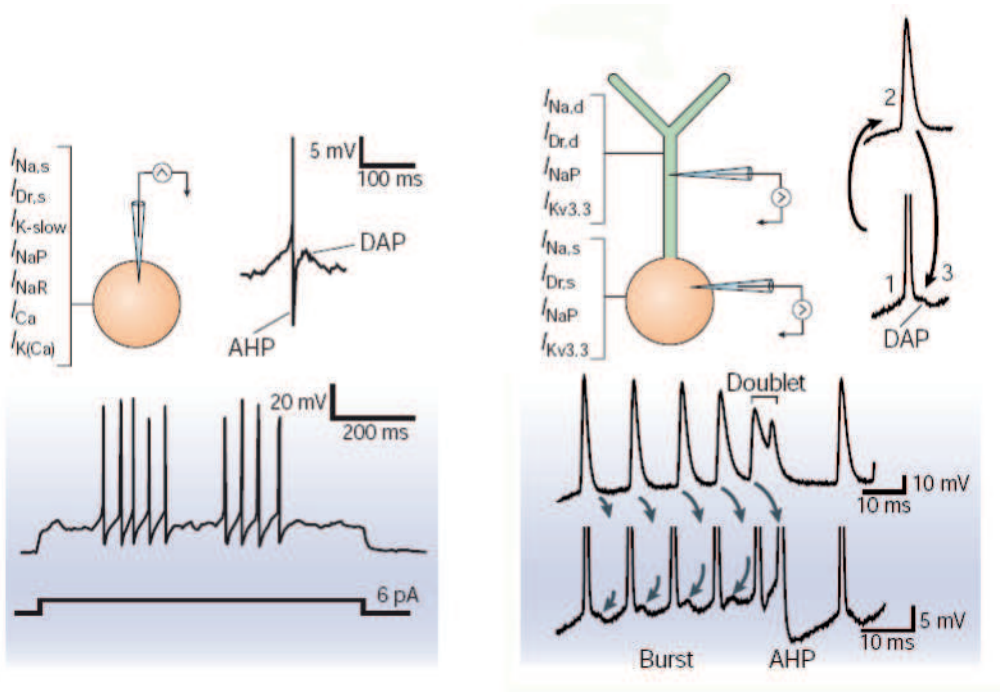

(a) Adendritic mechanism.

(b) Dendritic mechanism.

Figure 1.8: **Bursting mechanisms**. **a**. Adendritic mechanism: Model of a cerebellar granule cell based on seven somatic conductances. *Top left*: schematic electrotonic structure and conductance list. *Top right*: High-frequency burst spikes rely on fast Na^+ ($I_{Na,s}$), delayed rectifier ($I_{Dr,s}$) and fast afterhyperpolarization (AHP, $I_{K(Ca)}$) currents. The Ca^{2+}-dependent K^+ current, $I_{K(Ca)}$, is activated by a Ca^{2+} conductance, I_{Ca}. A resurgent Na^+ current, I_{NaR}, mediates the depolarizing afterpotential (DAP). *Bottom*: two bursts in response to a current pulse. Bursting is favored by a persistent Na^+ current (I_{NaP}) and terminated by a slow K^+ current ($I_{K\text{-}slow}$). **b**. Dendritic mechanism: Model of a electrosensory lateral-line lobe (ELL) pyramidal cell of the weakly electric fish. *Top left*: schematic electrotonic structure with soma and dendrites and conductance list of each part. *Top right*: Narrow somatic spikes (1) propagate back into the apical dendrite where they broaden due to slower dendritic conductances, $I_{Na,d}$ and $I_{Dr,d}$ (2). Current sourcing back into the soma causes a DAP (3). *Bottom*: Somatic and dendritic spike bursts recorded separately in two cells (somatic spikes truncated). The slowdown in dendritic spike repolarization is due to slow inactivation of a dendritic K^+ conductance ($I_{Kv3.3}$) and results in a potentiation of the somatic DAP (arrows). When the DAP reaches threshold for a high-frequency spike doublet, the second spike fails to backpropagate. This allows the AHP to terminate the burst. Figure modified from Krahe and Gabbiani (2004).

dentritic tree is usually the basis of the dendrite-dependent burst generation (Krahe and Gabbiani (2004)). Figure 1.8b shows a model of electrosensory lateral-line lobe (ELL) pyramidal cells of the weakly electric fish (Krahe and Gabbiani, 2004). Somatic spikes propagate back to the apical dendrite and produce the activation of slower dendritic conductances, that cause a DAP in the soma. When DAP reaches the firing threshold, the neuron fires a burst of two high-frequency spikes (or doublet).

Burst firing has important implications in the information transfer between neurons. For instance, bursts are known to facilitate synaptic transmission (Lisman, 1997), can improve the signal-to-noise ratio of responses (Cattaneo et al., 1981; Sherman, 2001) or detect certain signals better than isolated spikes (Gabbiani et al., 1996). Experimental and theoretical evidence shows that burst firing represents another type of neuronal code (Gabbiani et al., 1996; Krahe and Gabbiani, 2004). In the study of a neuronal code based on bursts it is necessary to describe which burst parameters are relevant for information transmission. Several proposals have been made, including spike frequency (Izhikevich et al., 2003), burst duration (DeBusk et al., 1997; Lisman, 1997), latency of the first spike (Middlebrooks et al., 1994), interspike interval within a burst (Doiron et al., 2007; Oswald et al., 2007) and number of spikes per burst (Martinez-Conde et al., 2002; Kepecs et al., 2002; Arganda et al., 2007; Eyherabide et al., 2008).

The burst-size code proposed by Kepecs et al. (2002) can serve as example to further understand how bursts can be the basis of a neuronal code. In a previous study, Gabbiani and Metzner (1999) analyzed the neuronal response of first and second-order sensory neurons in the the weakly electric fish. When the animal was stimulated by weak electric fields with random amplitude modulations, spikes in the P-receptor elements (first-order sensory neurons) accurately encoded these random amplitude modulations (probably by a rate code). The ELL pyramidal cells (second-order sensory neurons, in the electrosensory lateral line lobe) fired short bursts of spikes that were found to extract up and down-strokes (slopes) in the random amplitude modulations.

Kepecs et al. (2002) used a simple model of pyramidal neurons based on two compartments (soma and dendrite) to investigate the signaling properties of bursts (Figure 1.9a). They mimicked a random amplitude modulated stimulus and reproduced the experimental result of bursts detecting slopes (Figure 1.9b). The simulated neuronal response was composed of bursts of several sizes (number of spikes per burst) and also isolated spikes. They analyzed the value of stimulus slopes eliciting bursts of different sizes, and they obtained that larger bursts where coding for larger values of slopes. In Figure 1.9c we can see the probability distributions of slopes before bursts of two to five spikes. These distributions are clearly different, supporting the hypothesis of a burst-size code.

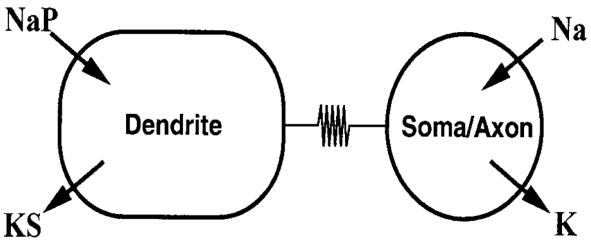

(a) Pyramidal neuron model.

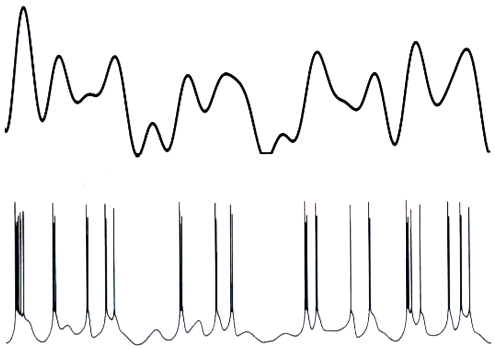

(b) Stimulated burst firing.

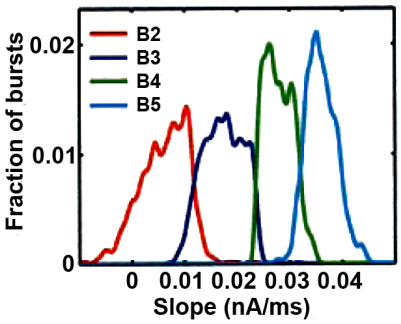

(c) Slope probability distributions given different burst sizes

Figure 1.9: **Burst-size coding**. **a**.Two-compartment model of pyramidal neurons. Somatic currents are Hodgkin-Huxley-type and generate fast spikes. Dendritic region contains a persistent sodium current and a slow potassium current responsible for bursting. **b**. *Top*: Random input applied to the dendrite. *Bottom*: membrane potential response (with bursts and isolated spikes) **c**. Distribution of stimulus slope before bursts of different sizes. B2 represents bursts of two spikes, B3 bursts of three spikes, and so on. Figures from Kepecs et al., 2002.

1.2 Code Flexibility: Adaptation in sensory systems

Adaptation of the neuronal response is a process by which the responsiveness of the neuron changes as a result of previous stimulation. Although there are some sensory neurons that do not adapt their response (as a population of SI cortical neurons responding to noxious stimuli, Kenshalo and Isensee, 1983), adaptation takes place at different levels in most sensory systems. Adaptation to static stimuli is a well-known phenomenon in nervous systems, but a constant value of stimuli is not likely in nature, as animals live in a continuously changing environment. Sensory systems have to deal with stimuli that

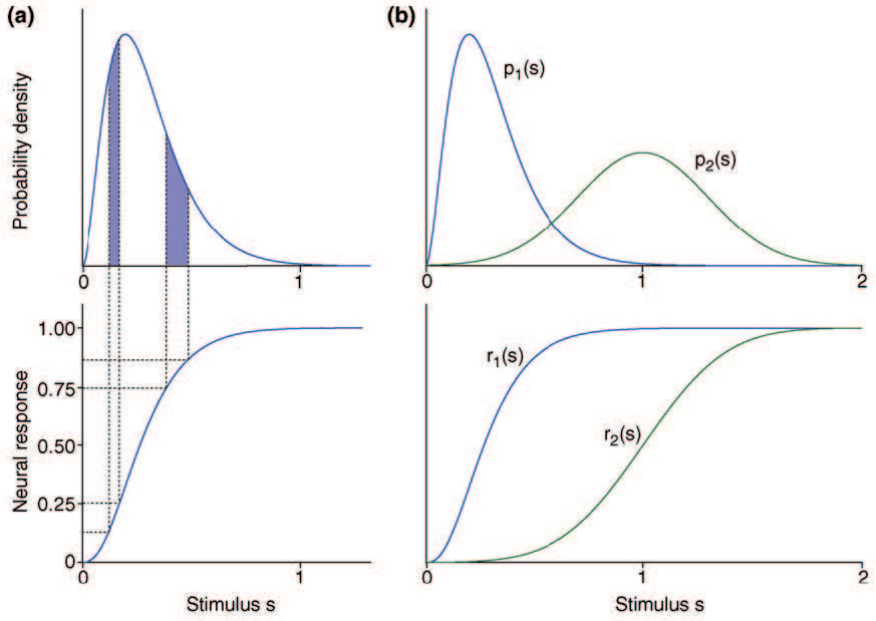

Figure 1.10: **Adaptation optimizes neuronal coding**. **a**. *Top*: An example of a stimulus distribution. *Bottom*: The most efficient stimulus/response relationship (the cumulative distribution). Equal probability in the stimulus distribution (shaded areas) are transformed to equal response ranges, making all responses equally likely. **b**. *Top*: Two different stimulus distributions, illustrating a change from the first one, $p_1(s)$, to a new one, $p_2(s)$. *Bottom*: The most efficient stimulus/response relationship also changes from $r_1(2)$ and $r_2(s)$. Figure from Wark et al., 2007, adapted from Laughlin, 1981.

fluctuate in time and that even change their scale of values. A sensory neuron has a limited range of outputs, which is insufficient to represent all the values of stimulus that are present in a natural context and that can span in many orders of magnitude.

To code more efficiently, a neuron needs to change its coding strategy when the statistical distribution of the stimulus varies. That means that the neuron should have a flexible neuronal code, capable of reassigning its range of outputs to the new range of inputs. Figure 1.10 shows how changes in the intput/output relationship makes the neuronal code more efficient. In Figure 1.10a *top* we can see the probability distribution of a stimulus and Figure 1.10a *bottom*, the input-output relationship corresponding to a maximum information transfer without noise that coincides with the cumulative probability of the stimulus (Laughlin, 1981). In Figure 1.10b we can see how the optimal response changes if the distribution of the stimulus varies.

Adaptation makes it possible for the neuron to have a more efficient code since it is a

process that changes the neuronal response depending on the previous stimulation. The neuron can fit its response to different stimulus statistics to maximize the information transfer (*infomax* principle, Linsker, 1988) or to enhance the response to some values of the stimulus while suppressing the response to others (*selective coding* principle, Sobel and Tank, 1994; Wimmer et al., 2008). From a more general point of view, in a context in which stimuli change probabilistically and the biological mechanisms have noise, adaptation allows the neuron to optimize the performance of a task, for example coding (Grzywacz and Balboa, 2002). However, it is important to notice that even if an adaptive neuronal code allows the neuron to be sensitive to details in a wider range of stimulus values, there can also exist one disadvantage. As the neuron reassigns its output to different inputs scales, the neuronal response could entail certain ambiguity.

To understand the functions and mechanisms that are responsible for the flexibility of neuronal systems under real-world conditions, it is necessary to study adaptation to stimuli in their statistical context. Neuronal adaptation to stimulus statistics enables the neurons to be sensitive to details of the stimulus at different ranges of values. Adaptation to the mean of the stimulus, the simplest parameter of a distribution, is a basic processing strategy in all sensory modalities that permits sensitivity to fluctuations around the mean (Barlow and Mollon, 1982; Walraven et al., 1990). A more sophisticated strategy is the adaptation to the variance of the stimulus distribution (Brenner et al., 2000; Deweese and Zador, 1998; Fairhall et al., 2001; Maravall et al., 2007; Meister and Berry, 1999; Shapley, 1989; Smirnakis et al., 1997) and perhaps to higher-order moments (Kvale and Schreiner, 2004). Stimulus variance also changes in time in natural conditions, and adapting to it allows the matching of output range to input range and a higher information transfer (Brenner et al., 2000; Fairhall et al., 2001; Sharpee et al., 2006).

1.2.1 Possible mechanisms underlying adaptation

Despite the importance of adaptation to stimulus statistics for the correct functioning of many systems, the underlying mechanisms remain largely unknown. Theoretical analysis and experimental evidence argue in favor of the existence of multiple mechanisms, (from synaptic or network, Abbott et al., 1997; Markram et al., 1998; Tsodyks and Markram, 1997, to intrinsic or single-neuron mechanisms, Diaz-Quesada and Maravall, 2008; Sanchez-Vives et al., 2000a; Rieke, 2001; Sanchez-Vives et al., 2000b; Stemmler and Koch, 1999), which probably span several time scales and work under different constraints (Fairhall and Bialek, 2002; Gilboa et al., 2005) and that could even have different effects on different types of code (Prescott and Sejnowski, 2008).

At the single-neuron level, different ionic currents have been described to be implicated in adaptation processes, especially the calcium-activated potassium currents. For instance, in the newt, the hyperpolarization produced by these currents has been shown to be necessary for odor adaptation (Kawai, 2002). More recently, sodium has been seen to play a relevant role in neuronal response adaptation (Bhattacharjee and Kaczmarek, 2005). Current injection experiments have identified slow sodium inactivation in bipolar cells (Kim and Rieke, 2003; Rieke, 2001) and sodium-dependent potassium conductances in cortex (Sanchez-Vives et al., 2000b) as potential mechanisms.

1.3 The leech as a tool to study sensory codes

The present thesis describes our study of a burst code in a mechanoreceptor cell of the leech *Hirudo medicinalis*. In this section we will describe the utility of using the leech to understand basic processes in nervous systems and also why we have studied the sensory code (and its properties) in this particular neuron.

1.3.1 Why the leech?

Nervous systems allow animals to perform very complex tasks such as coordinating muscle movements, discriminating among different values of one stimulus, making decisions, learning or creating memories. To study the underlying circuits and mechanisms of these abilities, one strategy consists of using the simplest possible system. The balance between structural simplicity and processing complexity points at the leech as a good candidate for studying basic neuronal mechanisms and circuits.

The nervous system of the leech is composed of a longitudinal cord connecting a head ganglion to a tail ganglion, passing through 21 segmental and practically identical ganglia (Figure 1.11). This ganglionic structure satisfies experimental requirements such as survival of synapses in isolated ganglia and healthy maintenance of neurons during long recordings. Furthermore, the segmented body of the leech makes it possible to perform experiments in a reduced preparation preserving structures, connections and functions of segments (Figure 1.12). It is then possible to apply controlled stimuli on the skin while recording intracellularly the response of a sensory neuron. Therefore, we can analyze the properties of the stimulus that the neuron is coding and the type of code that it is using.

Each segmental ganglion is composed of circa 400 neurons, big enough to be visible throw a dissection microscope (from 10 μm to 80 μm, Figure 1.13a), arranged in two layers and protected by glial cells. The ventral layer is mainly composed of sensory cells, while the dorsal side houses most of the motor-neurons. Interneurons are located

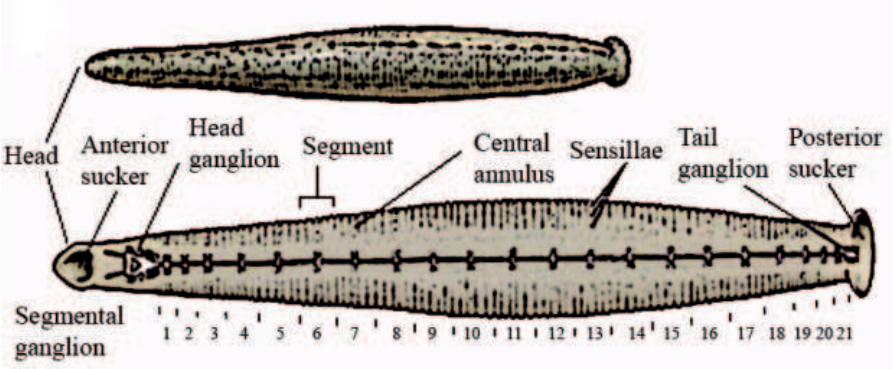

(a) Segmental body of the leech.

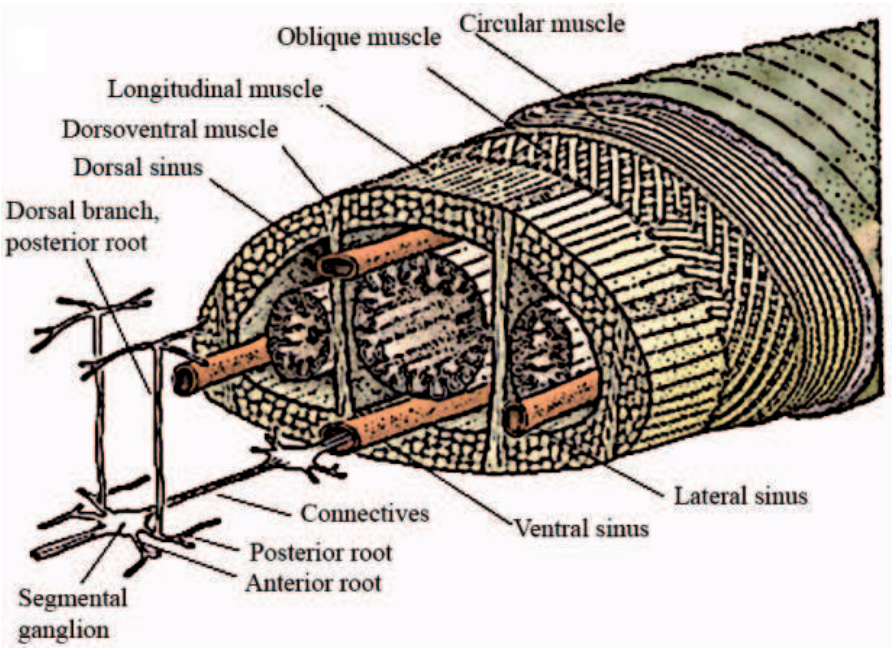

(b) Anatomical arrangement of leech organs.

Figure 1.11: **Leech Anatomy. a**. Scheme of the segmental anatomy of the leech focused on the nervous system structure. **b**. Position of the Nerval cord within the rest of the morphological structures, shown in a transverse view. (Modified from Nicholls and Van Essen (1974))

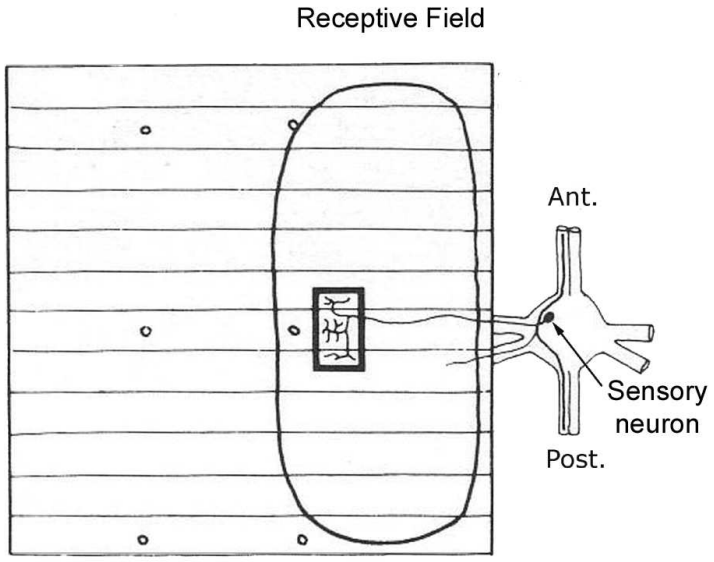

Figure 1.12: **Reduced preparation of the leech nervous system**. The neuroanatomy of the leech allows experimental preparations preserving the connections between sensory neurons to their receptive fields. (Modified from Blackshaw (1981))

throughout the ganglion. Most of the neurons are easily identified by simple visual inspection according to their shapes, sizes and positions inside the ganglion. Due to these anatomical features, it is relatively easy to perform electrophysiological recordings in the leech.

1.3.2 Why T cell?

Mechanosensory systems are good candidates for the study of sensory codes, as the stimulation can be easily controlled. Inside the leech segmental ganglia (Figure 1.13a), there are three types of mechanosensory neurons responding to: touch (T cells), pressure (P cells) and noxious mechanical stimuli (N cells). All of them can be easily recognized not only by size and position, but also by the temporal structure of their action potentials through intracellular recordings (Figure 1.13b). These three types of mechanoreceptors have been largely studied, including their firing pattern, connectivity, shapes, receptive fields, relevant stimuli, biophysical properties, etc. Among these three types of neurons, only T cells have a bursty firing when the skin is mechanically stimulated (Figure 1.13c, Van Essen (1973))

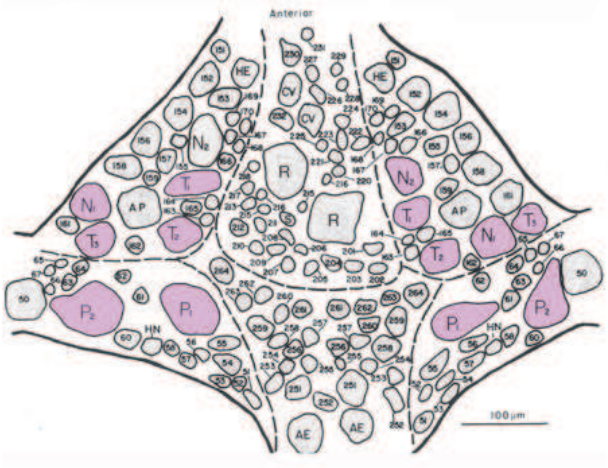

(a) Ventral side of leech ganglion.

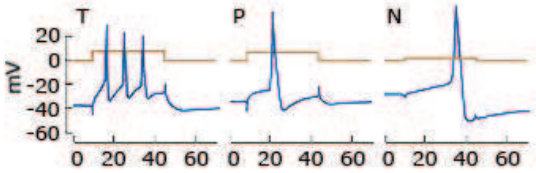

(b) Leech mechanoreceptors response to electrical stimulation.

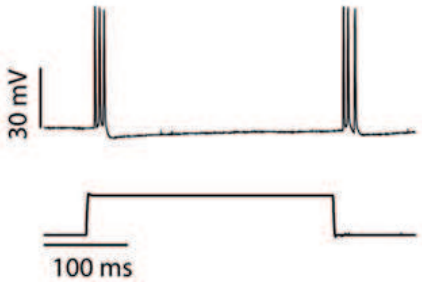

(c) T cell response to a mechanical step-like stimulus.

Figure 1.13: **Mechanosensory neurons in a segmental ganglion. a**. Ventral side of a leech ganglion. Colored neurons are T, P and N. (Modified from Muller et al., 1981) **b**. Typical firing pattern of a T, P and N neurons elicited by current injection. (Modified from Nicholls and Baylor, 1968) **c**.T cell response to a simple step-like mechanical stimulation (of height 0.4 mm and duration of 300 ms). .

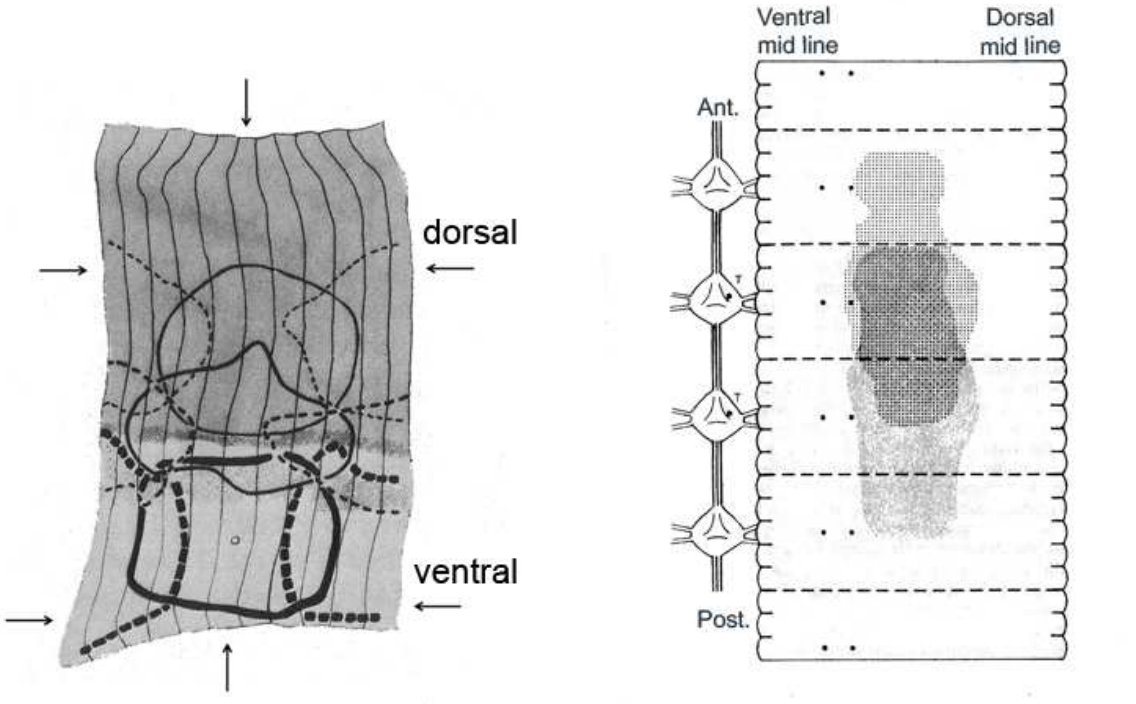

(a) T cell receptive fields.

(b) Overlapping receptive fields.

Figure 1.14: **Overlapping of receptive fields**. **a**. Receptive fields of T cells drawn on a piece of the skin. (→) marks dorsal and ventral mid lines of the skin; (↓) marks central annulus; solid lines represent boundaries in the receptive fields of the three T cells of the same lateral packet; dashed lines represent receptive fields of the T cells in adjacent ganglia. Figure from Nicholls and Baylor (1968). **b**. Receptive fields of two T cells in adjacent ganglia both innervating lateral skin. Each receptive field spans 12 to 13 annuli over three body segments, and extensively overlap. Figure from Yau (1976).

As we can see in Figure 1.13a, there are six T cells in each segmental ganglion, separated in two packets. T cells form a mechanosensorial network in which T cells on the same side of the ganglion are electrically connected, and T cells on different sides are connected via an interneuron (Baylor and Nicholls, 1969b). The neuronal processes of each packet only go through the ipsilateral nerve roots. Therefore, the receptive fields of each T cell is located ipsilaterally to the position of the soma and map to either the dorsal, lateral or ventral region. Each T cell also sends axons through connectives between ganglia, expanding its receptive fields to the adjacent segments. Each receptive field substantially overlaps with the adjacent ones (Figure 1.14).

The above description probably have important effects on the population code of the

T cells circuits, however we could wonder about the coding properties at a single neuron level. All T cells are mechanosensory neurons firing in bursts when the skin in their receptive fields is being indented by a moving object (Nicholls and Baylor, 1968). In Figure 1.13c we can see the dynamics of their response, which are as follows: When the object over the skin doesn't move, the cell remains silent; only when the object changes its position (going upwards or downwards) the T cell fires in bursts. This simple evidence and previous studies (Carlton and McVean, 1995) lead to think that T cells are coding changes in position or, in other words, velocities.

It is also known from previous studies, that repetitive mechanical stimulation of the skin leads to an after-hyperpolarization of the T cell membrane that can last from seconds to minutes and that have effects on the firing rate of the neuron (Baylor and Nicholls, 1969a; Catarsi and Brunelli, 1991; Catarsi et al., 1990; Jansen and Nicholls, 1973; Mar and Drapeau, 1996; Scuri et al., 2002, 2005; Van Essen, 1973). This hyperpolarization, up to 30 mV, is mainly produced (75% of its total amplitude) by the activity of the sodium pump, or Na^+/K^+ATPase, in response to the increase of Na^+ ions resulting from the spiking activity of the neuron (Baylor and Nicholls, 1969a; Jansen and Nicholls, 1973). The rest of the hyperpolarization, up to 5 mV, is due to a calcium-dependent potassium current, $I_{\mathrm{K,Ca}}$ (Jansen and Nicholls, 1973). The activity of the sodium pump controls the excitability of T cells in the scale of 1 min and therefore (Van Essen, 1973), may affect to sensory code of the T cell.

We thus consider that anatomy and neurobiology of the leech permit simple and powerful experiments to study the properties of a sensory code based on bursts.

2
Objectives

This thesis is focused on three aspects of the sensory code: a) the stimulus that is coded by the sensory neuron, b) the type of code that the neuron uses and c) the adaptive properties of the sensory code.

Our aim in this study was to demonstrate that:

- Some features of bursts can be used by neurons to code and discriminate between different values of stimulus features, in this case, of stimulus velocity.

  Previous studies show that among the three types of the leech mechanoreceptors, T cell responds to the lightest mechanical stimuli (Nicholls and Baylor, 1968) and that its repines get rapidly adapted when the skin is stimulated by a constant pressure (Pinato and Torre, 2000). This points at changes in position, or velocity, as the relevant stimulus features for T cell. We here wanted to probe this idea in a more quantitative way, using statistically richer stimuli functions.

  Moreover, T cell response has been described to be bursty when the skin is mechanically stimulated (Van Essen, 1973). Thus, we considered that bursts had to be playing and important role in the sensory coding of velocities.

- A neuronal response based on bursts can show adaptation to the statistics of the stimulus, in this case, to the standard deviation of velocities.

  Regardless of the type, sensory codes have to deal with a more o less variable environment. In most of the cases, evolution could have forced neuronal codes to be flexible in order to allow animals to act efficiently in a changing natural context. This flexibility could be supported by changes in the excitability of the neuronal membrane.

  It is known that the T cell response decrease after repetitive stimulation (Baylor and Nicholls, 1969a; Jansen and Nicholls, 1973; Mistick, 1978) and thus, we thought that this could be an effect of the adaptation to stimulus statistics.

- The ubiquitous sodium pump may be a molecular substrate for the adaptation of neuronal codes to the statistical context.

  The sodium-potassium ATPase, or sodium pump, is ubiquitous in neurons. During firing, Na^+ ions accumulate inside the axon, driving the sodium pump, which continues its activity even when the spike trains have ceased. The sodium pump exchanges three internal Na^+ ions for two external K^+ ions, and the resulting imbalance causes the membrane to recover from depolarization and can even hyperpolarize the membrane.

  The membrane hyperpolarization reduces membrane excitability, for example, in dopaminergic neurons (Shen and Johnson, 1998), spinal networks (Darbon et al., 2003), hippocampus (Gustafsson and Wigström, 1983; Vaillend et al., 2002), C-fibers in bullfrog sciatic nerve (Kobayashi et al., 1997), insect mechanoreceptors (French, 1989) and human skin receptors (Kiernan et al., 2004). And therefore can be underlying adaptation processes.

  In T cell, the sodium pumps are known to control the membrane excitability on the scale of 1 min (see section 1.3 for references). This control of excitability is achieved by inducing a 1 minute lasting hyperpolarization of up to 30 mV as a consequence of firing activity. Thus, sodium pumps are good candidates to be responsible of neuronal response adaptation.

3

Materials and Methods

3.1 Experimental preparation and recording set-up

Adult leeches, *Hirudo medicinalis*, weighting between 4 and 6 grams, were bought from Zaug GmbH Biebertal and kept in a pond water tank at 18^{o}C.

To anesthetize the animal before the dissection, the leech is firstly cooled in a extracellular solution at 4^{o}C for few minutes. The ordinary extracellular solution contained 115 mM NaCl, 4 mM KCl, 1.8 mM CaCl22H20, 1.5 mM MgCl22H20, 10 mM glucose, 4.6 mM Tris maleate, 5.4 mM Tris base. NaOH was added to achieve a pH of 7.4 at room temperature (24–26^{o}C).

Once the leech is anesthetized, the reduced nervous system preparation is made under a dissection microscope (Stemi SV11, Zeiss) using Fine Science Tools. Semi-intact leech preparations (three or four central ganglia with intact connections to their corresponding skin flaps) were used for the experiments (Figure 3.1a).

Intracellular recordings were performed typically from ganglia G8 or G9 and the skin of the outer segments was used to pin the skin flaps to a Petri dish filled with Sylgard (Dow Corning).

The experiments were carried out over an anti-vibration table (Newport) and under a fluorescence microscope (Axioskop 2 FS Plus, Zeiss) as shown in Figure 3.1b. Neu-

ronal activity was intracellularly recorded using chlorinated silver electrodes in 40-70 MΩ quartz micro-pipettes (pulled by a P-2000 puller and filled with 3 M Potassium Acetate). Signals were received by a preamplifier connected to an amplifier (Axo probe-1A, Axon Instruments) and, through signal filters, sent to the data acquisition cards of a PC computer with a custom made acquisition program, Biosyst (written in Matlab by M. Juusola and G. de Polavieja).

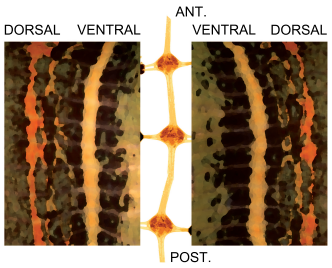

(a) Semi-intact preparation.

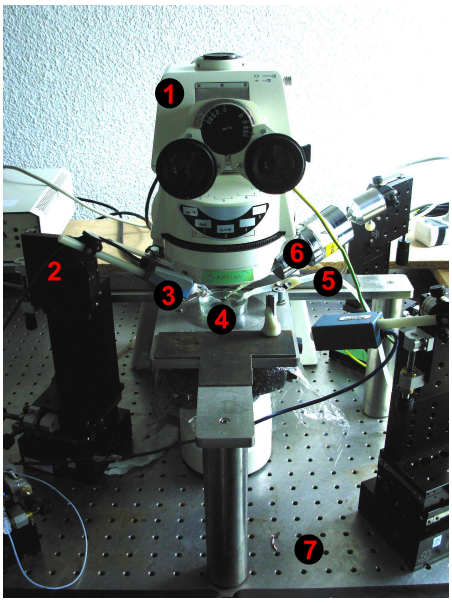

(b) Experimental set-up.

Figure 3.1: **Nervous system preparation and experimental set-up. a**. Drawing of the nervous system preparation with 3 ganglia (Photoshop modification from lab pictures). **b.** Experimental disposition: (1) Fluorescence microscope, (2) micro-manipulator, (3) pre-amplifier attached to a micro-electrode, (4) nervous system preparation, (5) flowing system, (6) mechanical stimulator and (7) anti-vibration table.

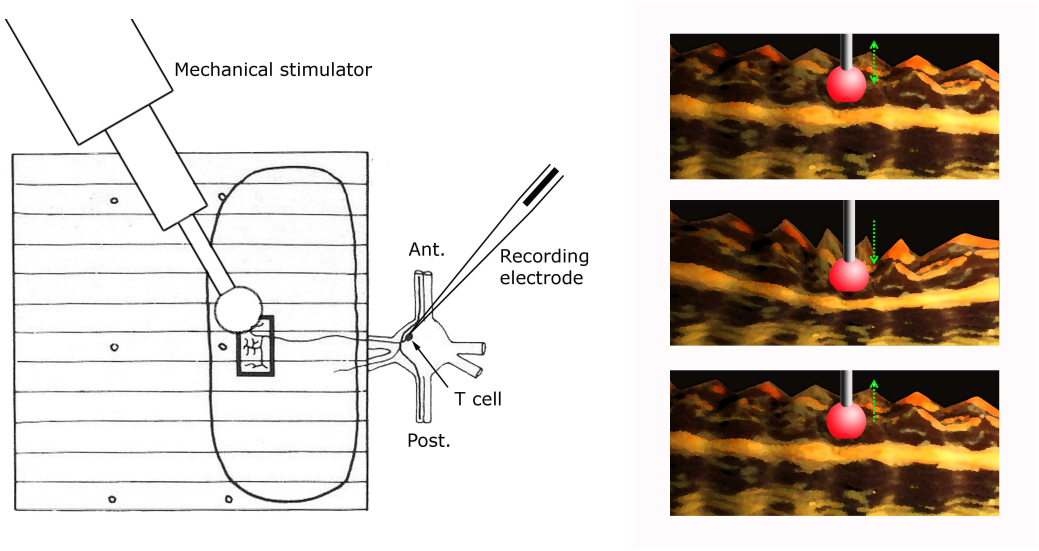

(a) Experimental scheme.

(b) Mechanical Stimulation.

Figure 3.2: **Mechanical stimulation on the skin. a.** Sketch of the experimental preparation while stimulating and recording from the ventral T cell (Modified from Blackshaw, 1981). **b.** Drawing illustrating that tip of the stimulator is always in contact to the skin while stimulating. Photoshop modification from lab pictures.

3.2 Stimulation of T cell

A computer controlled mechanical stimulator was used to elicit the activity of a T cell in response to a indenting object on its receptive field (Figure 3.2a). The basis of this stimulator is a solenoid that makes possible to perform any mathematical function in one dimension (upwards and downwards). The function to be perform is created and controled by a computer program. The computer also receives a feedback from the stimulator, recording the movement of the tip and allowing us to know the real stimulus applied over the skin.

On the tip of the stimulator we put a 3 mm diameter ball, in order to touch the skin without causing any damage. We made sure that the ball was always in contact with the skin during the experiment to guarantee that the stimulus was being applied on the skin at all times (Figure 3.2b). This condition was ensured by testing that the T cell had activity in response to step-like stimulus in all the tip trajectory.

Simple functions (or stimulus inputs) such as pulses, ramps or sines, in which it is possible to control amplitude, duration and frequency, can be quite informative about

the sensory code of T cells. However, this information can be more significant and more efficient using one ideal function scanning randomly a particular bandwidth of frequencies and amplitudes, as it avoids confusion in the analysis caused by adaptation to a repetitive stimulus and there are responses to different values of the stimulus in the same recording. These conditions are satisfied by a white Noise function, that creates a random signal with a flat power spectral density for a given bandwidth in frequencies and ideally has no auto-correlation in the spacial domain.

We have used a Gaussian white noise, whose amplitudes follow a Gaussian distribution, in with standard deviation and cut-off frequency. To build an approximation to this Gaussian white noise with a chosen cut-off frequency, we used the equation

$$wn(t) = A\left[\sum_{i=1}^{N} \alpha_i \cos(\omega_i t) + \beta_i \sin(\omega_i t)\right] + B \tag{3.1}$$

where α_i and β_i are N random numbers taken from a Gaussian probability distribution, ω_i are N random values of frequency with a uniform probability distribution and t is time. A and B are constants to control standard deviation and mean (to force the function to be standard normal: $\mu = 0$ and $\sigma = 1$) . Equation 3.1 was, later on, multiplied by the desired standard deviation.

Equation 3.1 is a pseudo-random white noise that can be performed by the mechanical stimulator as a function that is continuous in time (Figure 3.3a). The real stimulus that is finally applied over the skin is not a perfect white noise and has a small degree of auto-correlation, however it gets very close to a Gaussian probability distribution of stimulus values (Figure 3.3b) and a flat power spectra density up to the cutoff frequency (Figure 3.3c). The mechanical stimulator allows a position range with a maximum of 1 mm with 0.1 μm resolution and a frequency range from 0 to 100 Hz.

3.2.1 Protocols of mechanical stimulation

In order to analyze the role of bursts in the sensory code of T cells, we used 10 minute long pseudo-random stimuli with Gaussian distributions for positions with different variances. Different velocities distribution were achieve by modifying the maximum trajectory of the stimulus and the cut-off frequency. The stimulus maximum trajectory that we used for experiments was 1 mm long (the maximum allowed by the stimulator) and the maximum cut-off frequency, 20 Hz. The standard deviations of the velocity of the stimuli (σ_{vel}) were usually between 0.75 and 9 mm/s.

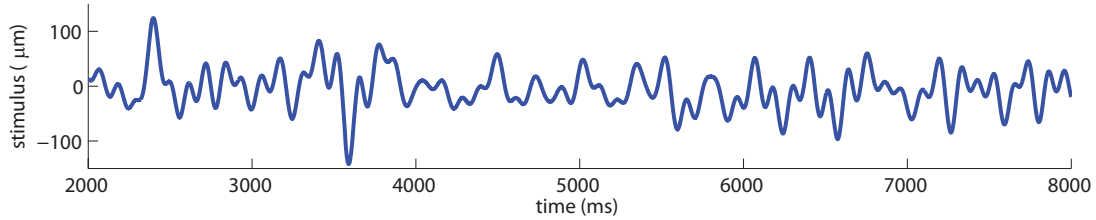

(a) Mechanical Gaussian white noise stimulus.

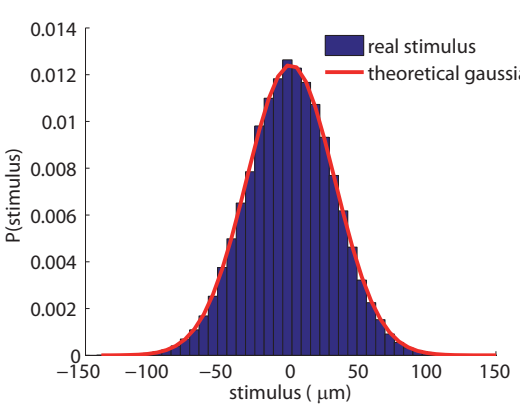

(b) Gaussian distribution of stimulus positions.

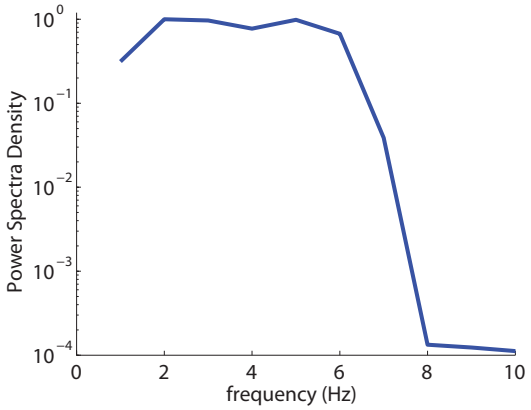

(c) Power spectra density of frequency.

Figure 3.3: **Mechanical "White Noise". a.** 12 seconds of a pseudo-random mechanical stimuli (cutoff frequency: 5 Hz, $\sigma_{\text{posit}} = 32$ μm). **b.** Probability distribution of the same stimulus values compared to a Gaussian with same μ and σ. **c.** Power Spectra Density of this stimulus.

3.3 Use of drugs

To test if the changes in the excitability of the cell membrane could be responsible of the adaptation of T cell sensory code, we used pharmacological blockers of the sodium pump and of the calcium-dependent potassium channels. Sodium pump and calcium-dependent potassium channel are known to produce the after-hyperpolarization of the T cell membrane in response to activity. As hyperpolarization of neuronal membranes usually produce a decay in excitability, we considered that blocking hyperpolarization should block the effect of changes in excitability.

These blockers were first quickly applied to the preparation using a pipette and afterward, at a constant flow of 1 ml/min, using a flow system.

Strophantidin, a reversible blocker of sodium pump (responsible of the 75% of the hyperpolarization), was applied in a concentration of 0.15 mM in extracellular solution (with 1% ethanol to better dissolve the drug, Jansen and Nicholls, 1973). We checked that strophantidin was effective after 15 min, as the hyperpolarization after repetitive stimulation almost disappeared.

We also used apamin, known to block the calcium-dependent potassium conductance in a concentration of 1 nM in the T neurons (Mozzachiodi et al., 2001). We observed its effect as a reduction of 5 mV in hyperpolarization.

Both, strophantidin and apamin, were purchased from Sigma Aldrich.

3.3.1 Mechanical protocols for drug experiments

For the experiments with strophantidin, we used two types of stimulation. One to be sure that the drug has been effective, and another to study the effect of the drug on the adaptive properties of the sensory code.

To test if the drug was effective, the protocol consisted of a 10 seconds train of 40 μm mechanical steps at 1.5 Hz on the skin of the leech, followed by 20 seconds of several 400 μm-amplitude sine-wave patterns at 10 Hz, and then repeating the initial train (Figure 3.4). The first part of the protocol makes the neuron fire a single spike at every 40 μm mechanical step. The second part elicits a strong response in T cell. This strong response has as a consequence a hyperpolarization big enough to avoid, for a variable period of time, the single spike firing in the third part of the protocol. When the blocking of sodium pumps by strophantidin is effective, the hyperpolarization disappears and the cell continues firing in the third part of the protocol.

Next, to study the effect of blocking the sodium pump in the adaptation of the code to stimulus statistics, we applied 3 min of white noise stimulation for two different variances.

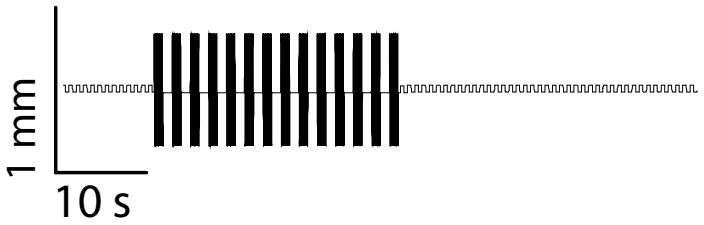

Figure 3.4: **Short protocol to test drugs effect in after-hyperpolarization**. This short protocol is compound of a 10 seconds train of 40 μm mechanical steps at 1.5 Hz on the skin of the leech, followed by 20 seconds of several 400 μm-amplitude sine-wave patterns at 10 Hz, and then another 20 seconds repeating the initial train.

We applied shorter stimulus than the ones we used studying the sensory code, because we typically found 6–9 min of healthy firing. Before the addition of strophantidin, we carried out a control experiment in 1% ethanol (as ethanol was needed to better dissolve strophantidin) using the same stimulation protocol. For these shorter recordings we used σ_{vel} of 1.5 and 2.25 mm/s. Larger variances are more likely to deteriorate the electrophysiology as a result of vibrations, and lower variances show more variability in the neuronal response.

For the experiments with apamin, we also tested the effect of the drug through a protocol showing the reduction of after-hyperpolarization (20 seconds of several 400 μm-amplitude sine-wave patterns at 10 Hz). And to observe the effect of inactivation of the calcium-dependent potassium conductance in the adaptation, 10 minutes white noise stimuli with σ_{vel} of 1.5 and 2.25 mm/s were applied over the skin.

To check the significance of our results we made pair-wise tests after checking that the data were normally distributed (Lillierfors and Jarque-Bera tests, Jarque and Bera, 1980; Lilliefors, 1967).

3.4 Analysis methods

Custom made MatLab software (developed by Raúl Guantes) based on signal discrimination methodologies was used to analyze the electrophysiological recordings. To prove our hypothesis that the T cell uses bursts to code stimulus velocity, we looked for correlations between some characteristic of bursts and the velocity of the stimulus applied to the skin.

The first step consisted in separating bursts in the recorded signal (using ISI distribution, section 3.4.1). Once the bursts were separated, we needed to find the characteris-

tics of the spike activity that correlate to velocity values (using different representations of the stimulus velocity distributions given certain characteristics, sections 3.4.3-3.4.4-3.4.5). When the characteristics were found, the next steps were to test their ability to discriminate velocity values (using Receiver-Operating Characteristics analysis, section 3.4.6) and to analyzed whether the neuronal response was coding any other feature of the stimulus (using Principal Component Analysis, section 3.4.7).

3.4.1 ISI distributions

Inter-spike intervals (ISIs) distributions, obtained by plotting the histogram of all times between spikes (Kepecs and Lisman (2003)), can be used to discriminate different time scales in a spike train. When a neuron fires in bursts, intervals between spikes inside a burst are significantly shorter than intervals between bursts and isolated spikes (Figure 3.5a). As a result of these different time scales, ISIs distributions for bursty neurons show a bimodal appearance (Figure 3.5b). In Figure 3.5b there is a sharp peak for small inter-spikes intervals (around 15 ms, corresponding to intra-bursts ISIs) followed by a wider peak for longer intervals (around 100 ms, corresponding to intervals between bursts).

The fact that these two peaks are distinctly separated allows us to identify intra-bursts ISIs from inter-bursts ISIs by just setting an ISI threshold. Thus, spikes separated by ISIs longer that the threshold are considered to belong to different bursts, while spikes separated by ISIs shorter than the threshold are assumed to belong to the same burst. When ISIs before and after a spike are longer than this threshold, we consider it as an isolated spike.

The cumulative ISI distribution is the probability that the inter-spike time is shorter than a certain value t and is computed as $P_{cum}(t) = \int_0^t P_{ISI}(\tau)d\tau$. This distribution shows a distinct plateau that indicates an appropriate ISI threshold for bursts discrimination. In Figure 3.5c this plateau is around 50 ms.

3.4.2 Spike and Burst-Triggered Average

A first approach to study the stimulus that elicits a neuronal response is to calculated the Spike-Triggered Averaged stimulus, $C(\tau)$ (STA). STA is the average value of the stimulus at time τ before a spike. It can be obtained using equation

$$C(-\tau) = \frac{1}{n}\sum_{\mathrm{i}=1}^{n} s(t_{\mathrm{i}} - \tau),$$

where n is the number of spikes, t_{i} is the occurring time of one spike and τ is time before

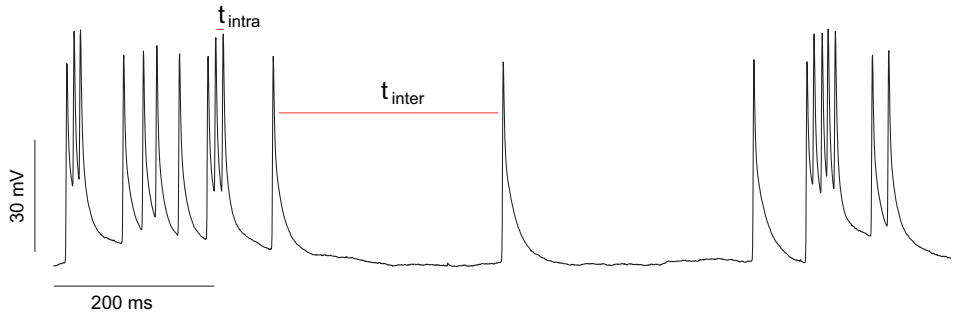

(a) Spike train of a T cell.

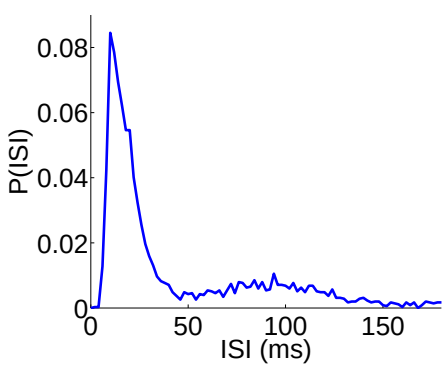

(b) ISI distribution.

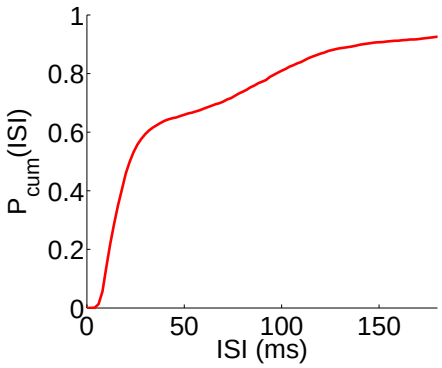

(c) Cumulative ISI distribution.

Figure 3.5: **ISI distribution allow the identification of bursts**. **a**. Spike train in a T cell. We can qualitatively appreciate that there are two different time distribution, one between bursts (t_{inter}) and another between spikes of the same burst (t_{intra}). **b**. Inter-spike interval histogram shows two timescales. **c**. Cumulative ISI distribution. There is a distinct plateau at around 50 ms. (Figures made from a 10 minutes long recording of a T cell stimulated by a mechanical white noise of $\sigma_{vel} = 2.25$ mm/s and with a cut-off frequency of 5 Hz)

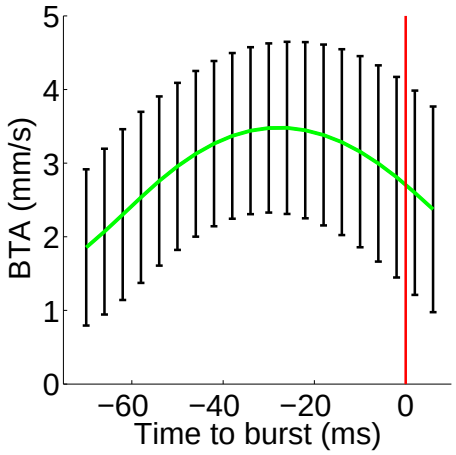

Figure 3.6: **Burst triggered average for bursts of 2 spikes**. Average absolute value of velocity before bursts of 2 spikes (from a 10 minutes long recording of a T cell stimulated by a mechanical white noise of $\sigma_{\text{vel}} = 2.25$ mm/s and with a cut-off frequency of 5 Hz). Error bars are standard deviation. Red vertical line indicates the time 0 (when a burst is elicited).

spike, $s(t_{\text{i}} - \tau)$ is the value of the stimulus at a certain time τ before the spike.

The same equation can be applied for bursts treated as units or for bursts of a given size. We get then the Burst-Triggered Average stimulus (BTA). In Figure 3.6 we can see an example of Burst-Triggered Average stimulus for bursts of two spikes in which we used absolute value of velocity as stimulus.

3.4.3 Probability distribution of velocity values

Instead of the mean value (and standard deviation) of the stimulus at time τ before a spike (STA), we also represented what we called the Spike, Burst or Silence Triggered Probability for velocities (STP, BTP and SilTP respectively). These probabilities are more informative than STA because, when we are not plotting absolute values, different distributions for negative and positives values can be hide behind the average.

Silences are defined as periods between bursts lasting at least 100 ms. As the most probable interval between burst is 100 ms (see section 3.4.1, Figure 3.5b), we consider that if there is an interval between spikes longer than 100 ms it is because there is not a sufficient stimulus to elicit a spike.

STP, BTP and SilTP are the probability distributions of velocity values, v , before spikes of different sizes ($P(v|\text{spike})$), bursts ($P(v|\text{b=n})$, b for bursts, n for number of spikes per burst) and silences ($P(v|\text{silence})$). In Figure 3.7 we can see an example of

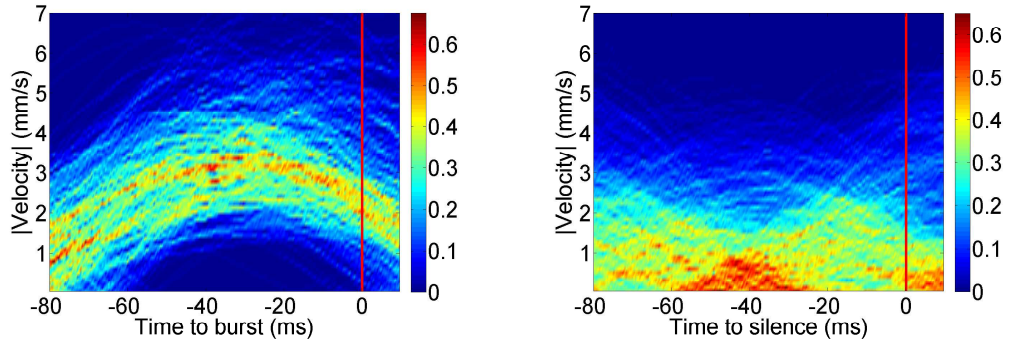

(a) BTP for velocities given b = 2.

(b) SilTP for velocities given a silence.

Figure 3.7: **Burst and Silence Triggered Probability for absolute values of stimulus velocity before bursts of 2 spikes**. These type of figures show the probability of stimulus velocity values at different times before bursts using a color code. Warmer colors mean more probability as shown in colorbars. **a**. BTP for velocities given bursts of 2 spikes. **b**. Silence Triggered Probability for velocities given a T cell silence. (From the recording of Figure 3.6)

BTP for velocities before bursts of two spikes (Figure 3.7a) and of SilTP for velocities before periods of non spiking or silences (Figure 3.7b) from a recording of a T cell that has been stimulated by a mechanical white noise of $\sigma_{\text{vel}} = 2.25$ mm/s and with a cut-off frequency of 5 Hz. More likely values of velocity are in warmer colors (as shown at the colorbars in Figure 3.7). Figure 3.7a shows that from 40 to 20 ms before a burst of two spikes, the most probable velocity is around 2-3 mm/s.

We also represented the probability of velocity values in a time interval before a burst (Figure 3.8). We considered the time of the first spike of a burst as the time in which the burst is fired. We used time intervals before a burst instead of just a time value for two reasons: First, we don't accurately know the exact response time of T cells (if there is any), and second, time intervals improve the statistic as they allow us to have more velocity values. For long recordings (10 minutes long, see section 3.2.1), we took stimulus intervals by either using 20 ms (centered at –15 ms) before the onset of bursting or 20 ms around the maximum response (defined as the most different to 0 mm/s, in Figure 3.8 is between -40 and -20 ms), both of which corresponded to where the coding was more significant. Both intervals give similar results when plotting the probability distributions, as we can see in the main figure of Figure 3.8. Short recordings (3 and 5 minutes long, see section 3.3.1) showed less variability using the second method, and were chosen for the statistical analysis in strophantidin and apamin conditions and their controls.

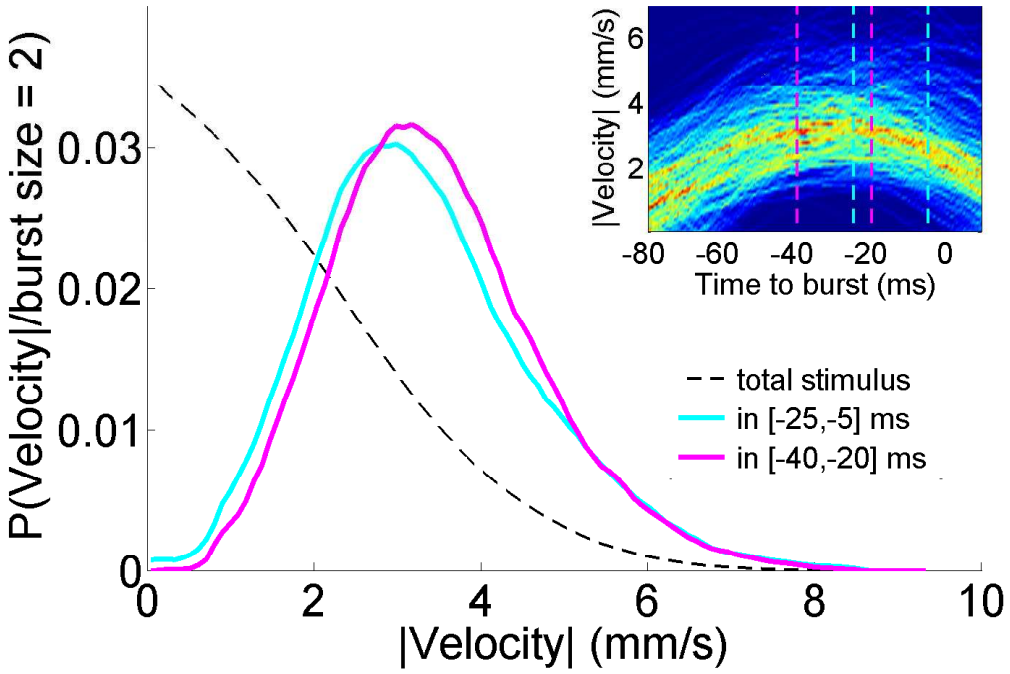

Figure 3.8: **Probability distribution in 20 ms intervals before bursts of 2 spikes**. Probability distributions for absolute values of velocities between 25 and 5 ms (in cyan) and between 40 and 20 ms (in magenta) before bursts of 2 spikes in a recording of a T cell stimulated by a mechanical white noise of $\sigma_{\text{vel}} = 2.25$ mm/s and with a cut-off frequency of 5 Hz. *Inset*: Probability distribution in time (the same as in Figure 3.7) with dashed lines to show the intervals in which the response is being analyzed ([-25,-5] in magenta, [-40,-20] in cyan).

To study the adaptation of the code to the statistical context, we analyzed how these distributions changed when the T cell was stimulated by mechanical white-noises with different σ_{vel}.

3.4.4 Stimulus-dependent and non-dependent firing rate

Calculating probability distributions was our basic methodology to understand coding and adaptation, however to compare our results to others in literature we performed additional analysis considering stimulus-dependent spike and burst rate to construct input/output relationships (Brenner et al., 2000; Maravall et al., 2007). Spike rates take into account every spike in the recording, while burst rates only consider the first spike of every burst.

Stimulus-dependent spike rate, $P(\text{spike}|s)$, and stimulus-dependent burst rate, $P(\text{b}|s)$, are both obtained from Bayes' theorem

$$\frac{P(\text{event}|s)}{P(\text{event})} = \frac{P(s|\text{event})}{P(s)},$$

where, *event* can be a spike or a burst , $P(s)$ is the total stimulus probability distribution and $P(\text{event})$ is the average event rate. $P(s|\text{event})$ can be obtained from the recordings taking the stimulus values before events, as we calculated $P(v|\text{b=n})$.

We were especially interested in understanding the role of bursts in the coding of velocity values, therefore we analyzed $P(\text{b}|v)$ (typically written as $r(v)$), and $P(\text{b})$ (typically written as r_{av}).

Input/output relationships are expressed in literature as normalized rates, $r(s)/r_{\text{av}}$, versus stimulus values (Brenner et al., 2000; Maravall et al., 2007), as this quantity is easily calculated following this method, and also avoids mismatching when comparing different recordings with different r_{av} (mean rate of the whole recording).

We also studied the independent firing rate. All methods to calculate firing rates use a binning and counting procedure that generates an estimation of its value. To avoid bin dependence, we used an approximation of spike and inter-bursts rate based on the inter-spikes intervals (Dayan and Abbott, 2001). This is know as instantaneous spike or burst rate and is calculated for every spikes or burst as 1/ISI or IBI (inter-burst interval).

Input/output relationships were plotted as instantaneous spike or burst rate versus velocities in a 20 ms interval (centered in -15 ms or in time of maximum response, see 3.4.3) before the spike or burst.

Intra-burst rates (rate within a burst) have been calculated as spike-count rate, dividing number of spikes per burst (2 or more) by duration (time from the first spike to the last

one in the same burst).Input/output relationships were plotted as intra-burst rates versus velocities in the 20 ms interval before the burst.

To better visualize the input/output relationship for rate (spike, burst or intra-burst rate), we calculated the mean and standard deviation of rate values for every velocity value.

3.4.5 Stimulus-dependent and non-dependent mean burst size

To study the role of burst-sizes we also calculated the input/output relationship for the mean burst-size (mean number of spikes per burst).

Stimulus-dependent mean burst-size was calculated with the same approach as stimulus-dependent rate. We used equation $\langle b(v) \rangle = \sum_n P(\text{b=n} \mid v) \times \text{n}$ where $P(\text{b=n} \mid v)$ is the velocity-dependent probability for bursts of n spikes computed from Bayes' theorem. As in the case of rates, to compare to previous works in literature, we used normalized burst sizes, $b(v)/b_{\text{av}}$ (where b_{av} is the mean burst-size of the whole recording).

Independent mean burst-sizes were calculated using distribution of burst-sizes in the recording. Input/output relationships for mean burst-sizes have plotted as mean burst-sizes versus velocity values in the 20 ms interval before the burst. Again, to better visualize them, we calculated the mean and standard deviation of mean burst-sizes for every velocity value.

3.4.6 Receiver-Operating Characteristics analysis

In order to quantify the ability of bursts to discriminate stimulus velocities and the importance of burst size in the neuron's coding, we used receiver-operating characteristics (ROC) analysis (Green and Swets, 1966).

The ROC analysis is a method that quantifies the discrimination of values between two probability distributions. It uses two relevant probabilities: probability of false alarm (or false positive) and probability of correct detection (or true positive).

In Figure 3.9 we can see a theoretical example with two populations, A and B. Figure 3.9a shows the probability distributions of a variable x in groups A and B. The question that ROC analysis answers is *"with what probability can we say that $x = x'$ belongs to the B group?"*. Probability of false alarm is the probability of $x = x'$ given A, while probability of correct detection is the probability of $x = x'$ given B (Figure 3.9a). The arbitrary threshold ($x = x'$) is displaced to make the ROC curve (Figure 3.9b), in which we compare probability of correct detection versus probability of false alarm. The area under the ROC curve (AUC) is the quantitative value that determines the quality of the

discrimination (values around 0.5 mean no discrimination). As a qualitative approach, the more bowed is the ROC curve toward the upper left corner, the better is the detection and discrimination.

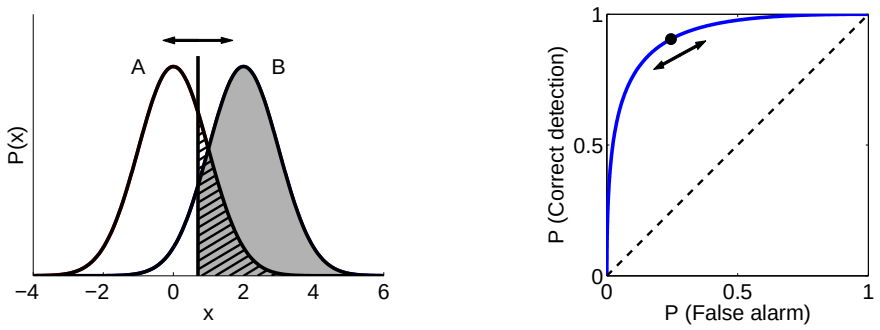

(a) Probability distributions.

(b) ROC curve.

Figure 3.9: **ROC analysis quantifies discrimination**. **a**. Probability distributions of a variable x in two populations or groups (A and B). Dashed area represents the probability of false alarm and gray area, the probability of correct detection. Black vertical line indicates an arbitrary threshold or x value. **b**. ROC curve for these two probability distributions. Black dot indicates the value of probability of correct detection versus probability of false alarm for the arbitrary threshold. (Bidirectional arrow in both figures is used to illustrate that the threshold is slid to construct ROC curve).

In our analysis, we used the ROC curve to discriminate between stimulus velocities based on the observation of the burst size (Gabbiani and C., 1998). We calculated how well bursts distinguish stimulus velocities in comparison to those corresponding to absence of firing. This amounts to analyzing the overlap of probability of correct detection of velocity and the probability of false alarm.

The probability of correct detection of velocity is the probability of stimulus having a velocity value ν given that the neuron fires, $p(\nu|\text{firing})$. The probability of false alarm is the probability of stimulus having a velocity value ν given that the neuron remains silent, $p(\nu|\text{silence})$. They have been calculated using equations

$$P_{\text{Correct detection}} = \int_{\nu_{th}}^{\infty} d\nu \cdot p(\nu|\text{firing})$$

and

$$P_{\text{False alarm}} = \int_{\nu_{th}}^{\infty} d\nu \cdot p(\nu|\text{silence}),$$

where ν_{th} is the velocity threshold separating the velocities to be detected from those that should remain undetected. ν_{th} is usually unknown, and its use is avoided studying the plot of the probability of correct detection versus false alarm for all ν_{th} (the ROC curve). The diagonal of this kind of plot, $P_{\text{Correct detection}} = P_{\text{False alarm}}$, represents the chance level of detection.

3.4.7 PCA analysis

We also quantified whether other stimulus features, apart from velocity, could be also encoded in the T cell's response. That was one of the reasons to use mechanical Gaussian white-noise stimulus instead of a constant or a repetitive stimulus. Gaussian white-noise stimuli present many pattern features, so we can analyze if there are other features apart from velocity that can be important for triggering bursts.

To find other features, we used a dimensionality reduction method known as principal component analysis (PCA). PCA is a mathematical tool that allows identifying patterns in data of high dimensionality. Using PCA, we found the relevant directions in stimulus space preceding burst firing (Oja, 2002).

PCA was mathematically achieved by constructing the covariance matrix of the stimulus before bursts,

$$C_{\mathrm{burst}}(\tau,\tau') = \left\langle s(t_{\mathrm{burst}}-\tau)\cdot s(t_{\mathrm{burst}}-\tau')\right\rangle - \langle s(t_{\mathrm{burst}}-\tau)\rangle \cdot \left\langle s(t_{\mathrm{burst}}-\tau'),\right\rangle$$

where $s(t_{burst}-\tau)$ represents a segment of stimulus velocities of length τ before bursts, and $\langle\,\rangle$ denote averaging over all bursts. The eigenvectors of the covariance matrix are the principal components or relevant stimulus features associated with bursting, and the eigenvalues give the relative contributions of these different components.

We followed a similar approach in which the matrix to be diagonalized is the covariance matrix with the correlation matrix of the whole mechanical stimulus subtracted (De Ruyter van Steveninck and Bialek, 1988; Agüera y Arcas et al., 2003). We took stimulus segments of 220 ms (200 ms before bursts and 20 ms after the beginning of the burst to take into account delays in response) sampled at 2 ms resolution.

3.5 Neuronal model

To simulate T cell responses, we modified a multicompartment model of the T neuron, made by Catarsi and collaborators (Cataldo et al., 2005). A neuronal model doesn't replace a real neuron in the study of a sensory code, but it actually allows to control all

parameters and virtually test the consequences of changes in their values.

A neuronal model makes possible, for example, to study the contribution of the size of the neuron, a parameter that we cannot change in a real neuron. When working with real neurons, blocking ionic currents to test their role involves the use of drugs, and that entails some uncertainties. It is very difficult to be sure that the drug is only affecting the target ionic current. And furthermore, drugs usually compromise the neuronal survival, so the interpretation of results is not always clear. An important advantage of the model, is that these uncertainties can be avoided: it is possible to remove just one ionic current (with no risk of killing the neuron) and then test the pure effect of the absence of this current.

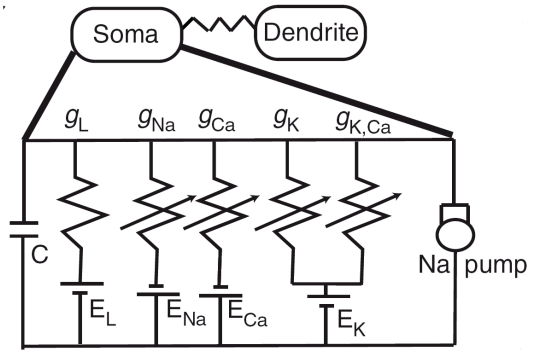

(a) T cell model.

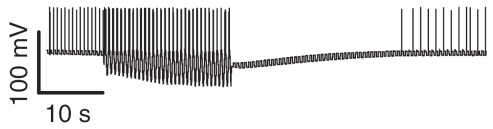

(b) Simulated afterhyperpolarization.

Figure 3.10: **T-cell model neuron.** **a**. Electrical circuit for each of the two compartments (soma and dendrite). Ionic conductances included leakage conductance (g_L), fast Na^+conductance (g_{Na}), delayed rectifier K^+conductance (g_K), high-threshold non-inactivating Ca^{2+}conductance (g_{Ca}), Ca^{2+}-activated K^+ conductance ($g_{K,Ca}$) and Na^+-activated pump current (I_{pump}). **b**. Neuron model response to a square wave stimulation (current step amplitude of 8 nA, period of 1.2 s) triggering 1 spike per period, followed by a sine wave with an amplitude of 40 nA and a frequency of 2 Hz producing higher activity. A refractory period is produced, as in the real neuron, after that high activity.

For simplicity, our model contains just two compartments, a soma/axon and a dendrite (Figure 3.10a), which are known to be sufficient elements to create a bursty neuron

(Krahe and Gabbiani, 2004). They consist of a membrane capacitance, $C = 1$ mF/cm^2 in parallel with two inward currents (a fast sodium current, I_{Na}, and a high-threshold Ca^{+2}current, I_{Ca}), an outward-persistent potassium current, I_{k}, a leak current, I_L, and two currents that are solely regulated by intracellular Na^+ and Ca^{2+} pools, a Ca^{2+}-activated potassium current, $I_{\mathrm{K,Ca}}$, and the sodium pump, I_{pump}. These last two currents are slow outward currents that are modulated by activity and are therefore responsible for different adaptation processes. $I_{\mathrm{K,Ca}}$ is fast (Cataldo et al., 2005; Wang, 1998), and the slower I_{pump} is responsible for the long refractory time after sustained activity (Cataldo et al., 2005) (Figure 3.10b).

3.5.1 Details of the T-cell model

The model has been constructed with differential equations

$$-C\frac{dV_{\mathrm{S}}}{dt} = I_{\mathrm{L}}^{\mathrm{S}} + I_{\mathrm{Na}}^{\mathrm{S}} + I_{\mathrm{K}}^{\mathrm{S}} + I_{\mathrm{Ca}}^{\mathrm{S}} + I_{\mathrm{K,Ca}}^{\mathrm{S}} + I_{\mathrm{pump}}^{\mathrm{S}} + g_{\mathrm{c}}(V_{\mathrm{S}} - V_{\mathrm{D}})/p \tag{3.2}$$

and

$$-C\frac{dV_{\mathrm{D}}}{dt} = I_{\mathrm{L}}^{\mathrm{D}} + I_{\mathrm{Na}}^{\mathrm{D}} + I_{\mathrm{K}}^{\mathrm{D}} + I_{\mathrm{Ca}}^{\mathrm{D}} + I_{\mathrm{K,Ca}}^{\mathrm{D}} + I_{\mathrm{pump}}^{\mathrm{D}} + g_{\mathrm{c}}(V_{\mathrm{D}} - V_{\mathrm{S}})/(1-p) - I_{\mathrm{stim}}, \tag{3.3}$$

where the indexes S and D stand for soma and dendrite, respectively, g_{c} is the electrotonic coupling and p is the ratio of soma to total membrane area. I_{stim} is the stimulation according to Gaussian white noise with a given frequency cut-off and variance.

The voltage activated ionic currents are given by

$$I_{\mathrm{Na}}^{\mathrm{i}} = g_{\mathrm{Na}} {m_{\mathrm{Na}}}^3 h(V_{\mathrm{i}} - V_{\mathrm{Na}}),$$

$$I_{\mathrm{K}}^{\mathrm{i}} = g_{\mathrm{K}} n^2 (V_{\mathrm{i}} - V_{\mathrm{K}})$$

and

$$I_{\mathrm{Ca}}^{\mathrm{i}} = g_{\mathrm{Ca}} m_{\mathrm{Ca}} (V_{\mathrm{i}} - V_{\mathrm{Ca}}),$$

where the index i stands for either soma or dendrite. Conductances and Nernst potentials are the same for both compartments and given by $g_{\mathrm{Na}} = 350$ mS/cm^2, $g_{\mathrm{K}} = 90$ mS/cm^2, $g_{\mathrm{Ca}} = 0.5$ mS/cm^2, $V_{\mathrm{Na}} = 45$ mV, $V_{\mathrm{K}} =$ -62 mV and $V_{\mathrm{Ca}} = 60$ mV.

The activating and inactivating gating variables m, n and h evolve according to first order kinetics as usual, $\frac{dm(V_i)}{dt} = \frac{[m_\infty(V_i) - m(V_i)]}{\tau_m}$, where the asymptotic values and time

constants are given by (Cataldo et al., 2005)

$$m_{\infty,\mathrm{Na}}(V_\mathrm{i}) = \frac{1}{1+e^{-(V_\mathrm{i}+35)/5}} \qquad \tau_{m,\mathrm{Na}} = 0.1$$

$$h_\infty(V_\mathrm{i}) = \frac{1}{\left[1+e^{(V_\mathrm{i}+50)/9}\right]^2} \qquad \tau_h = \frac{13.8}{1+e^{(V_\mathrm{i}+36)/3.5}} + 0.2$$

$$n_\infty(V_\mathrm{i}) = \frac{1}{1+e^{-(V_\mathrm{i}+22)/9}} \qquad \tau_h = \frac{5}{1+e^{V_\mathrm{i}+10/10}} + 1$$

$$m_{\infty,\mathrm{Ca}}(V_\mathrm{i}) = \frac{1}{1+e^{-(V_\mathrm{i}+10)/2.8}} \qquad \tau_{m,\mathrm{Ca}} = 0.6$$

The two currents modulated by the intracellular Ca^{2+} and Na^+ pools are given by

$$I^\mathrm{i}_{\mathrm{K,Ca}} = g_{\mathrm{K,Ca}} k_\mathrm{Ca}(V_\mathrm{i} - V_\mathrm{K})$$

and

$$I^\mathrm{i}_\mathrm{pump} = g_\mathrm{pump} k_\mathrm{Na}(V_\mathrm{i} - V_\mathrm{pump}),$$

where $g_{\mathrm{K,Ca}} = 3$ mS/cm^2, $g_\mathrm{pump} = 0.5$ mS/cm^2 and Nernst potential for the sodium pump $V_\mathrm{pump} = -200$ mV for both soma and dendrite. The dynamics for ion-dependent conductances and ionic concentrations are described as first order processes (Keener and Sneyd, 1998; Yamada et al., 1989)

$$\frac{dk_\mathrm{Ca}}{dt} = \frac{\left[\mathrm{Ca}^{2+}\right] - k_\mathrm{Ca}}{\tau_{\mathrm{k,Ca}}} \qquad \frac{d\left[\mathrm{Ca}^{2+}\right]}{dt} = \frac{-\alpha_\mathrm{Ca} I_\mathrm{Ca} - \left[\mathrm{Ca}^{2+}\right]}{\tau_{\mathrm{i,Ca}}}$$

$$\frac{dk_\mathrm{Na}}{dt} = \frac{\left[\mathrm{Na}^{+}\right] - k_\mathrm{Na}}{\tau_{\mathrm{k,Na}}} \qquad \frac{d\left[\mathrm{Na}^{+}\right]}{dt} = \frac{-\alpha_\mathrm{Na} I_\mathrm{Na} - \left[\mathrm{Na}^{+}\right]}{\tau_{\mathrm{i,Na}}},$$

where time constants for concentration-dependent conductances take the values $\tau_{\mathrm{k,Ca}} = 10$ ms, $\tau_{\mathrm{k,Na}} = 100$ ms for both compartments. Time constants for removal of ions are

$\tau_{\mathrm{i,Ca}} = 1250$ ms, $\tau_{\mathrm{i,Na}} = 16000$ ms for soma, and $\tau_{\mathrm{i,Ca}} = 1000$ ms, $\tau_{\mathrm{i,Na}} = 20000$ ms for dendrite. Note that time constants for sodium ions are one order of magnitude larger than those for calcium to take into account the empirical fact that the decrease in excitability and recovery due to I_{pump} is much slower than the one due to $I_{\mathrm{K,Ca}}$ (Cataldo et al., 2005; Jansen and Nicholls, 1973; Schlue, 1991). The proportion of the ionic currents contributing to the pools of calcium and sodium are given by parameters $\alpha_{\mathrm{Ca}} = 0.1$, $\alpha_{\mathrm{Na}} = 0.016$ for soma, and $\alpha_{\mathrm{Ca}} = 0.2$, $\alpha_{\mathrm{Na}} = 0.16$ for dendrite.

In this model, diffusion of ions between compartments is not described. Moreover, although removal of sodium ions should strictly depend on pump activity I_{pump}, this contribution is very small compared to the influx of sodium due to the fast sodium current, I_{Na} (I_{pump} is of the order of pA while I_{Na} spans tenths of nA). Therefore sodium removal may be modeled using an exponential decay, as described by the dynamics of ionic concentrations.

The electrotonic coupling is $g_{\mathrm{c}} = 1.5$ mS/cm^2 and the ratio of soma to total membrane area by $p = 0.7$. The differential equations for the time evolution of voltage and gating variables, as well as for the ion concentrations and pump conductances were numerically integrated using a fourth order Runge-Kutta method with integration time step of 0.05 ms.

Note that capacitance and all conductances in the model have values in units per surface area, and thus the voltages equations 3.2 and 3.3 are scaled by surface area of each compartment. To express the stimulus current in current units, nA, we assume a dendrite area of 0.1 mm^2.

4
Results

4.1 Bursts Coding for velocity

We argue that T cells detect velocity values of an object indenting the skin. This idea is firstly based on the observation that T cells respond with bursts to the onset and offset of a simple mechanical step-like stimulus (Figure 1.13c in section 1.3). The results that follow show more detailed evidence for a velocity sensory code based on bursts.

4.1.1 T cell spikes detect the absolute value of stimulus velocity

To better characterize the features of the stimulus that elicits firing activity in T cells, we used mechanical Gaussian white noise stimuli and intracellularly recorded the T cell spikes. We then wanted to find whether there was any correlation between the T cell response and the stimulus velocity values. For that, we plotted the probability distributions of velocity values for 100 ms in three different situations (before any time point of the recording, before a spike and before a silence), obtaining a figure where warmer colors mean higher probability (Figure 4.1, see section 3.4.3).

Figure 4.1a shows the probability distributions of the stimulus velocity in the 100 ms before any time point of the recording. By construction, the most likely values in the total stimulus are close to 0 mm/s while higher velocities are very unlikely. Figure

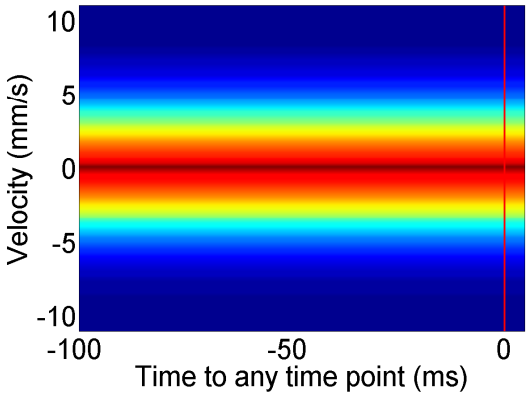

(a) Total stimulus probability at any time.

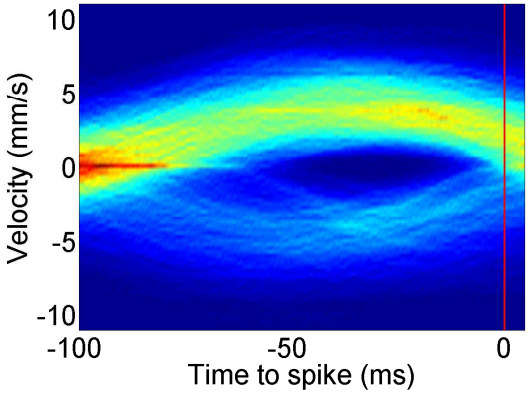

(b) Spike triggered probability for velocities.

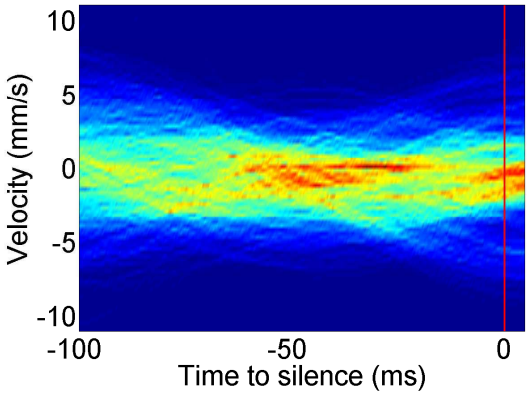

(c) "Silence" triggered probability for velocities.

Figure 4.1: **T cells detect absolute values of velocity.** **a**. Probability distribution of velocities before any time point for a mechanical Gaussian white noise stimulus of a $\sigma_{\text{vel}} = 3$ mm/s and a cut-off frequency of 5 Hz. **b**. Spike Triggered Probability of velocities before a spike (same stimulus as in a). **c**. Silence Triggered Probability of velocities before a silence (same stimulus as in a). Red vertical lines indicates time 0, when a spike is fired or the middle of a silence (plotted in a. for comparative purpose).

4.1b represents the Spike Triggered Probability (STP, described in section 3.4.3) in the 100 ms prior to any T cell spike. In this figure we can see that in an interval from 60 to 5 ms before the spike, most likely velocities are different from 0 mm/s (ranging from 2 to 5 mm/s in absolute value). This is especially significant, as in the total stimulus distribution of velocities these values have a very low probability (compare Figure 4.1a and Figure 4.1b). From these figures we could infer that T cell spikes are actually elicited after 60 to 5 ms of certain velocity values, which are indeed the most unlikely among the velocity values of stimulus.

Figure 4.1c shows probability distribution of the stimulus velocity in the 100 ms before a T cell silence (the Silence Triggered Probability for velocities, SilTP). Silences are defined as periods between spikes lasting at least 100 ms (see section 3.4.3). Red vertical line indicates the mid time in a silence. In Figure 4.1c we can see that velocity values before a silence show a distribution similar to the velocity distribution of the total stimulus. Therefore, silences in T cell do not discriminate between values of velocity.

In Figure 4.1b we can also see two probability plateaus between -60 and - 5 ms. By plateau we should understand a time interval in which velocity values are approximately constant. There is a plateau around 3 mm/s and another around -4 mm/s. Positive values are more likely than negative, and that makes the negative plateau less evident. Both plateaus indicate that T cells are responding to a certain range of positive (tip of the stimulator entering the skin) and negative (tip exiting the skin) values of velocity.

We represented separately the positive and negative velocity stimuli eliciting spikes to better appreciate negative values. Comparing these two probability distributions (Figure 4.2), we find an acceptable symmetry in the velocity values that produced spikes when the skin was being entered and exited. Therefore, we considered for simplicity the absolute value of the velocity as the relevant coded variable.

4.1.2 T cell uses a burst code for velocity values

Most of the T cell spikes appear in bursts of different sizes (different number of spikes per burst) in response to the mechanical stimulation. Figure 4.3 shows an extract from a T cell recording where we can see bursts of different sizes and isolated spikes. In this figure it is also shown the positions and velocities of the stimulus that elicits the bursty activity. Note how bursts are fired after positive and negative slopes in positions, and steady values of velocities (grey areas in Figure 4.3).
Bursts and isolated spikes were identified in the recordings using the distribution of inter-spike intervals (see section 3.4.1). ISI distributions have a first peak indicating the time

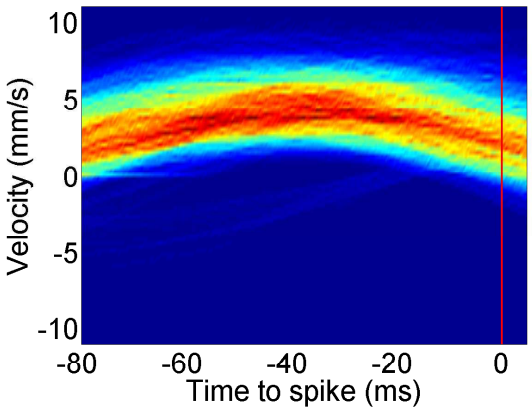

(a) STP for positive values of velocity.

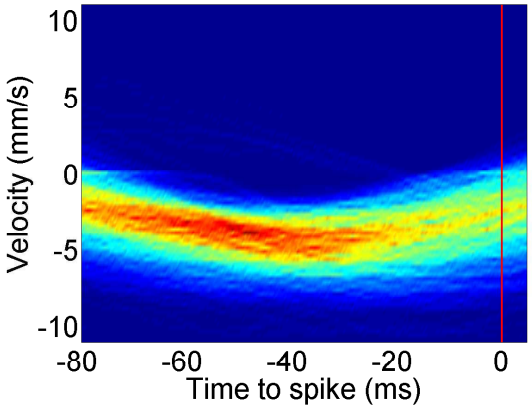

(b) STP for negative values of velocity.

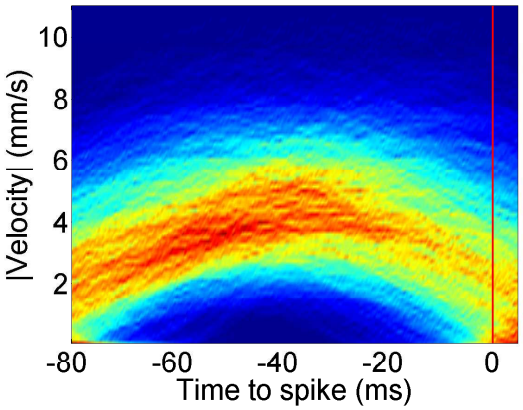

(c) STP for absolute values of velocity.

Figure 4.2: **T cells detect positive and negative velocities.** **a**. STP of positives velocities before spikes. **b**. STP of negative velocities before spikes. **c**. STP for absolute values of velocity. Again red vertical lines indicate the time when a spike is fired. Data from the recording in Figure 4.1.

scale for intra-burst spiking (around 10 ms in Figure 4.4a). The distribution also has a long tail of roughly Poissonian decay (coefficient of variation 1.1) indicating the existence of long uncorrelated inter-burst times. This ISI distribution has a bimodal appearance in which the value of lowest probability between the two modes (around 50 ms in Figure 4.4a) gives a tool to discriminate between burst and isolated spikes. The cumulative ISI distribution also shows a plateau at around 50 ms (Figure 4.4b). This value of 50 ms, very different from that of the intra-burst time intervals (around 10 ms), gives a clear time separation between bursts and isolated spikes. We thus found that bursts were separated by at least 50 ms. We considered then a spike as isolated if it was separated from any other by more than 50 ms, and as part of a burst if it was 50 ms or less close to another. Visual inspection of this procedure confirmed a good separation of bursts.

We found that bursts typically have from 2 to 7 spikes (Figure 4.5) and that the proportion of isolated spikes is just around 13-26% depending on the stimulus variance.

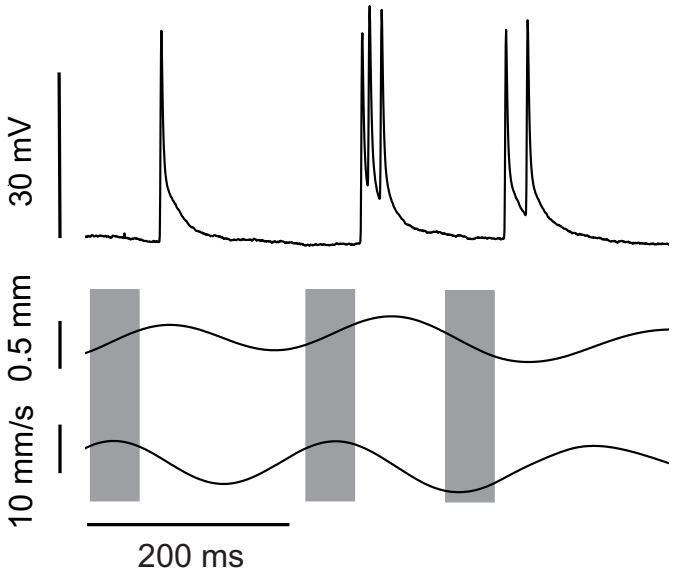

Figure 4.3: **T cell fires bursts of different number of spikes**. *Upper trace*: T cell firing bursts of different sizes in response to an object indenting the skin that goes up and downwards. *Middle trace*: Positions of the tip of the stimulator. *Lower trace*: Velocities of the tip of the stimulator. Grey areas show the relevant stimulus that elicits the burst firing. Data from a T cell response to a mechanical Gaussian white noise stimulus of $\sigma_{\text{vel}} = 3$ mm/s and cut-off frequency of 5 Hz.

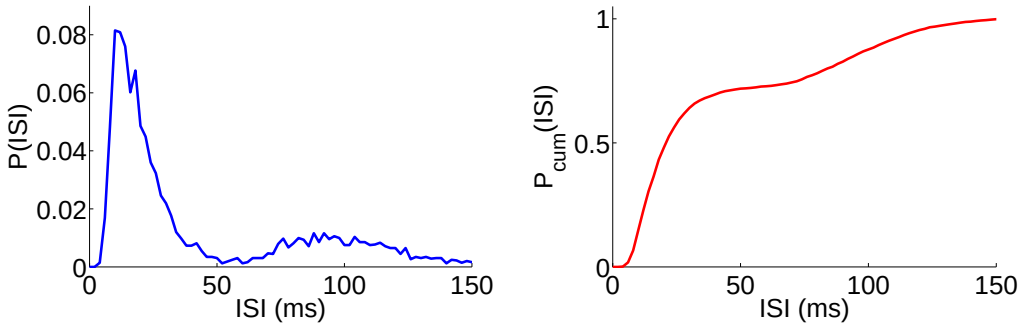

(a) ISI distribution.

(b) Cumulative ISI distribution.

Figure 4.4: **Spikes within bursts are separated by no more than 50 ms. a.** Probability of ISI distribution for a response to a Gaussian white noise stimulus with $\sigma_{\text{vel}} = 3$ mm/s and a cut-off frequency of 5 Hz. **b.** Cumulative ISI distribution, showing a plateau around 50 ms.

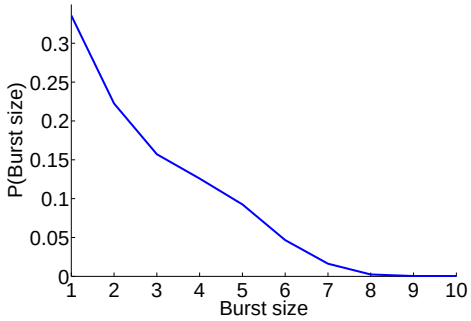

Figure 4.5: **Probability distribution of bursts sizes**. Smaller bursts show higher probability than larger bursts. Data from a T cell recording excited by a mechanical Gaussian white noise stimulus of $\sigma_{\text{vel}} = 3$ mm/s and cut-off frequency of 5 Hz.

4.1.2.1 Burst size code

The Burst Triggered Average for velocities before different burst-sizes (see section 3.4.3), in Figure 4.6a, shows that velocities eliciting different burst-sizes were statistically different. Analyzing the probability distributions of velocities before isolated spikes or a bursts of given size, we confirmed that the neuron responded to increasing stimulus velocity with bursts of increasing size, thus covering the tail of the stimulus velocity distribution (Figure 4.6b). Distributions were calculated for illustrative purposes using the stimulus in the time interval of 5–25 ms before the first spike in the burst (grey area in Figure 4.6a),

but any fixed time or time intervals in the coding region of 5–40 ms before spiking gave similar results (see section 3.4.3).

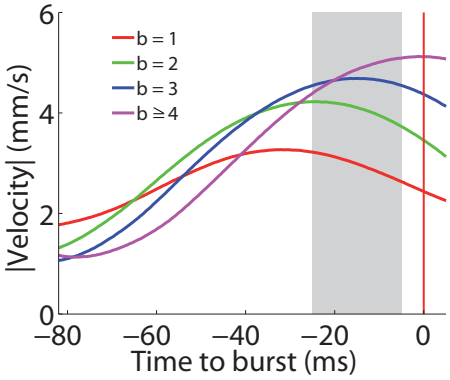

(a) BTA for velocities given different burst-size.

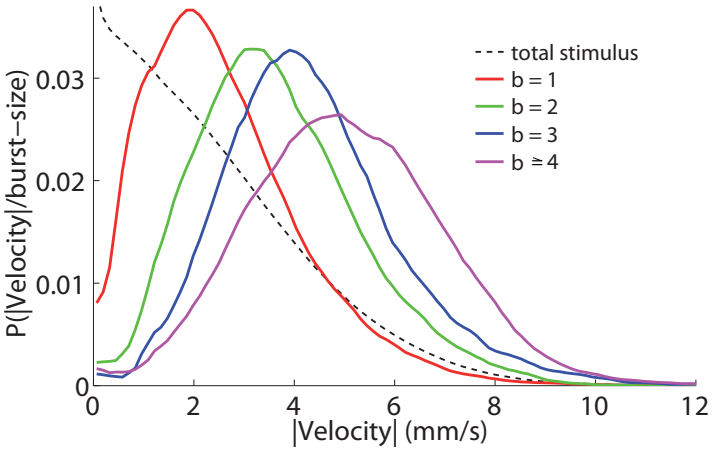

(b) Probability distribution of velocities given different burst-sizes.

Figure 4.6: **Different sizes of bursts code different velocities values. a**. Burst Triggered Average for velocities given isolated spikes (red, b = 1), bursts of 2 spikes (green, b = 2), bursts of 3 spikes (blue, b = 3) and , bursts of 4 or more spikes (magenta, b ≥ 4). Red vertical line indicates time 0 (when the burst is fired). Grey area marks the time interval from where we extracted velocity values to make histograms in b. Standard deviations are omitted for clarity ($\sigma_{b=1} \backsimeq 1.48$, $\sigma_{b=2} \backsimeq 1.53$, $\sigma_{b=3} \backsimeq 1.63$, $\sigma_{b\geq 4} \backsimeq 1.80$). **b**.Velocity distributions before isolated (red), bursts of 2 spikes (green), bursts of 3 (blue) and bursts of 4 or more spikes (magenta). Data from a recording of the response of a T cell to a mechanical Gaussian white noise with a $\sigma_{vel} = 3$ mm/s and a cut-off frequency of 5 Hz.

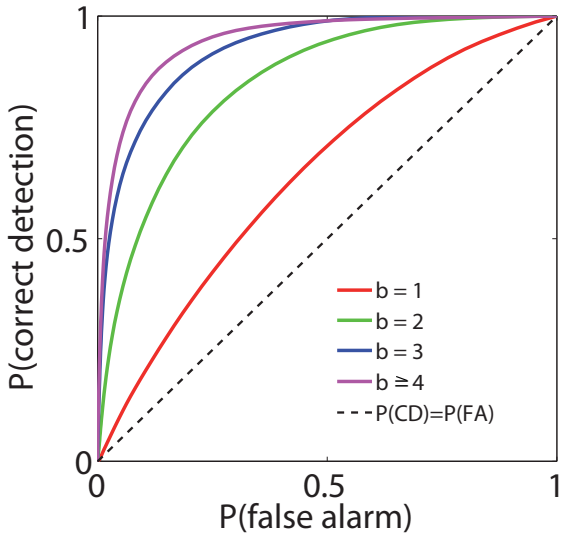

Figure 4.7: **Bigger bursts discriminate velocities values better than smaller bursts.** ROC curves of velocity detection for bursts against periods of silences. Red line is for isolated spikes and shows the worse discrimination. Green line is for bursts of two spikes, while blue is for bursts of 3 and magenta for bursts of 4 or more spikes. As it can be observed, bigger spikes are very good at the discrimination task. Data from a recording of a T cell responding to a mechanical Gaussian white noise whit a $\sigma_{\text{vel}} = 3$ mm/s and a cut-off frequency of 5 Hz.

To calculate the ability of bursts to discriminate between values of stimulus velocity in comparison to periods of non spiking, we carried out an analysis using an ideal observer procedure (ROC analysis, see section 3.4.6). This method quantifies the discrimination of values between two probability distributions, calculating the overlap between the two distributions given the different values of the stimulus. Using ROC analysis we compared the quality of velocity values detection of every burst size. Through this procedure, we found that isolated spikes were poor at this discrimination task, whereas bursts of increasing size performed excellently (Figure 4.7). A similar burst-size code has been previously predicted using biophysical models of pyramidal bursting neurons (Kepecs et al., 2002).

Burst sizes are then playing an important role for coding velocities in T cells. Examining the neuronal gain of burst sizes as a function of stimulus velocity (input/output relation for average burst size, see section 3.4.5), we found that average burst size typically increases with stimulus velocity (Figure 4.8).

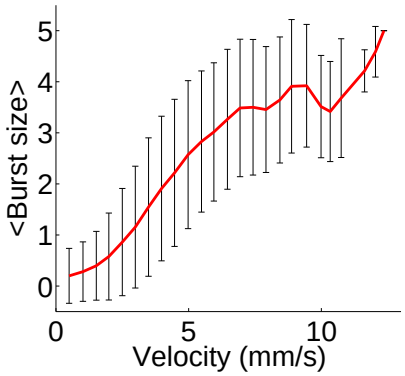

Figure 4.8: **Larger burst sizes code larger velocity values**. Mean burst size as a function of the stimulus velocity. Error bars are standard deviation. D from a recording of a T cell responding to a mechanical Gaussian white noise with a cut off frequency of 5 Hz and a $\sigma_{\text{vel}} = 3$ mm/s.

We conclude that stimulus velocity is actually encoded in the number of spikes per burst, in such a way that longer bursts code for higher velocities.

4.1.2.2 Burst rate code

Burst-size provide a good characterization of the response for the relevant range of coded input velocities. However neuronal codes are usually described by more than a feature of the firing activity. For that reason, we also checked whether the firing rate was able to describe the neuronal gain as a function of the velocity.

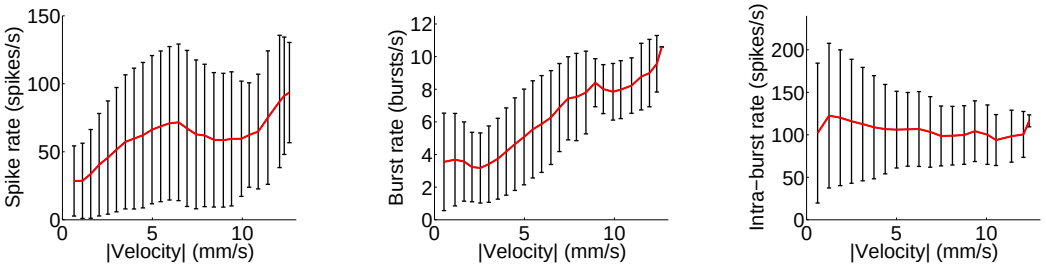

(a) Spike rate per velocity. (b) Burst rate per velocity. (c) Intra-burst rate per velocity.

Figure 4.9: **Burst rate also code velocity**. **a**. Spike rate as a function of the stimulus velocity. **b**. Bursts rate as a function of the stimulus velocity. **c**. Intra-burst rate as a function of the stimulus velocity. Error bars are standard deviation. Data from the same recording as Figure 4.8.

Figure 4.9 shows the input/output relation for spike (Figure 4.9a), burst (Figure 4.9b) and intra-burst rate (Figure 4.9c), calculated as described in section 3.4.4. In Figure 4.9a we can see that the mean spike rate increases with velocity, although there is also a great variability in the response. By contrast, burst rate shows an evident increase with velocity values and small variability. Regarding intra-burst rate, in Figure 4.9c, we can notice that there is no relation between the rate within a burst and the value of velocity eliciting that burst.

We conclude that, apart from burst-sizes, stimulus velocities are encoded by burst rate values. That means that higher velocity values produce a higher frequency between bursts.

4.1.3 T cell also codes other components of the stimulus but poorly

We demonstrated that velocity is a relevant variable coded for by T cell bursts. Even though, we wondered whether it is the only one. The fact that T cell responds just to the onset and offset of a step-like stimulus (Figure 1.13c in section 1.3) indicates that positions are not very relevant for the T cell neuronal code. However, as step-like stimuli are not naturalistic, we used Gaussian white-noise stimuli to analyze the contribution of positions to the code. In Figure 4.10 it is shown the Spike Triggered Probability (SPT, see section 3.4.3) of positions for a 10 minutes recording. We found that focusing in the 60 ms interval before the T cell spikes, the probability of a stimulus position has a slope. This slope indicates that it is the change in positions what is being code, and not the position values.

Once stimulus positions were left out of the coding, we further explored the features of the stimulus that could be coded by bursts. Then we used Principal Component Analysis (see section 3.4.7). PCA is a mathematical method that finds the relevant directions in stimulus space preceding burst firing, in other words, the relevant features of the stimulus that the neuronal response may be coding.

Figure 4.11 gives the two first principal components extracted by this analysis together with the Burst Triggered Average (BTA) for velocities and accelerations. It can be seen that the first component matches with the BTA for velocities while the second matches with the BTA for accelerations. Thus, we found a small acceleration component, around 20-25% of total contribution to bursting versus 70-75% for the velocity component, to which the neuron is also sensitive. The rest of components make a much lower contribution.

We further used ROC Analysis to test the ability of the bursts to discriminate values of stimulus accelerations in comparison to periods of silence. We found a poor discrimina-

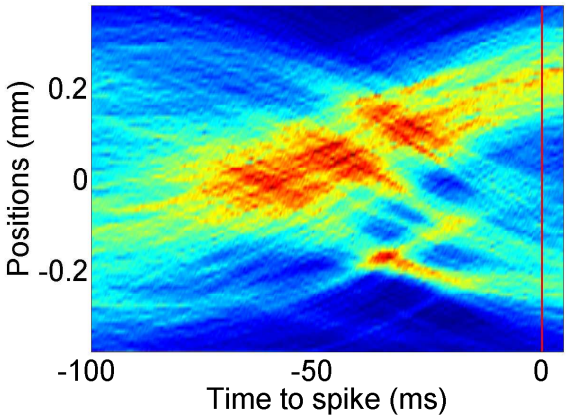

Figure 4.10: **T cell doesn't code for position values**. STP of positions calculated from the same recording of Figure 4.1. Red vertical line indicates time 0 (time when the spike is fired).

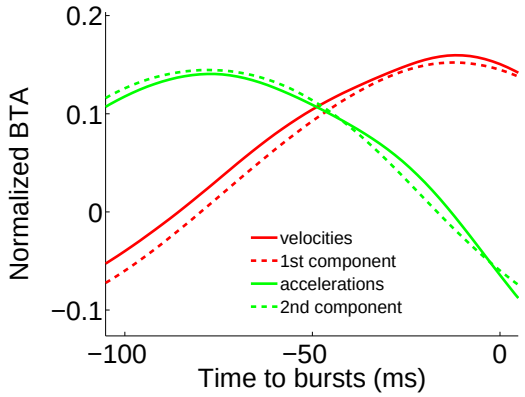

Figure 4.11: **Bursts code mainly for velocity but also for acceleration.** Solid lines represent the burst triggered average for velocity (red) and acceleration (green) values of the mechanical stimulus. Dashed lines represent the first (red; 71.15%) and the second (green; 25.43%) components calculated by PCA. (Data from a recording of a T cell responding to a mechanical Gaussian white noise with a cut-off frequency of 5 Hz and a $\sigma_{\text{vel}} = 3$ mm/s)

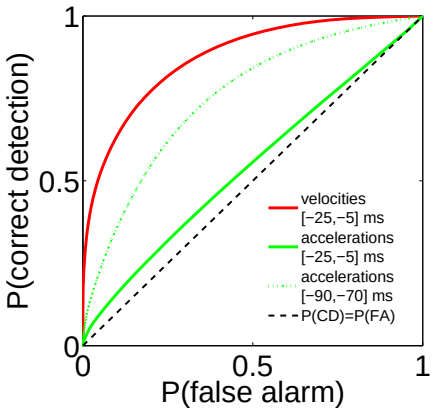

Figure 4.12: **Bursts discriminate much better velocity than acceleration.** Red solid line represents the ROC curve for bursts discrimination of values of stimulus velocity (from 25 to 5 ms before the bursts) in comparison to periods of non spiking. Green solid line represents the same ROC curve but for values of stimulus acceleration. Green dotted line represent the ROC curve for values of stimulus acceleration in a different time interval (from 90 to 70 ms before the bursts). Data from a recording of a T cell responding to a mechanical Gaussian white noise with a cut off frequency of 5 Hz and a $\sigma_{\text{vel}} = 3$ mm/s.

tion for accelerations values as shown in Figure 4.12. The ROC curve for discrimination of velocities (red) in the coding interval (between 25 and 5 ms before the bursts are triggered) performs much better than the ROC curves for discrimination of accelerations (green) in that coding interval and also in the most discriminant interval for acceleration (between 90 and 70 ms before the bursts are triggered). Therefore, even if there is a small acceleration component, bursts of T cell are worse for coding that property of the stimulus than for velocities.

4.2 Adaptation to stimulus statistics in T cells

In the previous section, we have described the sensory code of the T cell. We have shown that it is based on both the number of spikes per burst and the burst rate. However, it is also relevant to know whether it is a flexible code or not. Leeches, as any other animal, have to deal with a changing environment, and a flexible code might be a survival advantage. Therefore, the question is whether the T cell is able to adapt its response to changes in the statistical context of the stimulus.

In the following, we will described the adaptive properties of the T cell response to

different stimulus distributions. We will analyzed the effect on the code of the previous activity and also of the reduction of excitability. Furthermore, we will show that the T cell response adapts to the stimulus variance.

4.2.1 Burst *memory* of previous activity

As it has been demonstrated, different burst-sizes code for different velocity values, but how well this burst-size code discriminates between velocity values? In Figure 4.13a we can see, trough inspection of ROC curves, that burst-sizes coding performs an acceptable discrimination when comparing velocity probability distribution given non consecutive burst-sizes.

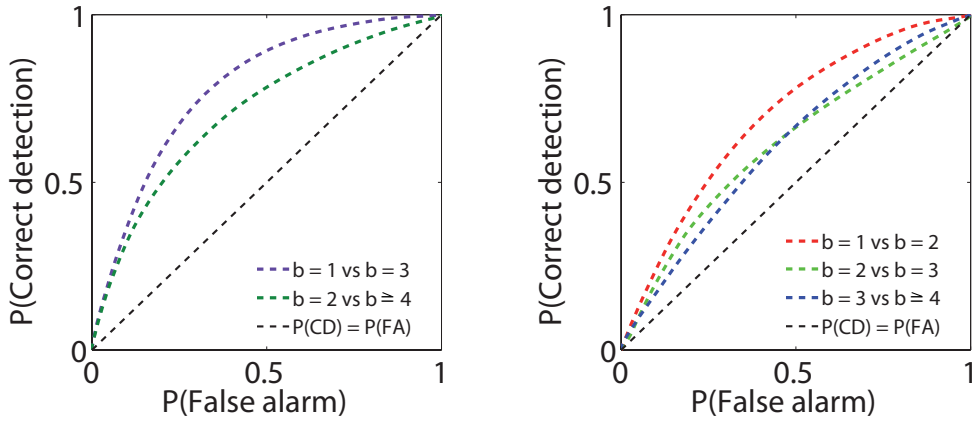

(a) ROC curve for non-consecutive burst-sizes. (b) ROC curve for consecutive burst-sizes.

Figure 4.13: **Discrimination of velocity values. a**. ROC curves for velocity distributions given non consecutive burst-sizes. Purple dashed line: discrimination between velocities detected by isolated spikes and by bursts of 3 spikes. Dark green dashed line: discrimination between velocities detected by bursts of 2 spikes and by bursts of 4 or more spikes. **b**. ROC curves for velocity distributions given consecutive burst sizes. Red dashed line: discrimination between velocities detected by isolated spikes and bursts of 2 spikes. Green dashed line: discrimination between velocities detected by bursts of 2 spikes and bursts of 3 spikes. Blue dashed line: discrimination between velocities detected by bursts of 3 spikes and bursts of 4 or more spikes. Black dashed line: Probability of correct detection (CD) equal to probability of false alarm (FA). Data from a recording of a T cell responding to a mechanical Gaussian white noise with a cut-off frequency of 5 Hz and a $\sigma_{\text{vel}} = 2.25$ mm/s.

However velocity values discrimination gets worse when comparing distribution given consecutive burst-sizes. This was qualitatively observable in the wide overlap of conditioned distributions of velocity (Figure 4.6) and quantitatively, though inspection of the corresponding ROC curves (Figure 4.13b). In the following we will discuss the origin of this overlapping.

Velocity distributions given a certain burst-size are wide and this produces a considerable overlapping between them. We wonder whether the distributions widths could be due to an influence on previous activity on the burst-size. To validate this hypothesis, we tested the influence of the size and timing of the previous burst on the velocity coding of the current burst-size.

Figure 4.14 shows an example for bursts of 2 spikes, although other burst-sizes have been also tested, obtaining similar results. In Figures 4.14a and 4.14b, we see that bursts of two spikes code for smaller velocity values when they are preceded by isolated spikes or bursts of less than 4 spikes and for higher velocity values when preceded by bursts of 4 or more spikes. Velocity distribution before bursts of 2 spikes given the previous burst-size are different enough to be distinguishable by ROC analysis (Figure 4.14c). This observation led us to think that the size of a burst could be coding for the value of the velocity related to the previously detected velocities instead of for the value of the velocity itself.

Using the same example, in Figures 4.15a and 4.15b we can notice that bursts of 2 spikes preceded by silences (defined as inter-bursts intervals larger than 100 ms) code for smaller velocity values than when preceded by inter-burst intervals shorter than 100 ms. Velocity distributions given this conditions are again different enough to be distinguishable by ROC analysis (Figure 4.15c). It seems that the burst-size codes for velocity values related to the velocities detected in a previous time window. No activity means that no relevant velocities have been detected lately, and this causes the threshold to lower, so that smaller velocities have the opportunity to be detected.

This previous activity dependence entails wider and more overlapping velocity distributions, but thanks to it, the neuron has the possibility of making a comparison of the current velocity value to the previous one, coding in such a way the value within a context. This could be just an inevitable consequence of biophysics constrains in the T cell firing activity, however it actually has an important effect on the T cell velocity coding.

4.2.2 Excitability changes in T cell membrane

In the previous section, we saw how the T cell can be coding velocity values that are relevant in the context of the stimulus. This means that the T cell has an adaptive

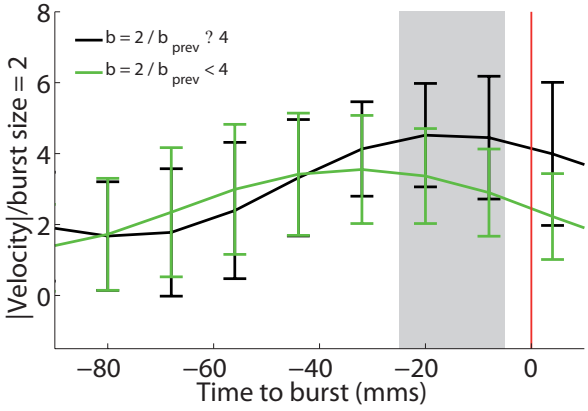

(a) BTA for velocities given bursts of 2 spikes preceded by bursts smaller or larger than 4 spikes.

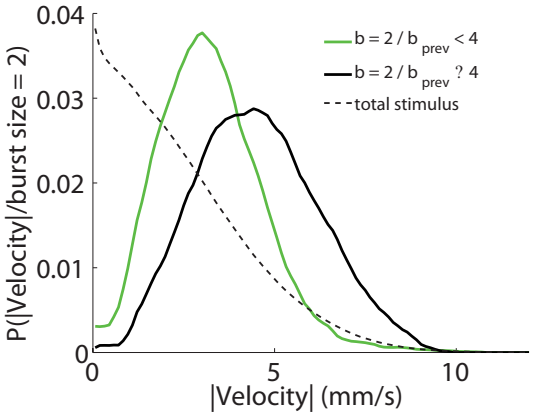

(b) Velocity probability distributions given bursts of 2 spikes preceded by bursts smaller or larger than 4 spikes.

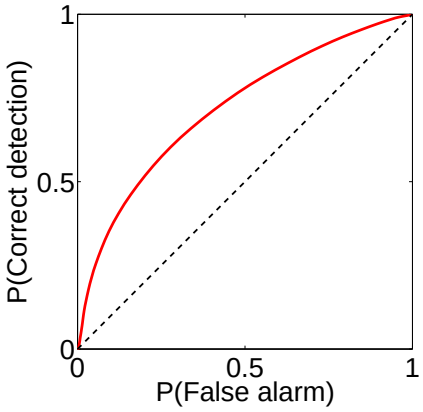

(c) ROC curve.

Figure 4.14: **Burst-size memory of previous burst-size**. **a**. BTA for velocities given bursts of 2 spikes. Dark green line: BTA for velocities given bursts of 2 spikes preceded by bursts of 4 or more spikes ($b_n = 2|b_{n-1} \geq 4$). Light green line: BTA for velocities before bursts of 2 spikes preceded by isolated spikes or bursts of less than 4 spikes ($b_n = 2|b_{n-1} < 4$). Grey area marks the time interval from where we extracted velocity values to make histograms in b. Error bars in a. and c. are standard deviation. **b**. Velocity probability distributions for ($b_n = 2|b_{n-1} \geq 4$) and ($b_n = 2|b_{n-1} < 4$) in the time window of 25 and 5 ms before a burst. **c**. ROC curve for velocity distributions for ($b_n = 2|b_{n-1} \geq 4$) and ($b_n = 2|b_{n-1} < 4$) in the time window of 25 and 5 ms before a burst. Data from the same recording as figure 4.13.

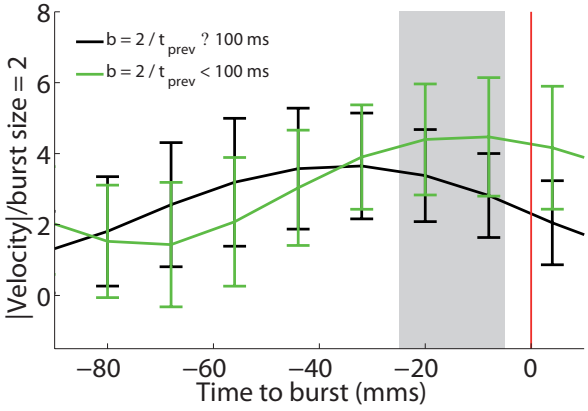

(a) BTA for velocities given bursts of 2 spikes preceded or not preceded by a silence.

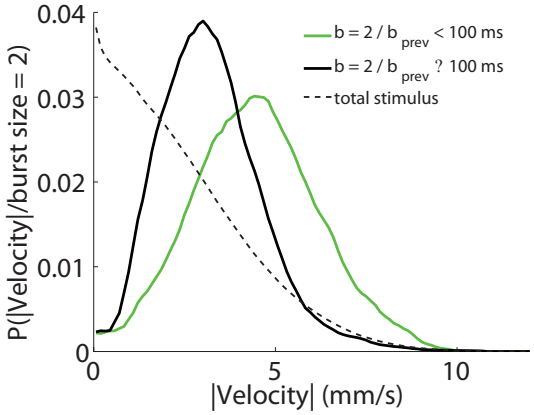

(b) Velocity probability distributions given bursts of 2 spikes preceded or not preceded by a silence.

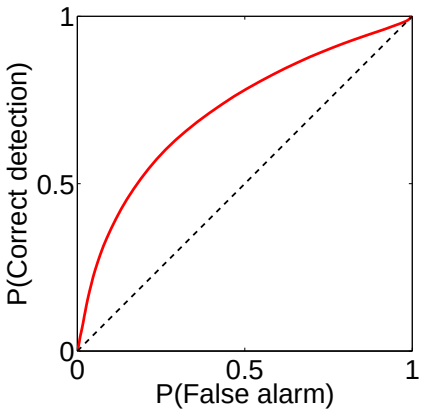

(c) ROC curve.

Figure 4.15: **Burst-size memory of time to the previous burst**. **a**. Dark green line: BTA for velocities given bursts of 2 spikes preceded by a silence ($b_n = 2|t_{\text{prev}} > 100$ ms). Light green line: BTA for velocities given bursts of 2 spikes preceded by an inter-bursts interval smaller than a silence ($b_n = 2|t_{\text{prev}} \leq 100$ ms). **b**. Velocity probability distributions for ($b_n = 2|t_{\text{prev}} > 100$ ms) and ($b_n = 2|t_{\text{prev}} \leq 100$ ms) in the time window of 25 and 5 ms before a burst. Grey area marks the time interval from where we extracted velocity values to make histograms in b. Error bars in a. and c. are standard deviation. **c**. ROC curve for velocity distributions for ($b = 2/t > 100^{\sim}$ms) and ($b = 2/t = 100^{\sim}$ms) in the time window of 25 and 5 ms before a burst. Data from the same recording as figure 4.13.

response at least in a short term scale. We thought that the T cell sensory code could also present adaptation to statistics in a longer term scale. To prove this idea, we first needed to test if there were changes in the excitability of this neuron when exposed to long stimuli with different probability distributions of velocities.

The T cell, mainly due to the action of the sodium pumps, hyperpolarizes its membrane in response to activity. T cell membrane hyperpolarization, in turn, produces a reduction in the firing rate, as mentioned in section 1.3.2. To increase the firing activity, the neuron has to be stimulated with a stronger stimulus. In the case of the T cell, a stronger stimulus means a stimulus presenting higher velocities. This fact led us to think that hyperpolarization and the consequent reduction in firing activity could be depending on the velocity variance. To test this hypothesis we recorded the spiking activity of a T cell while the skin was being stimulated with Gaussian white-noise distributions of displacements with different standard deviations.

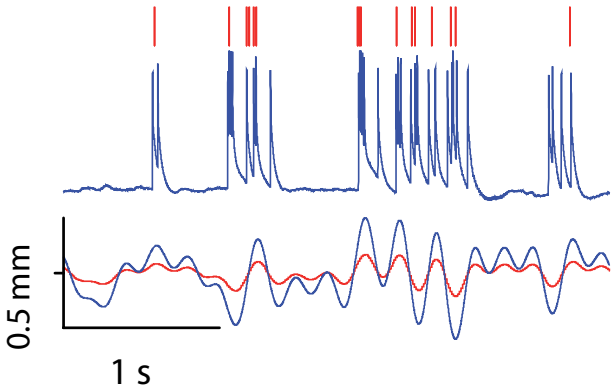

Figure 4.16: **T cell response to two mechanical Gaussian white noise stimuli of different $\sigma_{\mathbf{vel}}$.** Voltage responses of the T cell (*top*) when the skin was stimulated with Gaussian white noise distributions of displacements with a cutoff frequency of 5 Hz and two different standard deviations (*bottom*, red lines, $\sigma_{\text{posit}} = 0.0425$ mm and $\sigma_{\mathbf{vel}} = 0.75$ mm/s; blue lines, $\sigma_{\text{posit}} = 0.1275$ mm and $\sigma_{\mathbf{vel}} = 2.25$ mm/s).

It is illustrative, as a qualitative approach, to consider the raw spike trains that are produced by the neuron after it has been stimulated for several minutes and therefore the response can be already adapted. In Figure 4.16 (*top*) we can see that, as we described in section 4.1, the neuron preferentially responded with bursts of spikes to slope in stimulus position (stimulus velocity). Notably, the firing characteristics for the two stimulus distributions were similar, despite their large difference in variance (compare blue spike train to red schematic spikes, in Figure 4.16 *top*). This is possible because

the neuron was more hyperpolarized for larger $\sigma_{\mathbf{vel}}$ of the mechanical stimuli (23 mV for $\sigma_{\mathrm{vel}} = 0.75$ mm/s, in red, and 27 mV for $\sigma_{\mathrm{vel}} = 2.25$ mm/s, in blue), and therefore was in a state of reduced excitability. For the same value of stimulus velocity, there was less response when the stimulus distribution had larger $\sigma_{\mathbf{vel}}$.

We quantified the dependence of hyperpolarization and reduction of excitability on σ_{vel} (Figure 4.17). In Figure 4.17a it is shown for the response to two different velocity distributions (blue, $\sigma_{\mathrm{vel}} = 0.75$ mm/s and red, $\sigma_{\mathrm{vel}} = 2.25$ mm/s) how the hyperpolarization, ΔV, increases with time when the T cell is being stimulated, but also reaches stationary values after 1 minute of stimulation. As we can see in this figure, the stationary value of ΔV is larger for larger values of σ_{vel}. Figure 4.17b shows the different stationary values of ΔV for T cell responses to velocity distributions with different σ_{vel} (ranging from 0.75 to 6.3 mm/s). Stationary values of ΔV increase with increasing stimulus velocity, σ_{vel}, reaching a top value around 28 mV at σ_{vel} of 2.25 mm/s.

Figure 4.17c shows the decrease with time of the firing rate, expressed as r_{av}. As we can see for the same two recordings of Figure 4.17a (cut-off frequency of 5 Hz for both and σ_{vel} of 0.75 mm/s in red and of 2.25 mm/s in blue), at the start of stimulation, r_{av} was higher for larger σ_{vel}. During the first 10 s there is an abrupt decay in the r_{av}, followed by a slower decay for approximately 1 min until stationary firing is reached. Larger reduction of excitability with increasing σ_{vel} is then apparent in the firing rate.

To see this more detailed, we also calculated the initial average firing rate, r_{av}, for the first second of stimulation as a function of the σ_{vel} (Figure 4.17d). The initial rate was higher with increasing σ_{vel} until a value of around 40 spikes/s at σ_{vel} of 6.3 mm/s (Figure 4.17d, full circles). We also calculated the r_{av} when the response of the neuron was adapted after 10 min of stimulation. This rate was smaller and depended less on σ_{vel}, reaching a value of 13 spikes/s for $\sigma_{\mathrm{vel}} > 2.25$ mm/s (Figure 4.17d, white squares). The reduction of excitability can be calculated as the difference between the initial spike rate and the spike rate when the neuron was adapted, $r_{\mathrm{av}}(t = 1\ \mathrm{s}) - r_{\mathrm{av}}(t = 10\mathrm{min})$, which increases with σ_{vel} and varies between 0 and 27 spikes/s.

For the Figure 4.17 we used cut-off frequencies of 5, 10 and 20 Hz, and we found that neither the hyperpolarization values nor the reduction in excitability depended substantially on the value of the cut-off frequencies; instead they depended only on σ_{vel}. The dynamics of adaptation were also found to be on the order of 1 min for the range of the stimulus cut-off frequencies considered in Figure 4.17.

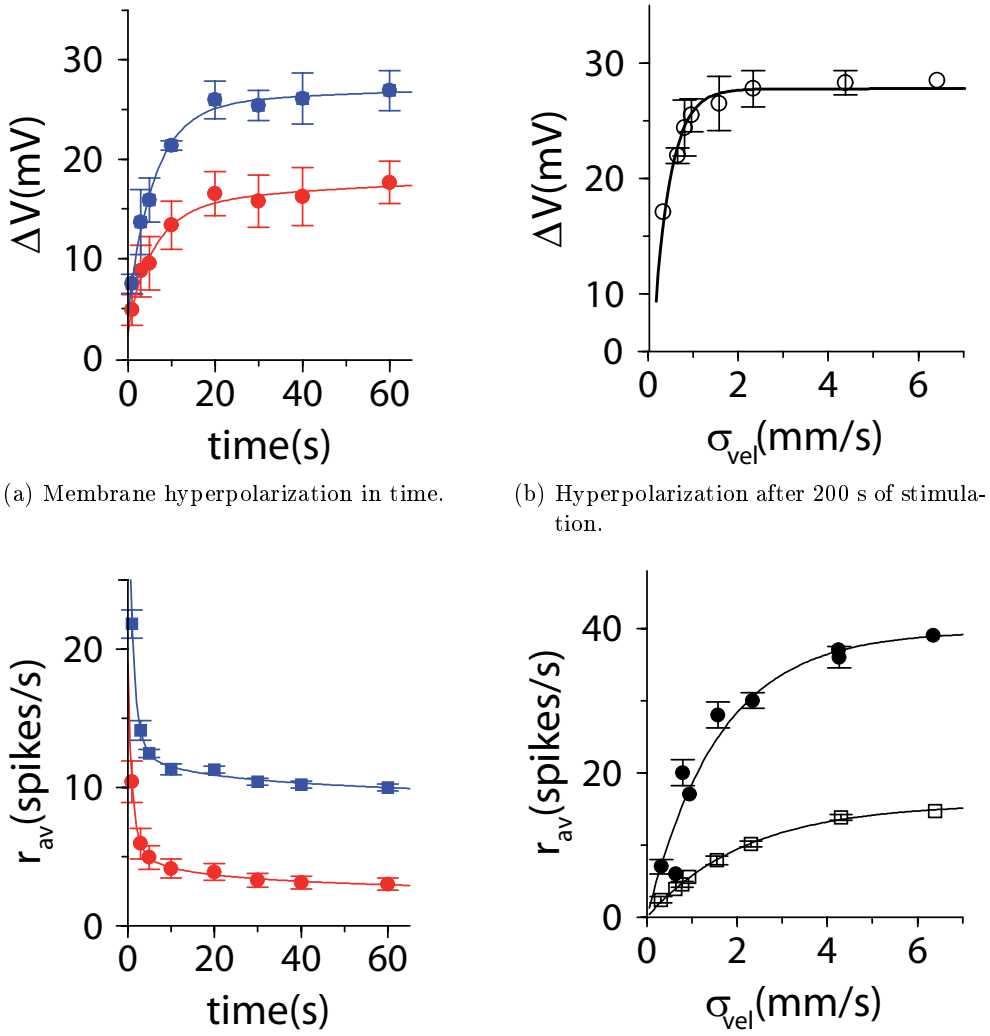

(a) Membrane hyperpolarization in time.

(b) Hyperpolarization after 200 s of stimulation.

(c) Rate average in time.

(d) Rate average at different times.

Figure 4.17: **Excitability of T cell is reduced with increasing $\sigma_{\mathbf{vel}}$. a**. Dynamics of membrane voltage for the stimulus ensembles in Figure 4.16(red circles, $\sigma_{\mathrm{vel}} = 0.75\tilde{}\mathrm{mm/s}$; blue squares, $\sigma_{\mathrm{vel}} = 2.25\tilde{}\mathrm{mm/s}$) . **b**. Increase in membrane hyperpolarization after 200 s of Gaussian white noise stimulation as a function of σ_{vel}**. c**. Dynamics of the average spike rate for the stimulus ensembles in Figure 4.16 . **d**. Average spike rate as a function of σ_{vel} (full circles represent average spike rate in the first second; empty squares represent the average firing rate after 10 min of stimulation). Solid lines are fits to exponential curves $y = a(1–e^{-bx})$. (For b and d, solid lines are fits to exponential curves $y = a(1–e^{-bx})$. For a and c, solid lines are fits to exponential and power-law growth/decay, $y = a(1–e^{-bx}) + cx^d$ and $y = ae^{-bx} + cx^d$, respectively. Error bar are standard deviations)

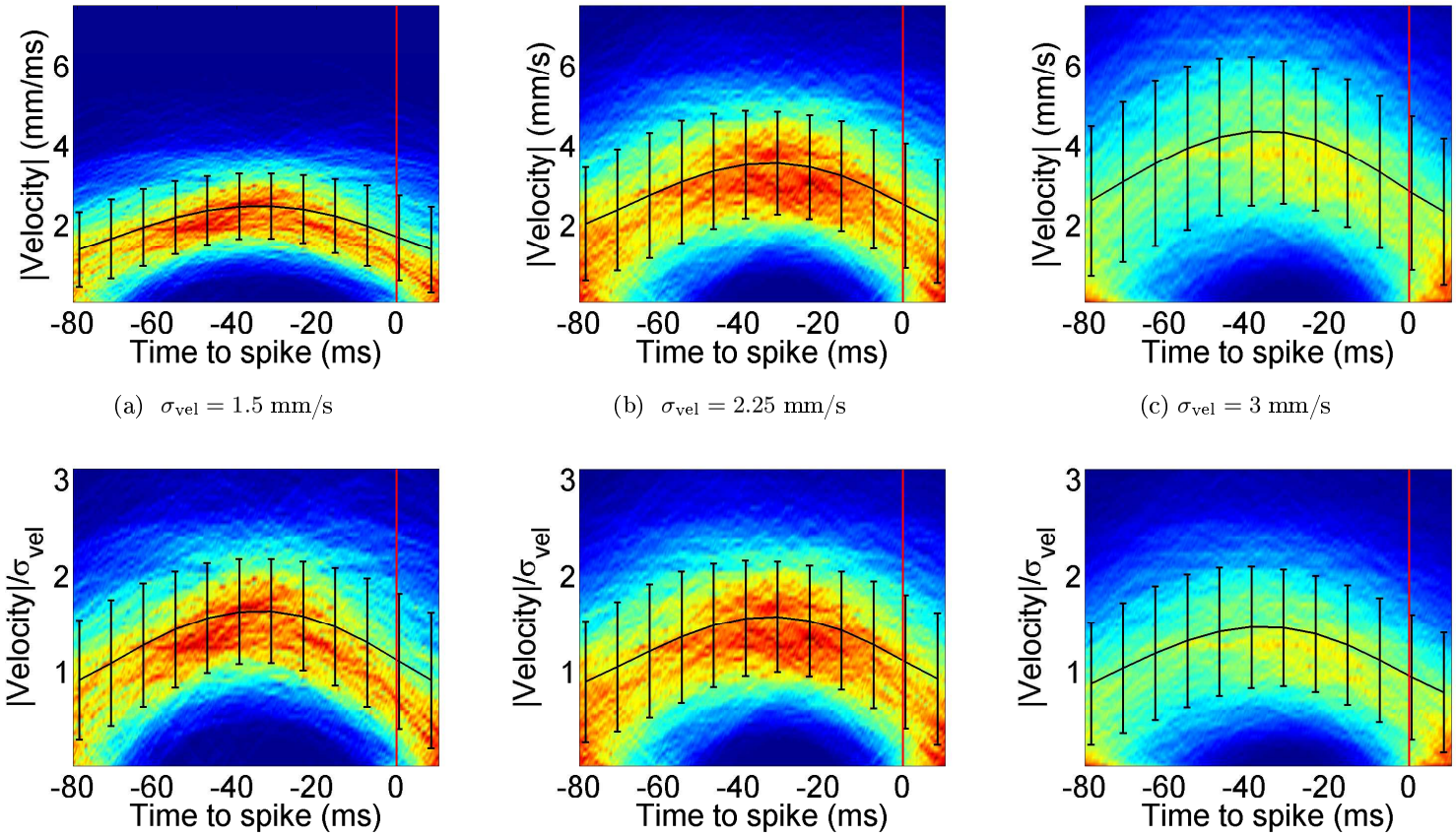

(a) $\sigma_{\text{vel}} = 1.5$ mm/s (b) $\sigma_{\text{vel}} = 2.25$ mm/s (c) $\sigma_{\text{vel}} = 3$ mm/s

(d) $\sigma_{\text{vel}} = 1.5$ mm/s (e) $\sigma_{\text{vel}} = 2.25$ mm/s (f) $\sigma_{\text{vel}} = 3$ mm/s

Figure 4.18: **T cell response adapts to σ_{vel}.** STP of velocity values in response to a white noise with a cut-off frequency of 5 Hz and **a**. $\sigma_{\text{vel}} = 1.5$ mm/s; **b**. and $\sigma_{\text{vel}} = 2.25$ mm/s; **c**. and $\sigma_{\text{vel}} = 3$ mm/s. **d**. **e**. and **f**. Same as a, b and c but with STP of velocity values scaled by σ_{vel}. Vertical red lines indicate time 0 (time when a spike is fired). Black solid lines represent the mean values of velocity and error bars are standard deviation.

4.2.3 T cell response adaptation to the standard deviation of stimulus velocity distribution.

As shown in section 4.2.2, the T cell membrane shows an increase in hyperpolarization and a decrease in excitability in proportion to stimulus velocity standard deviation. How does this change in excitability affect the T cell sensory coding? To answer this question we studied the activity of T cell in response to stimuli with different velocity standard deviations.

In Figure 4.18 we can see, through inspection of the spike triggered probability of velocities (STP, see section 3.4.3), how T cell changes its response to increasing velocity standard deviation (σ_{vel} = 1.5, 2.25 and 3 mm/s) moving the conditional velocity distributions, $P(v|\text{spike})$ toward increasing values of velocity . Figures 4.18d-e show the same STP of velocities as Figures 4.18a-b but with velocity values scaled by the σ_{vel} of every stimulus. Distributions of non scale velocity are clearly different, but distributions of σ_{vel}-scaled velocities are practically identical.

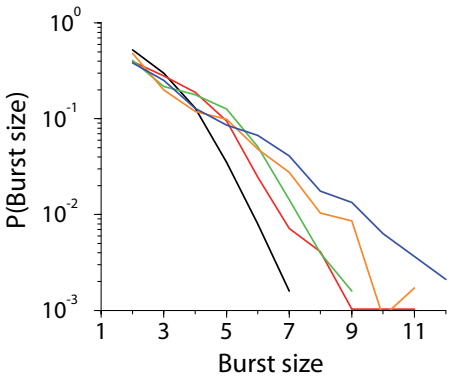

Figure 4.19: **Similar distribution of burt sizes in response to different σ_{vel}.** Probability distributions of burst size for 10 min long responses to stimulus ensembles of different standard deviations. (σ_{vel} = 0.75 (black), 1.5 (red), 2.25 (green), 3 (orange), 4.5 (blue) mm/s; green and blue correspond to a cut-off frequency of 10 Hz and the rest, to a frequency of 5 Hz)

This scaling could be due to an adaptation of the T cell response to the standard deviation of the stimulus velocity distribution. However, two scenarios are possible. First, in the case of a non-adaptive sensory code, the conditional velocity distributions could also change if the proportion of larger bursts increased with σ_{vel} while the proportion of smaller bursts decreased. Second, in the case of an adaptive sensory code, the conditional velocity distributions should changed while the proportion of every burst size should stay similar. When analyzing the distribution of burst sizes for different stimulus variances,

we realized that the proportion of every burst size stays similar until values of 5 or 6 spikes per burst (Figure 4.19). In all cases, larger bursts are much less probable. Without adaptation we would expect an increase of the probability of finding longer bursts relative to short bursts as stimulus velocity variance increases. Instead, what we found is an approximately exponential decay of the burst size probability for all stimulus variances.

To further prove that the T cell response adapts to the stimulus variance, we analyzed the adaptive properties of the T cell sensory code. We have shown, in section 4.1.2, that stimulus velocity is coded for in burst size and burst rate. Isolated spikes respond to values of stimulus velocity close to those corresponding to silences (Figures 4.6b and 4.7). We have thus concentrated on adaptive scaling of bursts as they show an excellent ability to discriminate velocities different to those corresponding to silences.

Taking as an illustrative example bursts of two spikes, we can see in Figure 4.20a how the velocities coded by bursts of two spikes are higher for larger σ_{vel}. This figure shows the burst triggered average of velocities (BTA, see section 3.4.3) prior to burst of two spikes. To examine the dependence of σ_{vel}, we again plotted the BTA in Figure 4.20a, but this time as a function of the ratio of the stimulus velocity to the σ_{vel}. We found that when velocities are scaled by σ_{vel}, bursts of two spikes code for very similar values of scaled velocities (Figure 4.20b). That means that the T cell is able to adapt its code to the statistics of the stimulus. Indeed, the relevant scaling parameter was found to be σ_{vel}.

To show more detailed evidence about this adapting scaling to σ_{vel}, we analyzed the adaptive properties of the response of the T cell to stimulus ensembles with five different σ_{vel} (0.75, 1.5, 2.25, 3 and 4.5 mm/s). Instead of the BTA, we plotted the conditional velocity distributions in an interval of 20 ms before bursts of two spikes ($P(v|\mathrm{b{=}n})$, see section 3.4.3). We again found that bursts of two spikes were produced in response to higher velocities for larger standard deviation of the stimulus distribution (Figure 4.21a). We also plotted the probabilities in Figure 4.21a as a function of the ratio of the stimulus velocity to the σ_{vel}. These probabilities of σ_{vel} -scaled velocities were found to be similar and, therefore, independent of the stimulus variance (Figure 4.21b).

This adaptive scaling was found for other burst sizes and even for isolated spikes, as shown in Figure 4.22. We concluded then that bursts of a given size were produced in response not to stimulus velocity, but to the ratio of velocity and the standard deviation of the velocity distribution. Note that the different stimulus ensembles have different σ_{vel} and also two different cut-off frequency (5 and 10 Hz, see legend of Figure 4.19). The adaptive scaling was found to be independent of the cut-off frequency.

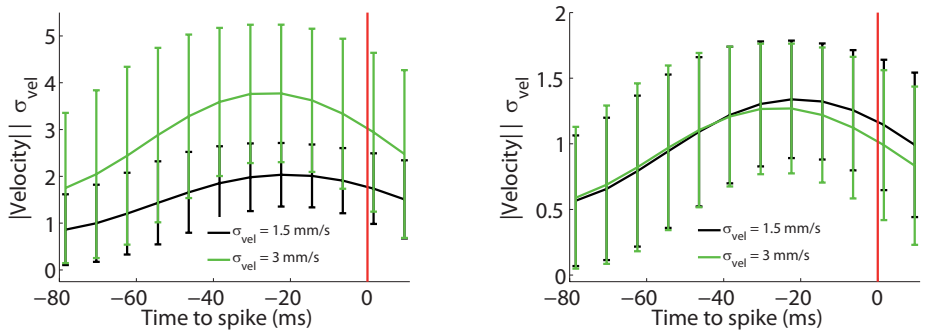

(a) BTA of velocities | b = 2.

(b) BTA of σ_{vel}- scaled velocities | b = 2.

Figure 4.20: **BTA for velocities given bursts of 2 spikes**. **a**. Burst Triggered Average of velocities prior to bursts of 2 spikes for two different velocity distributions (cut-off frequency = 5 Hz and σ_{vel} = 1.5 mm/s, light green, and 3 mm/s, dark green). **b**. Same as in a but with velocity values scaled by σ_{vel}. Vertical red lines indicate the time when a spike is fired. Error bars are standard deviation.

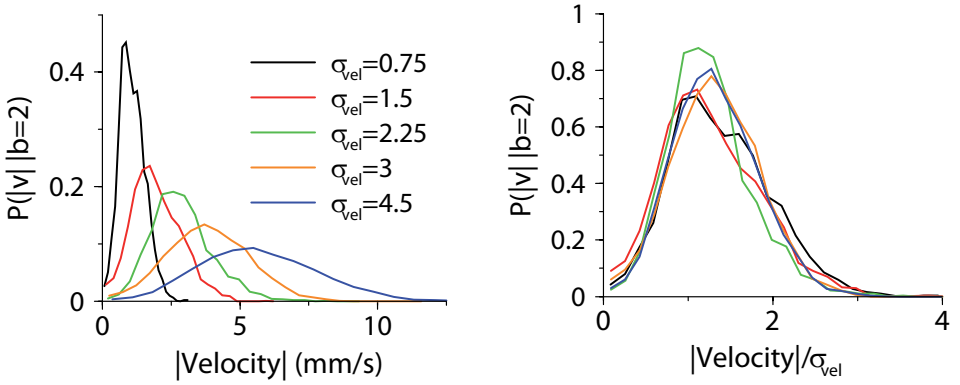

(a) Velocity distributions given b = 2.

(b) σ_{vel}-scaled velocity distributions given b = 2.

Figure 4.21: **Velocity distributions given bursts of two spikes show adaptive scaling to σ_{vel}**. **a**. Velocity distributions before bursts of two spikes for different stimulus ensembles. **b**. Same as in a, but with velocity divided by σ_{vel}. (Same stimulus ensembles as in Figure 4.19)

The same scaling was also found in the input-output functions. The normalized (by the mean burst-size) burst sizes in response to stimulus velocities were different depending on the stimulus variance (Figure 4.23a). The same normalized burst sizes, were instead produced in response to the ratio of velocity and σ_{vel} (Figure 4.23b). Normalized (by the mean burst rate) burst rates showed the same scaling relationship. Similarly to the case of normalized burst sizes, normalized burst rates for different input variances were elicited proportionally not to absolute velocity values (Figure 4.23c) but to velocities that were relative to the σ_{vel} (Figure 4.23d).

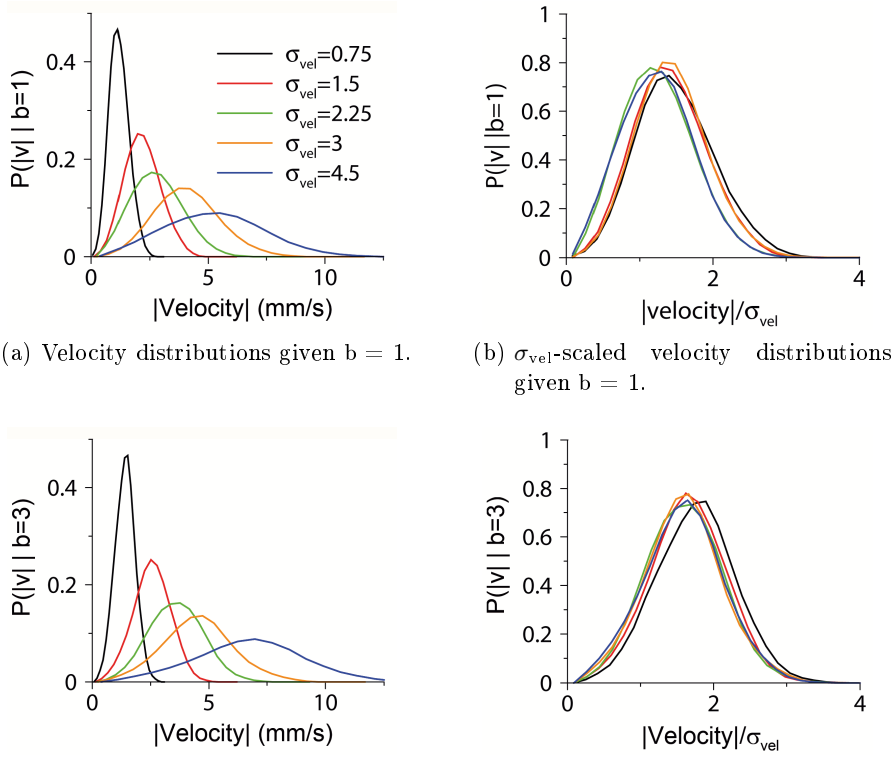

(a) Velocity distributions given b = 1.

(b) σ_{vel}-scaled velocity distributions given b = 1.

(c) Velocity distributions given b = 3.

(d) σ_{vel}-scaled velocity distributions given b = 3.

Figure 4.22: **Velocity distributions given other burst-sizes also show adaptive scaling to σ_{vel}.** **a**. Velocity distributions before isolated spikes for different stimulus ensembles. **b**. Velocity distributions as in a, but with velocity divided by σ_{vel}. **c**. and **d**. as a and b but for bursts of 3 spikes. (Same stimulus ensembles as in Figure 4.19)

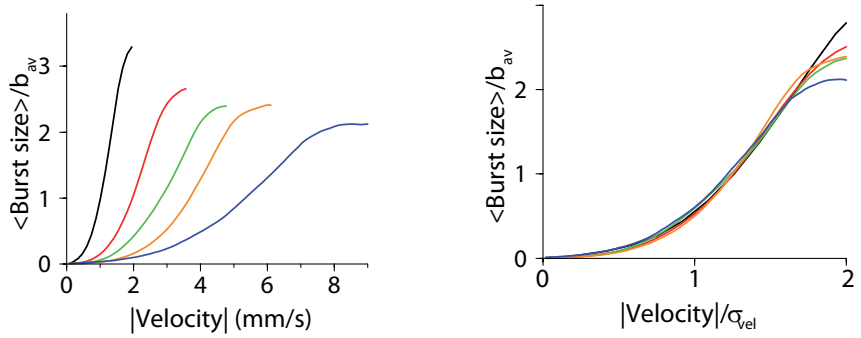

(a) Average burst-size per velocity.

(b) Average burst-size per σ_{vel}-scaled velocity.

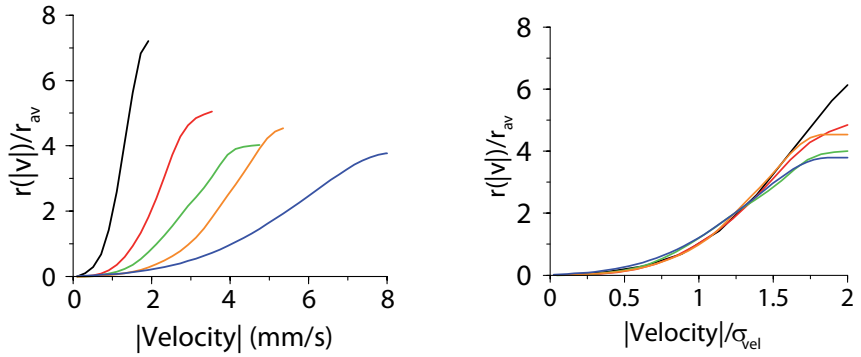

(c) Burst-rate per velocity.

(d) Burst rate per σ_{vel}-scaled velocity.

Figure 4.23: **Burst rate and burst-size coding also adapts to σ_{vel}.** **a**. Average burst-size as a function of stimulus velocity, normalized by the mean burst-size value at each stimulus σ_{vel}. **b**. Average burst-size as a function of the stimulus velocity rescaled by σ_{vel}. **c**. Normalized (by mean burst rate) burst rate as a function of the stimulus velocity. **e**. Burst rate as a function of the stimulus velocity rescaled by σ_{vel}. (Same stimulus ensembles as in Figure 4.19).

4.2.4 Adaptive scaling of principal components

Velocity is the most relevant variable that is coded, but as shown in section 4.1.3 is not the only one, and so we also tested whether there was adaptive scaling for other relevant stimulus features. To do this, we calculated the neural gain as a function of the two main stimulus components obtained by PCA (see section 3.4.7). We demonstrated in section 4.1.3 that these two components corresponded to stimulus velocity and acceleration (illustrated in insets of Figures 4.24b and4.24d). Both components showed a similar adaptation to stimulus variance, as we can see in Figure 4.24.

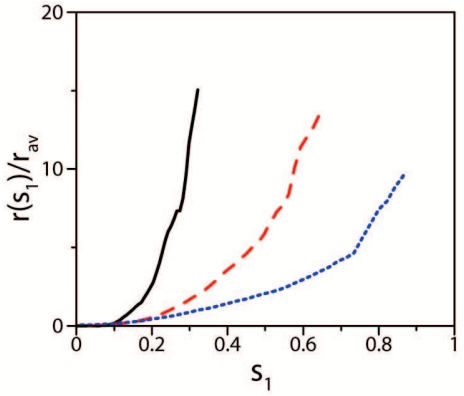

(a) Normalized rate as a function of the 1st component.

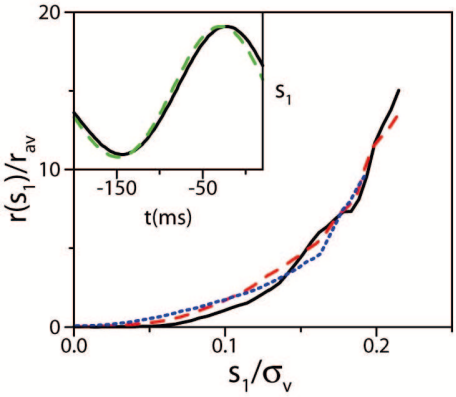

(b) Normalized rate as a function of the 1st component/σ_{vel}.

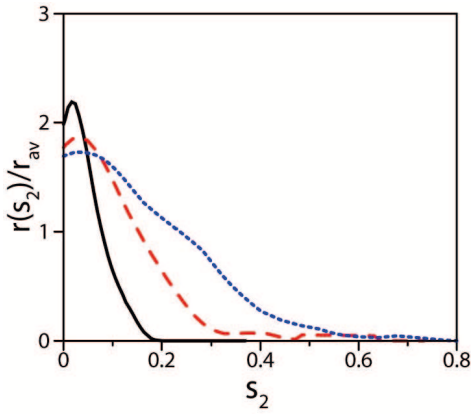

(c) Normalized rate as a function of the 2nd component.

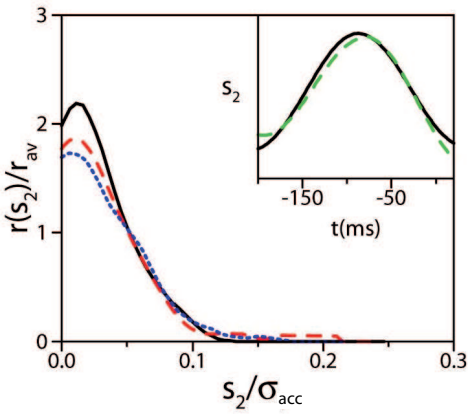

(d) Normalized rate as a function of the 2nd component/σ_{acc}.

Figure 4.24: **First two principal components obtained by PCA show adaptive scaling**. **a**. Normalized rate as a function of the dominant eigenvector (velocity) for a stimulus of frequency cut-off 5 Hz, and three standard deviations: $\sigma_{\mathbf{vel}} = 1.5$ (black solid line), 3 (red dashed line), 4.5 mm/s (blue dotted line). **b**. Same as a, but for velocity rescaled by the corresponding standard deviations. Inset: Black solid line: first eigenvector s1. Green dashed line: Burst triggered average of the stimulus velocity, roughly corresponding to the mean velocity before bursts. **c**. Normalized rate as a function of the second leading eigenvector (acceleration) for the same stimulus parameters as in a. **d**. Same as c, but with acceleration rescaled by the corresponding distribution widths. Inset: Black solid line: second eigenvector s2. Green dashed line: Derivative of the first component, showing that the second eigenvector gives the acceleration.

4.3 The role of sodium pumps in the adaptive scaling

Activity-dependent hyperpolarization has been shown to produce a reduction in excitability in the T cell membrane. In this cell, hyperpolarization is due to the action of two membrane components: sodium pumps and calcium-dependent potassium channels. Sodium pumps are known to be responsible of the 75% of the activity-dependent hyperpolarization (Baylor and Nicholls, 1969a; Van Essen, 1973) while calcium-dependent potassium channels produce the residual 25% (Jansen and Nicholls, 1973). In order to describe the biophysical substrates of the T cell adaptation to statistics, we investigated the possible implication of both molecular species.

4.3.1 Adaptive effect of sodium pumps activity

The action of sodium pumps produces a hyperpolarization of the T cell membrane that reduces the excitability of the cell (Van Essen (1973)). These changes in excitability could account for the adaptive scaling found in T cell response. Therefore, we investigated the role of sodium pumps in this process.

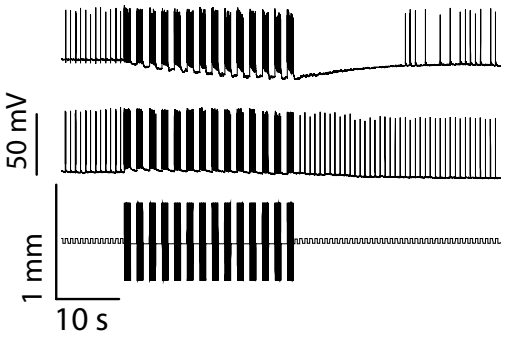

Figure 4.25: **Elimination of hyperpolarization by the action of strophantidin**. *Top*: T cell voltage response to a mechanical protocol to test reduction of excitability (*bottom*). *Middle*: Voltage response of the same T cell as in *top* after adding strophantidin to the bath solution.. *Bottom*: Protocol consisting of a 10 s train of 40 mm mechanical steps at 1.5 Hz on the skin of the leech, followed by 20 s of several 400 mm-amplitude sine-wave patterns at 10 Hz, and then repeating the initial train.

We first examined the effect of the sodium pump on the activity-dependent hyperpolarization and on the reduction of excitability using a simple protocol for skin stimulation. Skin was subjected to a series of small (40 mm) mechanical steps at a frequency of 1.5 Hz both before and after 20 s of skin displacement that consisted of 400 mm amplitude sinusoidal patterns at 10 Hz (Figure 4.25, *bottom*). In control conditions,

the membrane hyperpolarized by 10 mV during the sinusoidal stimulation and did not respond to the following step stimuli for 20 s (Figure 4.25, *top*). When we bathed the preparation with strophantidin (Figure 4.25, *middle*), a well-known blocker of the sodium pump (Jansen and Nicholls, 1973; Van Essen, 1973), the hyperpolarization disappeared and the cell responded almost immediately to the following step stimuli. We conclude that the hyperpolarization that is induced by the pump activity after firing increases the voltage-to-spike threshold.

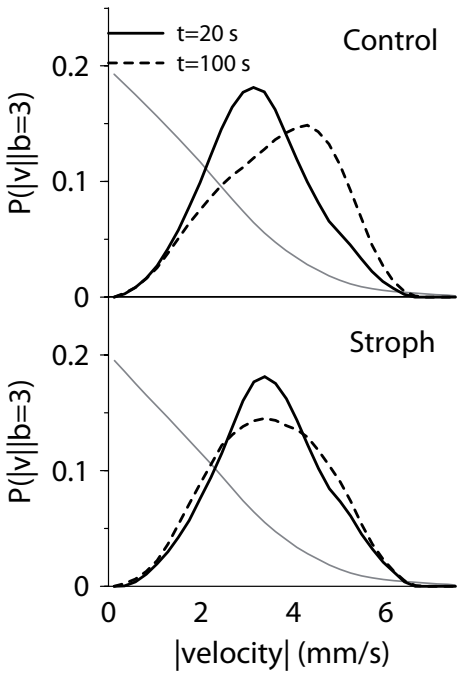

Figure 4.26: **Blocking sodium pumps eliminates the dynamics necessary for adaptive rescaling**. *Top*: Velocity distribution before bursts of three spikes for a stimulus ensemble with $\sigma_{\mathbf{vel}}$ = 2.25 mm/s and a frequency cut-off of 5 Hz until t = 20 s (solid line) and until t = 100 s (dashed line). *Bottom*: Same as in *top* but in the presence of the sodium pump blocker strophantidin 0.15 mM, showing no shift to higher velocities..

We then examined the effect of the sodium pumps on adaptation. Adaptation to statistics implies that a burst of given size is first produced in response to low velocities, but after 1 min of stimulation it is produced in response to higher velocities. As we showed in section 4.2.2, the T cell response is adapted after 1 min of stimulation (Figure 4.17c). This implies that there is a shift of the response to higher velocities, higher the larger the stimulus variance. For a burst of three spikes, for example, the distribution of preceding velocities showed this shift to higher velocities. In Figure 4.26 *top* we

can see how in normal conditions the response in the first 100 seconds is shifted when compared to the response to the first 20 seconds . After sodium pumps were blocked with strophantidin (Jansen and Nicholls, 1973), there was at most 6–9 min of healthy firing response (see section 3.3), enough time to observe neither hyperpolarization nor a shift to higher velocities. Figure 4.26 shows how the strophantidin eliminates the shifting to higher velocities.

Notably, there was a substantial disruption of adaptive scaling in the presence of the sodium-pump blocker strophantidin, shown for $\sigma_{\mathbf{vel}}$ of 1.5 (black) and 2.25 mm/s (red) (Figure 4.27). This is indicated by the fact that velocity distributions or input/output relationships scale much better in control condition (Figures 4.27a-e *top*) than in strophantidin condition (Figures 4.27a-e *middle*). As a measure of disruption of adaptive scaling, we used the difference in the mean value of the two ensembles, d (for velocity distributions) and he root-mean-square error, RMSE, between the two curves (for input/output relations). This disruption of adaptive scaling was significant for all quantities implicated in the coding, including the distribution of velocities before bursts of two spikes (Figure 4.27a, p = 0.03), bursts of three or more spikes (Figure 4.27b, p = 0.045) and all bursts (Figure 4.27c, p = 0.011), as well as the burst rate (Figure 4.27d, p = 0.012) and burst-size input/output relationships (Figure 4.27e, p = 0.012). P values were obtained from pair-wise t-tests after checking that the data of the differences between controls and strophantidin conditions were normally distributed (Lilliefors and Jarque-Bera tests).

We tested that this disruption of adaptive scaling by strophantidin was not a result of additional non-stationary effects of the drug by checking that the input-output relationships were independent of the order of presentation of the stimulus distributions. In Figure 4.28a we can see the adaptive scaling in control condition in the T cell response to Gaussian white noise of cut-off frequency of 5 Hz and two different σ_{vel} (1.5 and 2.25 mm/s). Figure 4.28b shows that the presentation order does not underlie the disruption of the adaptive scaling. In this case we first presented the stimulus with a $\sigma_{\mathrm{vel}} = 2.25$ mm/s (red), then the one with $\sigma_{\mathrm{vel}} = 1.5$ mm/s (black) and then again the one with $\sigma_{\mathrm{vel}} = 2.25$ mm/s (dashed red). Neither the first nor the second normalized burst rate input/output relation for $\sigma_{\mathrm{vel}} = 2.25$ mm/s showed adaptive scaling with the one of $\sigma_{\mathrm{vel}} = 1.5$ mm/s.

With all these results, we concluded that the sodium pump is necessary for adaptation to statistics on a slow time scale in the mechanoreceptor neuron.

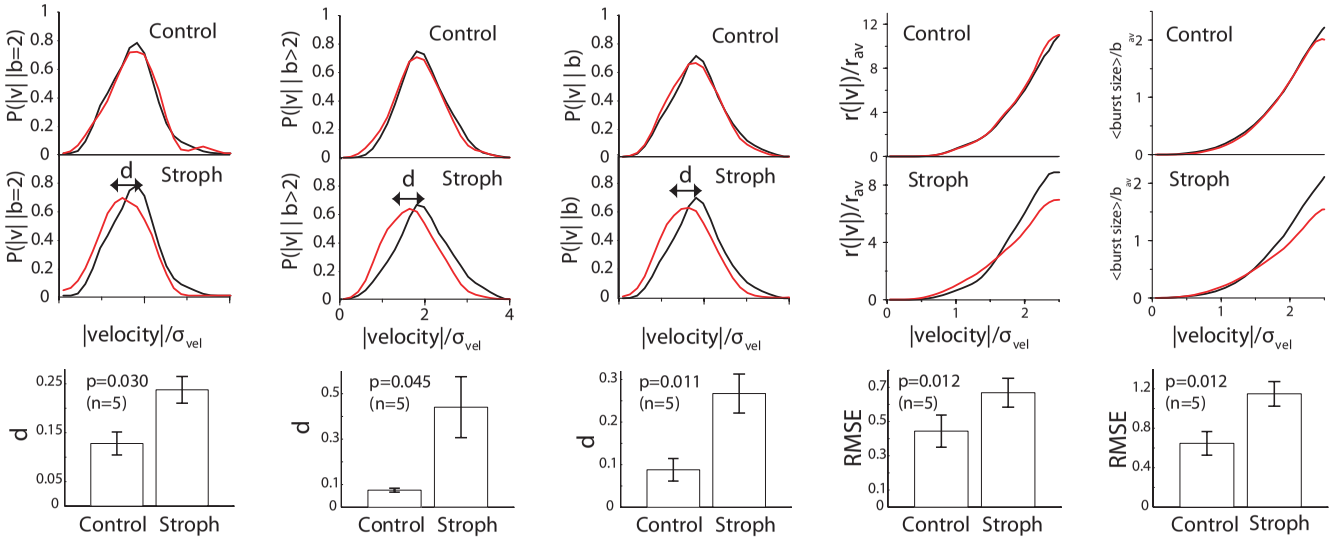

(a) P(|v| |b=2) (b) P(|v| |b>2) (c) P(|v| |b) (d) Burst rate/v. (e) Burst-size/v.

Figure 4.27: **Blocking sodium pumps disrupts adaptive scaling**. **a**. σ_{vel}-scaled velocities distributions before bursts of 2 spikes for two stimulus ensembles (cut-off frequency of 5 Hz and σ_{vel} of 1.5, black, and 2.25 mm/s, red). *Top*: control condition. *Middle*: strophantidin condition. *Bottom*: Significance tests for adaptive scaling. **b**. Velocity distributions as in a, but for bursts of 3 or more spikes. **c**. Velocity distributions as in a, but for all bursts. **d**. σ_{vel}-scaled normalized burst rates as in a. **e**. σ_{vel}-scaled normalized mean burst-size as in a. Error bars are s.e.m.

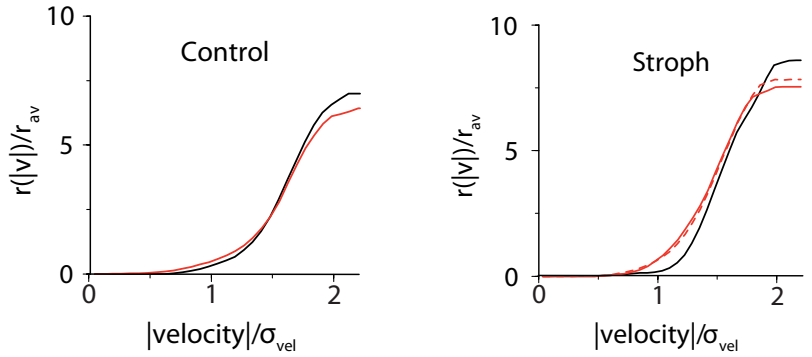

(a) Control condition (b) Strophantidin condition

Figure 4.28: **No non-stationarity affecting the input-output relationships in presence of strophantidin**. **a**. Normalized burst rate as a function of velocity divided by $\sigma_{\text{vel}} = 1.5$ mm/s (black line) and $\sigma_{\text{vel}} = 2.25$ mm/s (red line) and a frequency cut-off of 5 Hz. **b**. In presence of strophantidin, we used a stimulation protocol first using an ensemble with $\sigma_{\text{vel}} = 2.25$ mm/s (solid red line), then $\sigma_{\text{vel}} = 1.5$ mm/s (black line) and again $\sigma_{\text{vel}} = 2.25$ mm/s (dashed red line).

4.3.2 Non adaptive effect of calcium-dependent potassium conductance

Activity-induced hyperpolarization in T cell is mainly due to the sodium pump, but to a lesser extent is also the result of a calcium-dependent potassium conductance with a contribution up to 5 mV (Jansen and Nicholls, 1973). We therefore tested whether this potassium conductance has an influence on adaptive scaling using the specific blocker apamin, which is known to inhibit the calcium-dependent potassium conductance in the T cell (Mozzachiodi et al., 2001, see section 3.3).

We first tested that adding 1 nM of apamin decreased hyperpolarization values after stimulation protocols designed to see this effect (Figure 4.29a). We confirmed a significant decrease of hyperpolarization of 5 mV for these protocols ($P < 0.002$, Figure 4.29b). We also tested that in our experiments using Gaussian white noise, apamin had the same effect, and we found that hyperpolarization after bursts was reduced by 4-6 mV (Figures 4.29c and 4.29d).

Then, we performed the same test as we had previously performed to show that blocking sodium pumps had a significant disruptive effect on adaptive scaling (Figures 4.26and 4.27). We found that the shift of coded velocities in control conditions (Figure 4.30a *top*) is similar to that of apamin conditions (Figure 4.30a *bottom*). We also found that the relevant coding variables, like normalized rates, show the same adaptive scaling as controls (Figure 4.30b).

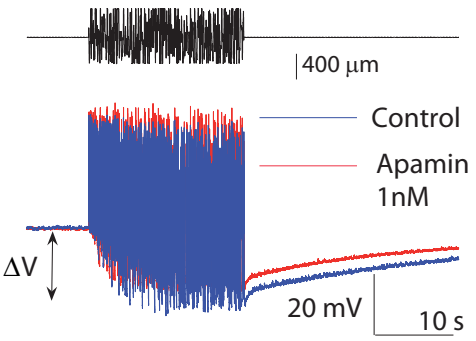

(a) Voltage response with Apamin and in control.

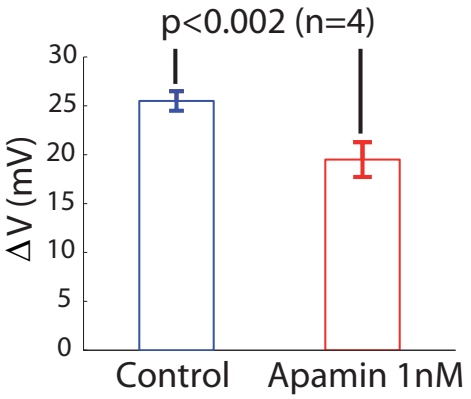

(b) Significant reduction of hyperpolarization.

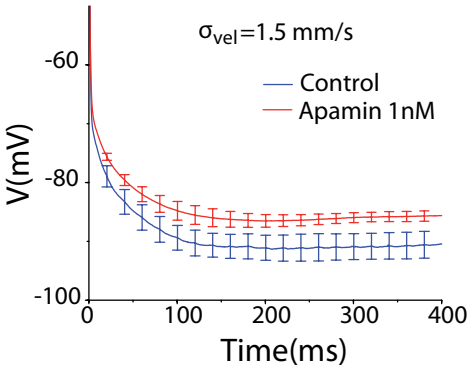

(c) Average voltage trace with and without apamin ($\sigma_{\mathbf{vel}} = 1.5$ mm/s).

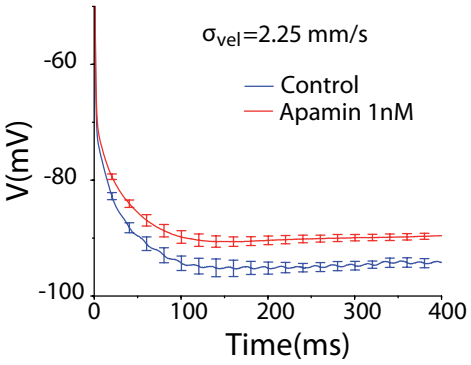

(d) Average voltage trace with and without apamin ($\sigma_{\mathbf{vel}} = 2.25$ mm/s).

Figure 4.29: **1 nM of apamin decreases afterhyperpolarization in T cell**. **a**. Voltage response in control (in blue) and in presence of apamin 1nM (in red) to stimulation protocols designed to produce hyperpolarization (in black; section 3.3). **b**. Comparison of hyperpolarization in 4 different T cells with and without Apamin. Controls hyperpolarize 5 mV more (pair-wise t-test, $P < 0.002$ and $n = 4$). Error bars are s.e.m. **c**. Average voltage trace after bursts in response to a Gaussian white noise with cut-off frequency of 5 Hz and $\sigma_{\mathbf{vel}} = 1.5$ mm/s for 4 control experiments (in blue) and 4 experiments in presence of apamin for the same neurons (in red). **d**. Same as c but for stimulation with $\sigma_{\mathbf{vel}} = 2.25$ mm/s . Error bars in c and d are standard deviations.

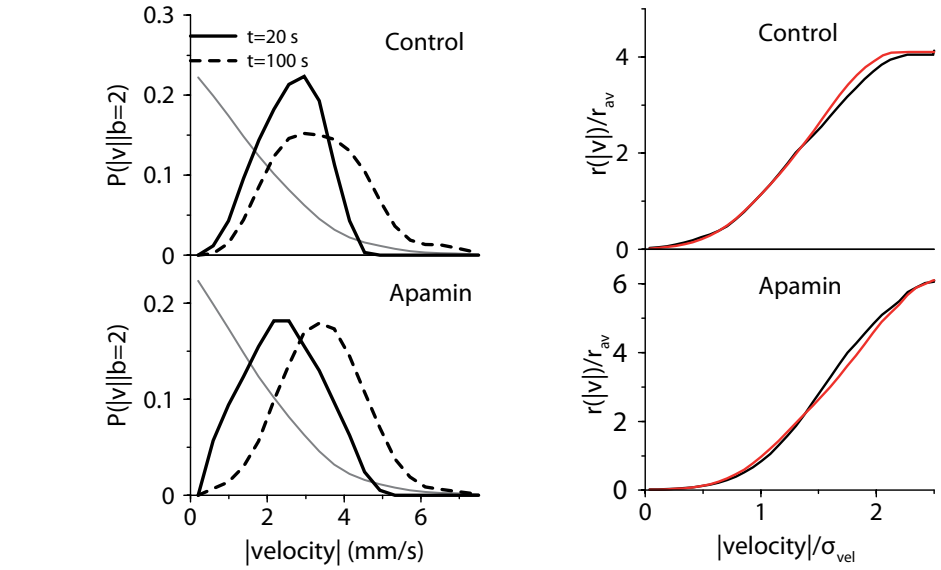

(a) Velocity distributions given b = 2.

(b) Normalized rate.

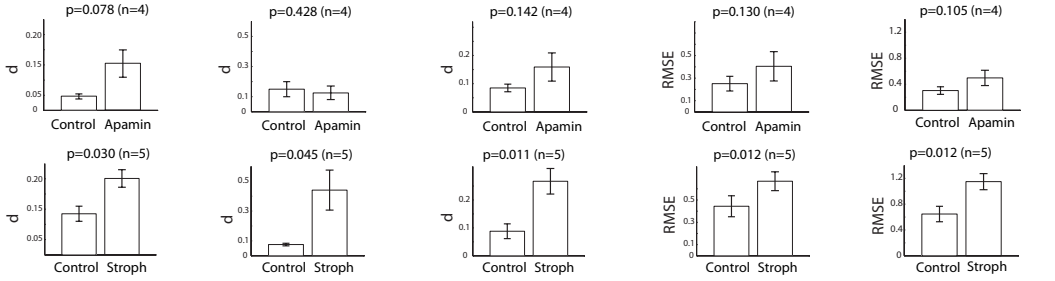

(c) Difference in P(|v| |b=2)

(d) Difference in P(|v| |b>2)

(e) Difference in P(|v| |b)

(f) Difference in burst rate/v.

(g) Difference in burst-size/v.

Figure 4.30: **Blocking calcium-dependent potassium current has no significant effect in adaptive scaling**. **a**. *Top*: Velocity distributions before bursts of 2 spikes for the first 20 s of recording (thick black line) and the first 100 s (dashed line) in a control recording. Stimulus ensemble with cut-off frequency 5 Hz and $\sigma_{\mathbf{vel}} = 2.25$ mm/s shown as thin continuous line. *Bottom*: Same as *top* but with 1 nM of apamin. **b**. *Top*: Normalized burst rate showing adaptive scaling for two ensembles of standard deviations $\sigma_{\mathbf{vel}} = 1.5$ (black) and 2.25 mm/s (red) and cut-off frequency of 5 Hz in control experiment. *Bottom*: As *top* but with 1 nM of apamin. **c-g**. Significance tests for adaptive scaling, comparing controls and apamin condition (*top*) and those for controls and strophantidin condition (*bottom*, as in Figure 4.27). Scale of y-axis has been chosen identical for apamin and strophantidin conditions for quick comparison. No significant difference is found between controls and apamin condition for the five quantities measured. Error bars are s.e.m.

We finally tested that none of the relevant coding properties had significant differences to controls, finding no sign of a significant disruption of adaptive scaling (Figures 4.30c-f). Only for the case of the velocity distributions prior to bursts of 2 spikes, there is an effect close to be significantly different from controls (Figure 4.30c, p = 0.078). Figure 4.30c-f gives also the results for strophantidin for comparison (bottom, same as Figure 4.27), showing that for the apamin condition the results are also more similar to controls in the mean values and in no case the small differences are statistically significant.

4.3.3 Neuronal model

To further investigate the role of sodium pumps in adaptive scaling, we used a two-compartment model. The model, described in section 3.5, includes all known conductances for the T neuron (Cataldo et al., 2005). The responses of the model neuron to simple protocols that hyperpolarize the membrane (in section 3.3.1) were similar to those observed in experiments (Figure 4.31; compare with experimental results in Figure 4.25). After a high frequency stimulation, the membrane potential of the neuron model gets hyperpolarized, reducing its excitability (Figure 4.31a). When the sodium pump is removed from the model, this hyperpolarization does not take place, and consequently there is not a reduction in excitability (Figure 4.31b). Removing the sodium pump currents is similar to the adding strophantidin in real experiments. The small gap that we observed in absence of sodium pump currents (Figure 4.31b) is a result of the recovery time of the after-hyperpolarization calcium-dependent potassium conductance, $g_{\mathrm{K,Ca}}$, which has a faster time scale than that of the sodium pump (Cataldo et al., 2005; Jansen and Nicholls, 1973). This gap also takes place in the real T cell (in Figure 4.25 *middle*, the first mechanical step does not elicit response).

4.3.3.1 Effect of the sodium pumps in the neuronal model

To simulate the mechanical stimulation of T cells, we stimulated the neuronal model with Gaussian white noise current stimuli of different σ_{vel}, with units in nA/s. These current stimuli have the disadvantage of skipping the transduction of the mechanical stimuli. However we found a similar response in the natural and in the modeled cell.

Analyzing the simulated responses to Gaussian white noise current stimuli of different σ_{vel}, we determined that the sodium pump has effects in both coding and adaptive scaling. As we can see in Figure 4.32a (*top*: with sodium pump, *bottom*: without sodium pump), without the sodium pump, the neuron saturated earlier and thus did not code high velocities. Adaptive scaling took place in the complete model for velocities up to

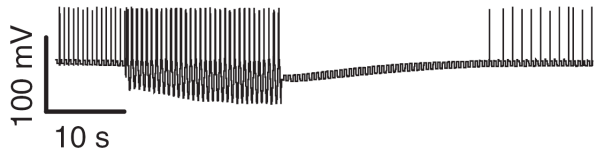

(a) Simulated response to a protocol hyperpolarizing the membrane.

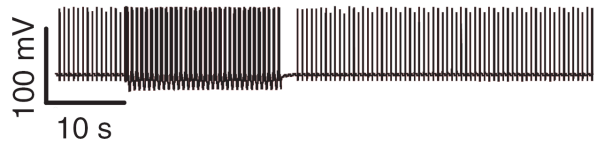

(b) Simulated response to a protocol hyperpolarizing the membrane without sodium pumps.

Figure 4.31: **Simulated response of the neuronal model is similar to real T cell response**. **a**. Neuron model response to a square wave stimulation (current step amplitude of 8 nA, period of 1.2 s) triggering 1 spike per period, followed by a sine wave with an amplitude of 40 nA and a frequency of 2 Hz producing higher activity. **b**. Response of the neuron model to the same stimulation without the sodium pump.

twice the σ_{vel} of the stimulus (Figure 4.32b *top*), which is similar to the experimental results (Figure 4.23d). The same model without sodium-pump dynamics showed no adaptive scaling in the normalized rate (Figure 4.32b *bottom*), which is also similar to the experimental results in presence of strophantidin (Figure 4.27d).

As we did for real experiments, we tested in the model neuron whether the adaptation to the statistics of the burst-size coding was disrupted without the action of the sodium pump. Checking the distributions of stimulus velocities before bursts of two spikes in response to Gaussian white noise stimuli of different σ_{vel}, we also determined that there was no adaptive scaling in absence of sodium pumps (Figure 4.33). In the complete model, different velocity distributions given bursts of two spikes matched when scaled by σ_{vel} (Figure 4.33b *top*). When the sodium pump is removed, the velocity distributions do not match so well (Figure 4.33b, *bottom*).

To find out whether the sodium pumps could be the only elements responsible for adaptive scaling in the model, we also tested the effects of eliminating the calcium-dependent potassium current, $I_{\text{K,Ca}}$. We removed this current from the model but retaining the sodium pump, as we did in real experiments by the use of apamin. The $I_{\text{K,Ca}}$ is the other hyperpolarizing conductance of the T cell that can be responsible for 25% of the

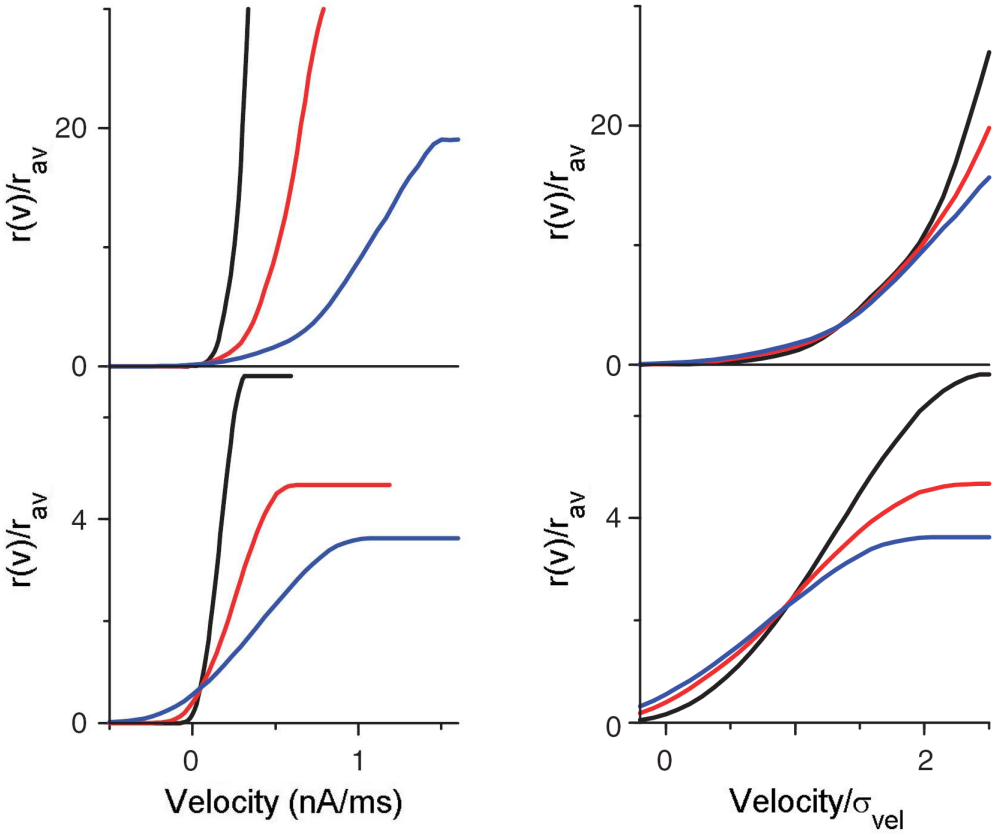

(a) Burst rate coding for velocity values.

(b) Adaptation of burst rate coding to σ_{vel}.

Figure 4.32: **Sodium pumps affect coding and adaptive scaling in the model**. **a**. *Top*: Normalized burst rate for the model neuron in response to Gaussian white-noise current stimulation ensembles of different σ_{vel} (black: 4.5 nA/s; red: 9 nA/s; blue: 18 nA/s; cut-off frequency = 8 Hz). *Bottom*: Normalized burst rate as in *top* figure, but without the sodium pump. **b**. Normalized burst rates in *top* (complete model) and *bottom* (without the sodium pump) with the stimulus velocity rescaled by the σ_{vel}.

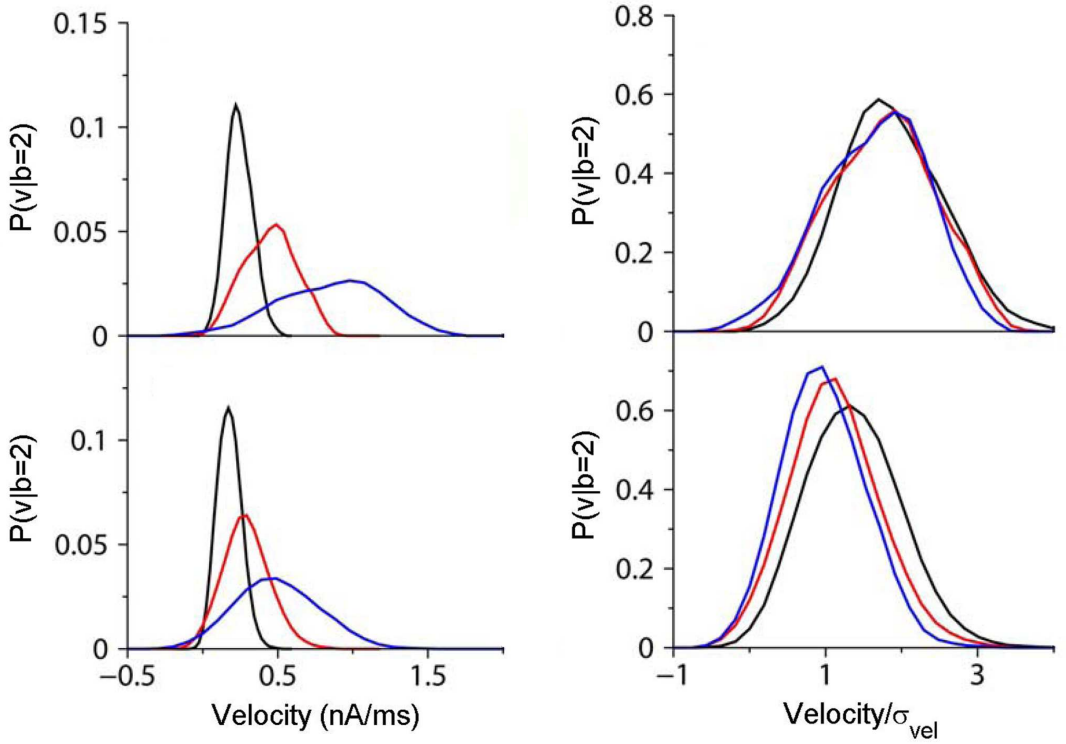

(a) Burst-size coding for velocity values.

(b) Adaptation of burst-size coding to σ_{vel}.

Figure 4.33: **Adaptive burst coding also needs the action of sodium pumps in the model**. **a**. *Top*: Velocity distribution given bursts of 2 spikes for the model neuron in response to Gaussian white-noise current stimulation ensembles of different σ_{vel} (black: 4.5 nA/s; red: 9 nA/s; blue: 18nA/s; cut-off frequency = 8 Hz). *Bottom*: Velocity distribution given bursts of 2 spikes as in *top* figure, but without the sodium pump. **b**. Velocity distribution given bursts of 2 spikes in *top* (complete model) and *bottom* (without the sodium pump) with the stimulus velocity rescaled by the σ_{vel}.

hyperpolarization in the early response to stimulation. The recuperation for this hyperpolarization takes place in 1 or 2 seconds. This time should not be enough for the neuron to "estimate" the standard deviation of the stimulus distribution at the frequencies considered since there is no time to collect enough statistics. We showed within the model that this current is not related to the adaptive scaling seen in the input/output relations, but rather to burst duration and frequency adaptation inside bursts, as it has been demonstrated in other models of neurons (Wang, 1998) . We plotted the normalized burst rate in response to Gaussian white noise stimuli of different σ_{vel} for the complete model (Figure 4.34a *top*) and for the model without the $I_{\mathrm{K,Ca}}$ current but retaining the sodium pump (Figure 4.34a *bottom*). We can see in Figure 4.34b that normalized rates versus velocity and the same plots scaling stimulus velocity by σ_{vel} are almost identical for the complete model and the model without the $I_{\mathrm{K,Ca}}$ current. This Figure shows that the removal of $I_{\mathrm{K,Ca}}$ did not eliminate the adaptive scaling, again consistent with the experimental results (Figure 4.30). This result is in clear contrast to the behavior in Figure 4.32 for the sodium pump, allowing us to argue that, at least in the model, sodium pumps are necessary and sufficient for the adaptive scaling.

4.3.3.2 Generality of the effect of sodium pumps

We also used the model to test the generality of the effect of the hyperpolarization due to sodium pumps. It is well known that neuronal firing depends on neuron size experimentally and in model studies (Van der Heyden et al., 1994). In our case, the model offers the opportunity to test which types of neurons might best show the hyperpolarization due to sodium pump activity. In particular we calculated, within the model and under plausible conditions, the dependence of hyperpolarization on neuron size.

We tested three cases: Case A assumes that area only affects the absolute values of capacitance and conductances; case B studies the effect of surface on sodium dynamics; case C takes into account both cases A and B simultaneously.

Case A: *Area affecting only absolute values of capacitance and conductances.*
In this case we kept the same specific values for membrane capacitance and conductances (values per unit area), and change only the membrane area. Making explicit the dependence of the voltage equations on compartment areas, we have

$$-CA_{\mathrm{S}}\frac{dV_{\mathrm{S}}}{dt} = A_{\mathrm{s}}(I_{\mathrm{L}}^{\mathrm{S}} + I_{\mathrm{Na}}^{\mathrm{S}} + I_{\mathrm{K}}^{\mathrm{S}} + I_{\mathrm{Ca}}^{\mathrm{S}} + I_{\mathrm{K,Ca}}^{\mathrm{S}} + I_{\mathrm{pump}}^{\mathrm{S}}) + \frac{1}{R_C}(V_{\mathrm{S}} - V_{\mathrm{D}}) \qquad (4.1)$$

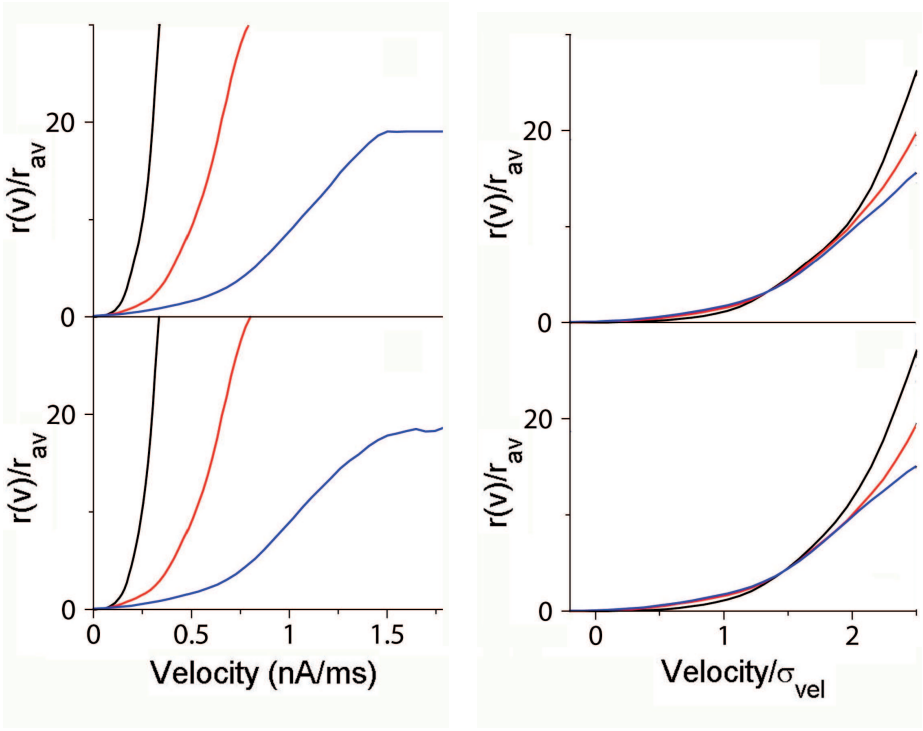

(a) Burst rate coding for velocity values. (b) Adaptation of burst rate coding to σ_{vel}.

Figure 4.34: **Removal of calcium-dependent potassium current does not eliminate adaptive scaling in the model**. **a**. *Top*: Normalized burst rate for the model neuron in response to Gaussian white-noise current stimulation ensembles of different σ_{vel} (black: 4.5 nA; red: 9 nA; blue: 18; cut-off frequency = 8 Hz). *Bottom*: Normalized burst rate as in *top* figure, but without the calcium-dependent potassium current.. **b**. Normalized burst rates in *top* (complete model) and *bottom* (without the calcium-dependent potassium current) with the stimulus velocity rescaled by the σ_{vel}.

and

$$-CA_{\mathrm{D}}\frac{dV_{\mathrm{D}}}{dt} = A_{\mathrm{D}}(I_{\mathrm{L}}^{\mathrm{D}} + I_{\mathrm{Na}}^{\mathrm{D}} + I_{\mathrm{K}}^{\mathrm{D}} + I_{\mathrm{Ca}}^{D} + I_{\mathrm{K,Ca}}^{\mathrm{D}} + I_{\mathrm{pump}}^{\mathrm{D}}) + \frac{1}{R_C}(V_{\mathrm{D}} - V_{\mathrm{S}}) - I_{\mathrm{ext}}, \quad (4.2)$$

with A_S and A_D the soma and dendritic areas, respectively, and $\frac{1}{R_C}$ the axial resistance. Capacitance C and intrinsic conductances are in units per area, as explain in section 3.5.1. To relate these equations to equations 3.2 and 3.3 in that section, we can divide both members of each of the equations above by the corresponding somatic and dendritic area, respectively. In this way we obtain exactly equations 3.2 and 3.3 with $I_{\mathrm{stim}} = I_{\mathrm{ext}}/A_{\mathrm{D}}$ and $g_{\mathrm{C}} = 1/(R_{\mathrm{C}}A_{\mathrm{D}})$ with $p = A_{\mathrm{S}}/(A_{\mathrm{S}} + A_{\mathrm{D}})$. To consider a different area in the equations 4.1 and 4.2, we can simply multiply the areas by a surface factor S. This amounts to rescaling stimulus current and electrotonic coupling, I_{stim}/S and g_{C}/S, in equations 3.2 and 3.3.

Using a sinusoidal stimulus paradigm of amplitude 40 nA and frequency 2 Hz, we calculated the afterhyperpolarization $\Delta V = |V_{\mathrm{hyp}} - V_{\mathrm{rest}}|$ and recovery time to half the hyperpolarization value, $\tau_{\mathrm{rec}}^{1/2}$, as a function of the surface scale factor S varying linearly between 0.2 and 3. As shown in Figures 4.35a (*top*) and 4.35b (*top*) larger size implies smaller hyperpolarization and shorter half recovery time.

Case B: *Area affecting sodium dynamics.*

Here we supposed that the removal of Na^+ ions is a process physically located at the membrane and increases with surface area (which amounts to scale the time constant in each compartment as τ_{Na}/S). One could also hypothesize a slower decrease of sodium concentration with size due to diffusion effects, but previous modeling studies and experimental observations in other systems support the first assumption (Van der Heyden et al., 1994). Moreover, the contribution of the fast sodium current to sodium influx (α_{Na}) has been shown to be inversely proportional to the volume beneath the membrane (Keener and Sneyd, 1998; Yamada et al., 1989). Therefore the gain term in the equation for the sodium dynamics (see section 3.5.1) is proportional to the surface-to-volume ratio. For a cylindrical compartment this factor scales inversely with the compartment radius r, and thus we varied the surface factors S and r to scale the sodium dynamics (S from 0.2 to 3 and r from 0.5 to 1.5). We obtain a slower (linear) decrease in hyperpolarization with neuron size and a power-law decrease in recovery time (middle of Figures 4.35a and 4.35b).

Case C: *Cases A and B together.*
Combining both contributions in cases A and B when changing compartmental areas, that of absolute conductances and sodium dynamics, we found that hyperpolarization may be stronger for smaller neurons (bottom of Figures 4.35a and 4.35b).

With all these evidences in the neuronal model, we concluded that the effect of sodium pump hyperpolarization may increase in smaller neurons.

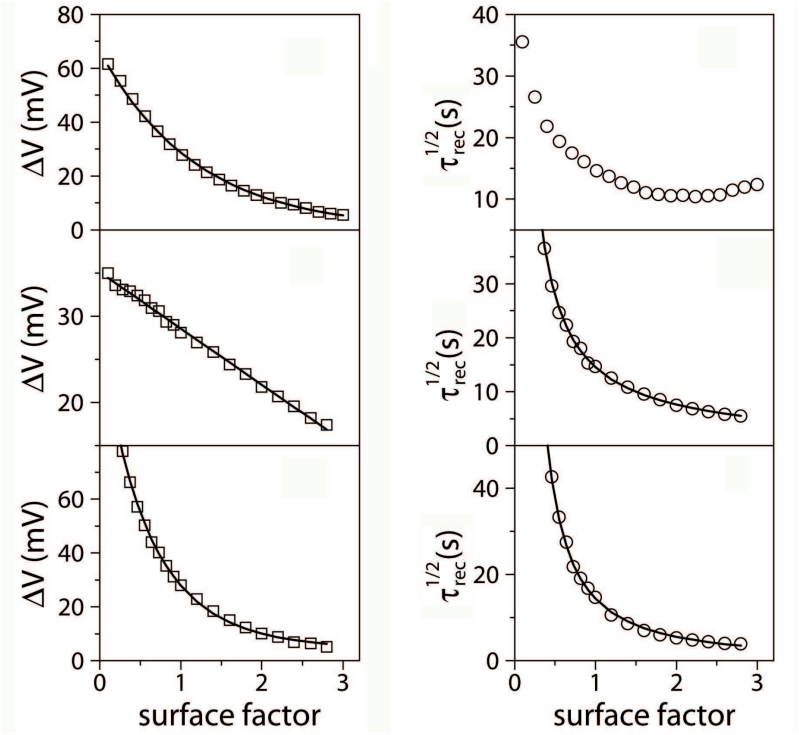

(a) Effect of size on ΔV

(b) Effect of size on $\tau_{\text{rec}}^{1/2}$

Figure 4.35: **Hyperpolarization and half-recovery time increase with decreasing neuron size according to the model**. **a**. Hyperpolarization amplitude, ΔV, as a function of surface scaling factor when scaling only the absolute values of capacitance and conductances (*Top*), when scaling only the sodium dynamics (*Middle*) and when scaling simultaneously the absolute values of capacitance and conductances and the sodium dynamics (*Bottom*). **b**. Same as in a. but for half-recovery time, $\tau_{\text{rec}}^{1/2}$. Solid lines correspond fittings: $\Delta V = 4.2e^{-0.84S}$ (a, *top*), $\Delta V = 35 - 65S$ (a, *middle*), $\Delta V = 95e^{-1.6S} + 8.6S^{-1/2}$ (a, *bottom*), $\tau_{\text{rec}}^{1/2} = 2.7S^{-0.93}$ (b, *middle*), $\tau_{\text{rec}}^{1/2} = 2.7S^{-1.37}$ (b, *bottom*).

5 Discussion

In the present thesis, we have described a neuronal code based on burst sizes (number of spikes per burst). We first dissected the coding properties of a bursting neuron, the mechanoreceptor of the leech *Hirudo medicinalis* known as T cell, and showed that the neuron uses a burst code. Bursting has been found to be important in information transmission, as it improves synaptic reliability (Lisman, 1997), the signal-to-noise ratio of neuronal responses (Livingstone et al., 1996) and the detection of behaviorally important features of the stimuli (Gabbiani et al., 1996). It is possible that bursts could act as unitary events or, alternatively, that their structures might convey extra information. Consistent with the second theory, it has been proposed that burst parameters are responsible for coding. Spike frequency during bursts might determine which postsynaptic neurons become excited (Izhikevich et al., 2003). Also, modeling studies of a general class of bursting neurons have shown that burst-size codes for stimulus slope (Kepecs et al., 2002). Experimental evidence that duration correlates with stimulus optimality in visual cortex (DeBusk et al., 1997) supports such a burst-size code.

This is to our knowledge the first time that a neuronal code based on different burst sizes (number of spike per burst) has been experimentally described. Before this work, theoretical studies (Kepecs et al., 2002) pointed at the burst size as a possible burst feature to code for stimulus slopes. Experimental results (Cattaneo et al., 1981; DeBusk

et al., 1997; Martinez-Conde et al., 2002) also suggested that the burst size could be coding for optimality in the stimulus. After our work, Eyherabide et al. (2008) found another burst size code in the auditory system of the grasshopper.

We have also shown that this neuronal code presents adaptive scaling. This finding further supports the relevance of burst size coding, as it has the flexibility that is needed for dealing with the changing real-world stimuli. In this manner the system can detect the velocity of approaching objects, with adaptive scaling allowing for the detection of high velocities relative to common stimuli such as water displacements. The most robust result for adaptive scaling is the one that we obtained when analyzing the velocity distributions prior to burst sizes. Both, the normalized burst rate and the normalized burst size coding also showed adaptive scaling. However the normalization was needed because the mean burst size and rate also depended on the variance of stimulus velocities. This fact suggests that non normalized burst rates and sizes could be elements of the neuronal code carrying information about the velocity scale. This could avoid ambiguities in the neuronal code. Maybe the burst size could be coding the relative importance of the velocity values withing the total stimulus distribution, while the non normalized burst rate could be signaling the global stimulus variance.

We further found that blocking sodium pumps had a strong and significant disruptive effect on adaptive scaling. This result points to the sodium pumps as important elements for the adaptive scaling in the leech mechanoreceptor. Sodium pumps activity is a homeostatic mechanism maintaining ionic gradients. However, it has been shown that sodium pump activity may induce hyperpolarization in neuronal membranes (Shen and Johnson, 1998; Darbon et al., 2003; Gustafsson and Wigström, 1983; Vaillend et al., 2002; Kobayashi et al., 1997; French, 1989; Kiernan et al., 2004) . Our results go a step further and implicate this ubiquitous mechanism in the adaptation of neuronal codes to stimulus statistics.

We also tested whether blocking the calcium-dependent potassium current had an effect on adaptive scaling. However no single statistical test showed a significant role for this current, albeit we found some evidence for it having a very weak effect on rescaling, close to statistical significance for bursts of two spikes.

We also modeled this neuron to further show that sodium pumps can be a general mechanism for adaptive scaling. We expect sodium pumps to be important for adaptive scaling in other systems when tested with similar stimulations. Favorable preparations would be those in which hyperpolarization has already been shown to be induced by sodium-pump activity (Shen and Johnson, 1998; Darbon et al., 2003; Gustafsson and Wigström, 1983; Vaillend et al., 2002; Kobayashi et al., 1997; French, 1989; Kiernan et al., 2004).

Both insect mechanoreceptors (French, 1989) and human skin receptors (Kiernan et al., 2004) are experimental systems similar to the one that we employed, and protocols very similar to ours could be directly adapted to these systems. In hippocampal pyramidal neurons there is a brief hyperpolarization of 1 s as a result of calcium-dependent potassium current and a hyperpolarization of 20 mV lasting 1 min that is due mainly to the sodium pump in normal conditions (Gustafsson and Wigström, 1983), similar to what occurs in the leech T neuron. In terms of functional relevance, this hyperpolarization in hippocampus may be seen as a way to avoid overexcitation (Vaillend et al., 2002), but more generally, it might scale neuronal responses to input statistics. When sodium-pump activity is reduced in hippocampal neurons, there is still hyperpolarization as a result of a sodium-sensitive potassium conductance (Gustafsson and Wigström, 1983). The situation seems to be reversed in visual cortex, where there is hyperpolarization as a result of activity affecting a time scale of 30 s that is mostly due to a sodium-dependent potassium current, and in which sodium pumps might be of secondary importance (Sanchez-Vives et al., 2000a).

Generally, sodium pumps and some potassium conductances may hyperpolarize the membrane on overlapping time scales in many neurons, with differences in their relative importance, as is the case in the T neuron, in hippocampus (Gustafsson and Wigström, 1983; Vaillend et al., 2002), in C-fibers in the bullfrog sciatic nerve (Kobayashi et al., 1997), insect mechanoreceptors (French, 1989) and probably in visual cortex (Sanchez-Vives et al., 2000a,b). Adaptive scaling in bipolar cells in the retina has been shown to be due to slow sodium inactivation (Rieke, 2001; Kim and Rieke, 2003). This is an effect that might be quite general on the time scale of 1 s, and that is, in principle, compatible with adaptive scaling on the scale of 1 min as a result of sodium pump activity.

Adaptive scaling could be based on more than one single-neuron mechanism. With mechanisms acting on different time scales, the neuron could adapt its response dealing with the complex dynamics of stimuli. With mechanisms acting on the same time scale, the neuron could show an adaptive response able to deal under different constraints, as, for instance, modulating its adaptive response by different molecular mechanisms.

Conclusions

In this thesis, we have shown that:

- The touch mechanoreceptor (T cell) of the leech *Hirudo medicinalis* codes by the number of spikes per burst the velocity values of an object indenting the skin of the animal, in such a way that larger bursts code for higher velocities.

- There is a reduction in membrane excitability that correlates to an increasing activity-dependent hyperpolarization with increasing stimulus variance.

- The burst size code and the burst rate of the T cell adapt to the stimulus statistic, more precisely to the stimulus variance.

- The sodium-pump dynamics, contributing for the 75% of the activity-dependent hyperpolarization, are a sufficient mechanism for a neuronal adaptation to stimulus variance on the time scale of 1 min. This has been tested both experimentally and using numerical simulations.

- The calcium-dependent potassium current, even if it contributes up a 25% to the activity-dependent hyperpolarization, has no significant effect on the adaptive scaling.

The results of this thesis have been published in Arganda et al. (2007).

Conclusiones

En esta tesis hemos demostrado que:

- El mecanoreceptor de tacto (célula T) de la sanguijuela *Hirudo medicinalis* codifica la velocidad de un objeto sobre la piel del animal a través del número de potenciales de acción por ráfaga, de tal modo que las ráfagas mayores (con mayor número de potenciales de acción) codifican velocidades mas altas.

- Hay una reducción en la excitabilidad de membrana que correlaciona con la hiperpolarización dependiente de actividad, que a su vez aumenta con mayores varianzas en las distribuciones de velocidad del estímulo.

- El código por tamaño de ráfaga y la frecuencia entre ráfagas de la célula T se adaptan a la estadística del estimulo, más específicamente a la varianza de la distribución de velocidades del estímulo.

- La dinámica de las bombas de sodio, que contribuye en un 75% a la hiperpolarización dependiente de la actividad, es un mecanismo suficiente para la adaptación a la varianza del estímulo en la escala de 1 min. Esto ha sido demostrado tanto por experimentos como por simulaciones numéricas.

- La corriente de potasio dependiente de calcio, a pesar de que contribuye hasta un 25% a la hiperpolarización dependiente de actividad, no tiene ningún efecto significativo en la adaptación a la estadística.

Los resultados de esta tesis han sido publicados en Arganda et al. (2007).

Bibliography

Abbott, L. F., Varela, J. A., Sen, K., Nelson, S. B., Jan 1997. Synaptic depression and cortical gain control. Science 275 (5297), 220–224.

Adrian, E., 1928. At the Basis of Sensation. Christopher (London).

Adrian, E. D., Zotterman, Y., Aug 1926. The impulses produced by sensory nerve endings: Part 3. impulses set up by touch and pressure. J Physiol 61 (4), 465–483.

Agüera y Arcas, B., Fairhall, A., Bialek, W., 2003. Computation in a single neuron: Hodgkin and huxley revisited. Neural Computation 15 (8), 1715–1749.
URL http://www.mitpressjournals.org/doi/abs/10.1162/08997660360675017

Alle, H., Geiger, J. R. P., 2006. Combined Analog and Action Potential Coding in Hippocampal Mossy Fibers. Science 311 (5765), 1290–1293.
URL http://www.sciencemag.org/cgi/content/abstract/311/5765/1290

Arganda, S., Guantes, R., de Polavieja, G. G., Nov 2007. Sodium pumps adapt spike bursting to stimulus statistics. Nat Neurosci 10 (11), 1467–1473.
URL http://dx.doi.org/10.1038/nn1982

Arshavsky, Y. I., Deliagina, T. G., Orlovsky, G. N., Panchin, Y. V., 1989. Control of feeding movements in the pteropod mollusc, clione limacina. Exp Brain Res 78(2), 387–397.

Barker, J. L., Gainer, H., 1975. Studies on bursting pacemaker potential activity in molluscan neurons. i. membrane properties and ionic contributions. Brain Research 84 (3), 461 – 477.
URL http://www.sciencedirect.com/science/article/B6SYR-4847Y0D-249/2/f897bb1642829fd1c04c8423dde86811

Barlow, H., Mollon, J., 1982. The Senses. Cambridge University Press.

Baylor, D., Nicholls, J., 1969a. After-effects of nerve impulses on signalling in the central nervous system of the leech. J Physiol 203 (3), 571–589.
URL http://www.pubmedcentral.nih.gov/tocrender.fcgi?iid=126503

Baylor, D. A., Nicholls, J. G., Aug 1969b. Chemical and electrical synaptic connexions between cutaneous mechanoreceptor neurones in the central nervous system of the leech. J Physiol 203 (3), 591–609.

Bhattacharjee, A., Kaczmarek, L. K., Aug 2005. For k+ channels, na+ is the new ca2+. Trends Neurosci 28 (8), 422–428.
URL http://dx.doi.org/10.1016/j.tins.2005.06.003

Bialek, W., Rieke, F., de Ruyter van Steveninck, R. R., Warland, D., June 1991. Reading a neural code. Science 252 (5014), 1854–1857.
URL http://dx.doi.org/10.1126/science.2063199

Blackshaw, S., 1981. Morphology and distribution of touch cell terminals in the skin of the leech. J Physiol 320 (1), 219–228.
URL http://jp.physoc.org/cgi/content/abstract/320/1/219

Borst, A., Theunissen, F., 1999. Information theory and neural coding. Nat Neurosci 2 (11), 947–57.

Brenner, N., Bialek, W., Steveninck, R. D. R. V., 2000. Adaptive rescaling maximizes information transmission. Neuron 26, 695–702.

Carlton, T., McVean, A., 1995. The role of touch, pressure adn nociceptive mechanoreceptors of the leech in unrestrained behaviour. J Comp Physiol A 177 (6), 781–791.

Carnevale, N. T., Wachtel, H., May 1980. Two reciprocating current components underlying slow oscillations in aplysia bursting neurons. Brain Res 203, 45–65.

Cataldo, E., Brunelli, M., Byrne, J., Av-Ron, E., Cai, Y., A., D., 2005. Computational model of touch sensory cells (t cells) of the leech: Role of the afterhyperpolarization (ahp) in activity-dependent conduction failure. J Comp Neurosci 18 (1), 5–24.
URL http://www.springerlink.com/content/u254221226348476/

Catarsi, S., Brunelli, M., 1991. Serotonin depresses the after-hyperpolarization through the inhibition of the na+/k+ electrogenic pump in t sensory neurones of the leech. J Exp Biol 155 (1), 261–273.
URL http://jeb.biologists.org/cgi/content/abstract/155/1/261

Catarsi, S., Garcia-Gil, M., Traina, G., Brunelli, M., 1990. Seasonal variation of serotonin content and nonassociative learning of swim induction in the leech hirudo medicinalis. J Comp Physiol A 167 (4), 469–474.
URL http://www.springerlink.com/content/u318w10571142515/

Cattaneo, A., Maffei, L., Morrone, C., Jul 1981. Patterns in the discharge of simple and complex visual cortical cells. Proc R Soc Lond B Biol Sci 212 (1188), 279–297.

Combes, D., Simmers, J., Moulins, M., 1997. Conditional dendritic oscillators in a lobster mechanoreceptor neurone. J Physiol 499 (Pt 1), 161–177.
URL http://jp.physoc.org/cgi/content/abstract/499/Pt_1/161

Connors, B. W., Gutnick, M. J., 1990. Intrinsic firing patterns of diverse neocortical neurons. Trends in Neurosciences 13 (3), 99 – 104.
URL http://www.sciencedirect.com/science/article/B6T0V-485RHY0-9/2/94dedd0cec0b9b04164bfe458c106a96

Darbon, P., Tscherter, A., Yvon, C., Streit, J., Nov 2003. Role of the electrogenic na/k pump in disinhibition-induced bursting in cultured spinal networks. J Neurophysiol 90 (5), 3119–3129.
URL http://dx.doi.org/10.1152/jn.00579.2003

Dayan, P., Abbott, L. F., 2001. Theoretical Neuroscience. Computational and Mathematical Modeling of Neural systems. MIT Press.

De Ruyter van Steveninck, R., Bialek, W., 1988. Real-time performance of a movement-sensitive neuron in the blowfly visual system: Coding and information transfer in short spike sequences. In: Proceedings of the Royal Society of London. Vol. 234 of B. The Royal Society, pp. 379–414.

DeBusk, B. C., DeBruyn, E. J., Snider, R. K., Kabara, J. F., Bonds, A. B., Jul 1997. Stimulus-dependent modulation of spike burst length in cat striate cortical cells. J Neurophysiol 78 (1), 199–213.

Deweese, M., Zador, A., 1998. Asymmetric dynamics in optimal variance adaptation. Neural Computation 10, 1179–1202.

Diaz-Quesada, M., Maravall, M., 2008. Intrinsic Mechanisms for Adaptive Gain Rescaling in Barrel Cortex. J. Neurosci. 28 (3), 696–710.
URL http://www.jneurosci.org/cgi/content/abstract/28/3/696

Doiron, B., Oswald, A.-M. M., Maler, L., Apr 2007. Interval coding. ii. dendrite-dependent mechanisms. J Neurophysiol 97 (4), 2744–2757.
URL http://dx.doi.org/10.1152/jn.00988.2006

Eyherabide, H. G., Rokem, A., Herz, A. V. M., Samengo, I., 2008. Burst firing is a neural code in an insect auditory system. Front Comput Neurosci 2, 3.
URL http://dx.doi.org/10.3389/neuro.10.003.2008

Fairhall, A., Bialek, W., 2002. Adaptive spike coding, 2nd Edition. MIT Press, Cambridge, MA, pp. 90–94.

Fairhall, A. L., Lewen, G. D., Bialek, W., de Ruyter Van Steveninck, R. R., Aug 2001. Efficiency and ambiguity in an adaptive neural code. Nature 412 (6849), 787–792.
URL http://dx.doi.org/10.1038/35090500

French, A. S., Sep 1989. Two components of rapid sensory adaptation in a cockroach mechanoreceptor neuron. J Neurophysiol 62 (3), 768–777.

Gabbiani, Metzner, May 1999. Encoding and processing of sensory information in neuronal spike trains. J Exp Biol 202 ((Pt 10)), 1267–1279.

Gabbiani, F., C., K., 1998. Principles of spike train analysis. Cambridge, MA, pp. 313–360.

Gabbiani, F., Metzner, W., Wessel, R., Koch, C., Dec 1996. From stimulus encoding to feature extraction in weakly electric fish. Nature 384 (6609), 564–567.
URL http://dx.doi.org/10.1038/384564a0

Gilboa, G., Chen, R., Brenner, N., Jul 2005. History-dependent multiple-time-scale dynamics in a single-neuron model. J Neurosci 25 (28), 6479–6489.
URL http://dx.doi.org/10.1523/JNEUROSCI.0763-05.2005

Gray, C. M., McCormick, D. A., 1996. Chattering cells: Superficial pyramidal neurons contributing to the generation of synchronous oscillations in the visual cortex. Science 274 (5284), 109–113.
URL http://www.sciencemag.org/cgi/content/abstract/274/5284/109

Green, D., Swets, J., 1966. Signal detection theory and psychophysics. Wiley, New York.

Grzywacz, N. M., Balboa, R. M., Mar 2002. A bayesian framework for sensory adaptation. Neural Comput 14 (3), 543–559.
URL http://dx.doi.org/10.1162/089976602317250898

Gustafsson, B., Wigström, H., Sep 1983. Hyperpolarization following long-lasting tetanic activation of hippocampal pyramidal cells. Brain Res 275 (1), 159–163.

Izhikevich, E. M., Desai, N. S., Walcott, E. C., Hoppensteadt, F. C., Mar 2003. Bursts as a unit of neural information: selective communication via resonance. Trends Neurosci 26 (3), 161–167.

Jahnsen, H., Llinás, R., 1984. Ionic basis for the electroresponsiveness and oscillatory properties of guinea-pig thalamic neurons in vitro. J Physiol 349, 227–247.

Jansen, J., Nicholls, J., 1973. Conductance changes, an electrogenic pump and the hyperpolarization of leech neurones following impulses. J Physiol 229 (3), 635–655.
URL http://jp.physoc.org/cgi/content/abstract/229/3/635

Jarque, C. M., Bera, A. K., 1980. Efficient tests for normality, homoscedasticity and serial independence of regression residuals. Economics Letters 6 (3), 255 – 259.
URL http://www.sciencedirect.com/science/article/B6V84-458XPXV-1F/2/af1ee53d6726656427ecd1271512133c

Juusola, M., Robinson, H. P. C., de Polavieja, G. G., Feb 2007. Coding with spike shapes and graded potentials in cortical networks. Bioessays 29 (2), 178–187.
URL http://dx.doi.org/10.1002/bies.20532

Kandel, E. R., Spencer, W. A., 1961. Electrophysiolog of hippocampal neurons: Ii. afterpotentials and repetitive firing. J Neurophysiol 24 (3), 243–259.
URL http://jn.physiology.org

Kawai, F., Apr 2002. Ca2+-activated k+ currents regulate odor adaptation by modulating spike encoding of olfactory receptor cells. Biophys J 82 (4), 2005–2015.
URL http://dx.doi.org/10.1016/S0006-3495(02)75549-5

Keener, J., Sneyd, J., 1998. Mathematical Physiology. Springer.

Kenshalo, D. R., Isensee, O., Dec 1983. Responses of primate si cortical neurons to noxious stimuli. J Neurophysiol 50 (6), 1479–1496.

Kepecs, A., Lisman, J., 2003. Information encoding and computation with spikes and bursts. Networks: Comput. Neural Syst 14 (1), 103–118.

Kepecs, A., Wang, X.-J., Lisman, J., Oct 2002. Bursting neurons signal input slope. J Neurosci 22 (20), 9053–9062.

Kiernan, M. C., Lin, C. S.-Y., Burke, D., Jul 2004. Differences in activity-dependent hyperpolarization in human sensory and motor axons. J Physiol 558 (Pt 1), 341–349.
URL http://dx.doi.org/10.1113/jphysiol.2004.063966

Kim, K. J., Rieke, F., Feb 2003. Slow na+ inactivation and variance adaptation in salamander retinal ganglion cells. J Neurosci 23 (4), 1506–1516.

Kobayashi, J., Ohta, M., Terada, Y., Nov 1997. Evidence for the involvement of na+-k+ pump and k+ conductance in the post-tetanic hyperpolarization of the tetrodotoxin-resistant c-fibers in the isolated bullfrog sciatic nerve. Neurosci Lett 236 (3), 171–174.

Krahe, R., Gabbiani, F., Jan 2004. Burst firing in sensory systems. Nat Rev Neurosci 5 (1), 13–23.
URL http://dx.doi.org/10.1038/nrn1296

Kvale, M. N., Schreiner, C. E., Feb 2004. Short-term adaptation of auditory receptive fields to dynamic stimuli. J Neurophysiol 91 (2), 604–612.
URL http://dx.doi.org/10.1152/jn.00484.2003

Lacher, V., 1964. Elektrophysiologische untersuchungen an einzelnen rezeptoren für geruch, kohlendioxyd, luftfeuchtigkeit und tempratur auf den antennen der arbeits-biene und der drohne (apis mellifica l.). J COMP PHYSIOL A 48(6), 587– 623.

Laughlin, S., 1981. A simple coding procedure enhances a neuron's information capacity. Z Naturforsch [C] 36 (9-10), 910–912.
URL http://view.ncbi.nlm.nih.gov/pubmed/7303823

Laughlin, S. B., de Ruyter van Steveninck, R. R., Anderson, J. C., May 1998. The metabolic cost of neural information. Nat Neurosci 1 (1), 36–41.
URL http://dx.doi.org/10.1038/236

Lilliefors, H., 1967. On the kolmogorov-smirnov test for normality with mean and variance unknown. Journal of the American Statistical Association.

Linsker, R., 1988. Self-organization in a perceptual network. Computer 21 (3), 105–117.

Lisman, J. E., Jan 1997. Bursts as a unit of neural information: making unreliable synapses reliable. Trends Neurosci 20 (1), 38–43.

Livingstone, M. S., Freeman, D. C., Hubel, D. H., 1996. Visual responses in v1 of freely viewing monkeys. Cold Spring Harb Symp Quant Biol 61, 27–37.

Mainen, Z. F., Sejnowski, T. J., Jul 1996. Influence of dendritic structure on firing pattern in model neocortical neurons. Nature 382 (6589), 363–366.
URL http://dx.doi.org/10.1038/382363a0

Mar, A., Drapeau, P., 1996. Modulation of conduction block in leech mechanosensory neurons. J. Neurosci. 16 (14), 4335–4343.
URL http://www.jneurosci.org/cgi/content/abstract/16/14/4335

Maravall, M., Petersen, R. S., Fairhall, A. L., Arabzadeh, E., Diamond, M. E., Feb 2007. Shifts in coding properties and maintenance of information transmission during adaptation in barrel cortex. PLoS Biol 5 (2), e19.
URL http://dx.doi.org/10.1371/journal.pbio.0050019

Markram, H., Toledo-Rodriguez, M., Wang, Y., Gupta, A., Silberberg, G., Wu, C., October 2004. Interneurons of the neocortical inhibitory system. Nat Rev Neurosci 5 (10), 793–807.
URL http://dx.doi.org/10.1038/nrn1519

Markram, H., Wang, Y., Tsodyks, M., Apr 1998. Differential signaling via the same axon of neocortical pyramidal neurons. Proc Natl Acad Sci U S A 95 (9), 5323–5328.

Martinez-Conde, S., Macknik, S. L., Hubel, D. H., Oct 2002. The function of bursts of spikes during visual fixation in the awake primate lateral geniculate nucleus and primary visual cortex. Proc Natl Acad Sci U S A 99 (21), 13920–13925.
URL http://dx.doi.org/10.1073/pnas.212500599

Meister, M., Berry, M., 1999. The neural code of the retina. Neuron 22, 435–450.

Metzner, W., Koch, C., Wessel, R., Gabbiani, F., 1998. Feature extraction by burst-like spike patterns in multiple sensory maps. J. Neurosci. 18 (6), 2283–2300.
URL http://www.jneurosci.org/cgi/content/abstract/18/6/2283

Middlebrooks, J. C., Clock, A. E., Xu, L., Green, D. M., May 1994. A panoramic code for sound location by cortical neurons. Science 264 (5160), 842–844.

Mistick, D. C., Aug 1978. Neurones in the leech that facilitate an avoidance behaviour following nearfield water disturbances. J Exp Biol 75, 1–23.

Mozzachiodi, R., Scuri, R., Roberto, M., Brunelli, M., 2001. Caulerpenyne, a toxin from the seaweed *Caulerpa taxifolia* depresses afterhyperpolarization in invertebrate neurons. Neuroscience 107 (3), 519–526.

URL http://www.sciencedirect.com/science/article/B6T0F-44FBXJ9-H/1/db2791e0850151aa247ecadac1b5cd08

Muller, J., Nicholls, J., Stent, G., 1981. Neurobiology of the leech. Cold Spring harbor Laboratory.

Nicholls, J., Baylor, D., 1968. Specific modalities and receptive fields of sensory neurons in cns of the leech. J Neurophysiol 31 (5), 740–756.
URL http://jn.physiology.org

Nicholls, J., Van Essen, D., 1974. The nervous system of the leech. Sci. Am 230 (1), 38–48.

Oja, E., 2002. Principal Component Analysis. Cambridge: MIT Press, MA, pp. 90–94.

Oswald, A.-M. M., Doiron, B., Maler, L., Apr 2007. Interval coding. i. burst interspike intervals as indicators of stimulus intensity. J Neurophysiol 97 (4), 2731–2743.
URL http://dx.doi.org/10.1152/jn.00987.2006

Parpura, V., Basarsky, T. A., Liu, F., Jeftinija, K., Jeftinija, S., Haydon, P. G., 1994. Glutamate-mediated astrocyte-neuron signalling. Nature 369, 744–747.

Pinato, G., Torre, V., 2000. Coding and adaptation during mechanical stimulation in the leech nervous system. J Physiol 529 (3), 747–762.
URL http://jp.physoc.org/cgi/content/abstract/529/3/747

Polavieja, G. G. D., Harsch, A., Kleppe, I., Robinson, H. P. C., Juusola, M., Jun 2005. Stimulus history reliably shapes action potential waveforms of cortical neurons. J Neurosci 25 (23), 5657–5665.
URL http://dx.doi.org/10.1523/JNEUROSCI.0242-05.2005

Prescott, S. A., Sejnowski, T. J., 2008. Spike-Rate Coding and Spike-Time Coding Are Affected Oppositely by Different Adaptation Mechanisms. J. Neurosci. 28 (50), 13649–13661.
URL http://www.jneurosci.org/cgi/content/abstract/28/50/13649

Rieke, F., Dec 2001. Temporal contrast adaptation in salamander bipolar cells. J Neurosci 21 (23), 9445–9454.

Rieke, F., Warland, D., de Ruyter, Bialek, W., 1997. Spikes: Exploring the neural code.
URL http://books.google.com/books?id=Sl5KAQAACAAJ\&dq=Spikes:+Exploring+the+Neural+Code\&ei=1E6MSeKqDI3CNqyM1bAF

Sanchez-Vives, M. V., Nowak, L. G., McCormick, D. A., Jun 2000a. Cellular mechanisms of long-lasting adaptation in visual cortical neurons in vitro. J Neurosci 20 (11), 4286–4299.

Sanchez-Vives, M. V., Nowak, L. G., McCormick, D. A., Jun 2000b. Membrane mechanisms underlying contrast adaptation in cat area 17 in vivo. J Neurosci 20 (11), 4267–4285.

Schingnitz, G., Werner, J., 1980. Thalamic burst firing – a neuronal code for temperature information? Brain Research 195 (2), 467 – 470.
URL http://www.sciencedirect.com/science/article/B6SYR-48360MN-N3/2/70be51b64fee698e1495b0f49b29ce61

Schlue, W., 1991. Effects of ouabain on intracellular ion activities of sensory neurons of the leech central nervous system. J Neurophysiol 65 (3), 736–746.
URL http://jn.physiology.org/cgi/content/abstract/65/3/736

Scuri, R., Mozzachiodi, R., Brunelli, M., 2002. Activity-Dependent Increase of the AHP Amplitude in T Sensory Neurons of the Leech. J Neurophysiol 88 (5), 2490–2500.
URL http://jn.physiology.org/cgi/content/abstract/88/5/2490

Scuri, R., Mozzachiodi, R., Brunelli, M., 2005. Role for calcium signaling and arachidonic acid metabolites in the activity-dependent increase of ahp amplitude in leech t sensory neurons. J Neurophysiol 94 (2), 1066–1073.
URL http://jn.physiology.org/cgi/content/abstract/94/2/1066

Sejnowski, T. J., 1999. Neural codes and distributed representations: foundations of neural computation. MIT Press, Cambridge, MA, USA.

Shannon, C. E., 1948. A mathematical theory of communication. Bell system technical journal 27.

Shapley, L., 1989. Retinal physiology: Adapting to the changing scene. Curr. Biol. 7, R421–R423.

Sharpee, T. O., Sugihara, H., Kurgansky, A. V., Rebrik, S. P., Stryker, M. P., Miller, K. D., Feb 2006. Adaptive filtering enhances information transmission in visual cortex. Nature 439 (7079), 936–942.
URL http://dx.doi.org/10.1038/nature04519

Shen, K. Z., Johnson, S. W., Oct 1998. Sodium pump evokes high density pump currents in rat midbrain dopamine neurons. J Physiol 512 (Pt 2), 449–457.

Sherman, S. M., Feb 2001. Tonic and burst firing: dual modes of thalamocortical relay. Trends Neurosci 24 (2), 122–126.

Shu, Y., Hasenstaub, A., Duque, A., Yu, Y., McCormick, D. A., 2006. Modulation of intracortical synaptic potentials by presynaptic somatic membrane potential. Nature 441, 761– 765.

Smirnakis, S., Warland, D., Bialek, W., Meister, M., 1997. Adaptation of retinal processing to image contrast and spatial scale. Nature 386, 69–73.

Sobel, E. C., Tank, D. W., 1994. In Vivo Ca2+ Dynamics in a Cricket Auditory Neuron: An Example of Chemical Computation. Science 263 (5148), 823–826.
URL `http://www.sciencemag.org/cgi/content/abstract/263/5148/823`

Stein, R. B., Gossen, E. R., Jones, K. E., May 2005. Neuronal variability: noise or part of the signal? Nat Rev Neurosci 6 (5), 389–397.
URL `http://dx.doi.org/10.1038/nrn1668`

Stemmler, M., Koch, C., Jun 1999. How voltage-dependent conductances can adapt to maximize the information encoded by neuronal firing rate. Nat Neurosci 2 (6), 521–527.
URL `http://dx.doi.org/10.1038/9173`

Su, H., Alroy, G., Kirson, E. D., Yaari, Y., 2001. Extracellular Calcium Modulates Persistent Sodium Current-Dependent Burst-Firing in Hippocampal Pyramidal Neurons. J. Neurosci. 21 (12), 4173–4182.
URL `http://www.jneurosci.org/cgi/content/abstract/21/12/4173`

Theunissen, F., Miller, J. P., Jun 1995. Temporal encoding in nervous systems: a rigorous definition. J Comput Neurosci 2 (2), 149–162.

Tsodyks, M. V., Markram, H., Jan 1997. The neural code between neocortical pyramidal neurons depends on neurotransmitter release probability. Proc Natl Acad Sci U S A 94 (2), 719–723.

Vaillend, C., Mason, S. E., Cuttle, M. F., Alger, B. E., Dec 2002. Mechanisms of neuronal hyperexcitability caused by partial inhibition of na+-k+-atpases in the rat ca1 hippocampal region. J Neurophysiol 88 (6), 2963–2978.
URL `http://dx.doi.org/10.1152/jn.00244.2002`

Van der Heyden, M., Hilgevoord, A., Bour, L., Ongerboer de Visser, B., 1994. Modeling motoneuron firing properties: dependency on size and calcium dynamics. Biol. Cybern. 72 (2), 133–139.
URL http://www.springerlink.com/content/u326474p06580811

Van Essen, D., 1973. The contribution of membrane hyperpolarization to adaptation and conduction block in sensory neurones of the leech. J Physiol 230 (3), 509–534.
URL http://jp.physoc.org/cgi/content/abstract/230/3/509

Volterra, A., Steinhäuser, C., August 2004. Glial modulation of synaptic transmission in the hippocampus. Glia 47 (3), 249–257.
URL http://dx.doi.org/10.1002/glia.20080

Walraven, J., Enroth-Cugell, C., Hood, D., MacLeod, D., Schnapf, J., 1990. The control of visual sensitivity. in Visual Perception: The Neurophysiological Foundations. Academic Press, New York.

Wang, X.-J., 1998. Calcium Coding and Adaptive Temporal Computation in Cortical Pyramidal Neurons. J Neurophysiol 79 (3), 1549–1566.
URL http://jn.physiology.org/cgi/content/abstract/79/3/1549

Wark, B., Lundstrom, B. N., Fairhall, A., August 2007. Sensory adaptation. Current Opinion in Neurobiology 17 (4), 423–429.
URL http://dx.doi.org/10.1016/j.conb.2007.07.001

Wimmer, K., Hildebrandt, K. J., Hennig, R. M., Obermayer, K., 2008. Adaptation and selective information transmission in the cricket auditory neuron an2. PLoS Comput Biol 4 (9), e1000182.
URL http://dx.doi.org/10.1371/journal.pcbi.1000182

Womack, M., Khodakhah, K., 2002. Active Contribution of Dendrites to the Tonic and Trimodal Patterns of Activity in Cerebellar Purkinje Neurons. J. Neurosci. 22 (24), 10603–10612.
URL http://www.jneurosci.org/cgi/content/abstract/22/24/10603

Wright, B. D., Sen, K., Bialek, W., Doupe, A. J., 2002. Spike timing and the coding of naturalistic sounds in a central auditory area of songbirds.
URL http://www.citebase.org/abstract?id=oai:arXiv.org:physics/0201027

Yamada, W., Koch, C., Adams, P., 1989. Multiple channels and calcium dynamics, 97–133.

Yau, K. W., Dec 1976. Receptive fields, geometry and conduction block of sensory neurones in the central nervous system of the leech. J Physiol 263 (3), 513–538.